# MSc Thesis report

## Incremental Nonlinear Dynamic Inversion controller - structural vibration coupling
## Study of the phenomenon and the existing solutions

**Master Thesis**

Alessandro Collicelli

# MSc Thesis report

## Incremental Nonlinear Dynamic Inversion controller - structural vibration coupling Study of the phenomenon and the existing solutions

by

Alessandro Collicelli

| | | |
|---|---|---|
| Student number: | 5133769 | |
| Project duration: | March, 2021 – September, 2022 | |
| Thesis committee: | Prof. Dr. G. C. H. E. de Croon, | TU Delft, chair |
| | Dr. Ir. E. J. J. Smeur, | TU Delft, supervisor |
| | Ir. T. S. C. Pollack, | TU Delft, supervisor |
| | Dr. X. Wang, | TU Delft, external examiner |
| Institution: | Delft University of Technology | |
| Profile: | Control and Operation | |
| Track: | Control and Simulation | |
| Collaborations: | MavLab | |
| Place: | Faculty of Aerospace Engineering, Delft | |

Cover Image: Boeing 787 wing flexion test, Source: Wired.com

TU Delft

# Preface

To the ones who supported me during this Master of Science endeavour: my family, my close and distant friends, my mentors and to all the people who shared a moment with me, thank you from the bottom of my heart.

*Alessandro Collicelli*
*Delft, September 29, 2022*

# Contents

# 1 Introduction

## 1.1. Background information on the thesis project

The Master Thesis project described in this document is meant to be the final task of the Aerospace Engineering Master of Science degree at Delft Technological University, for the track of *Control & Operation*, profile *Control & Simulation*. This project aims to provide insights on a relevant aerospace engineering topic or problem via scientific investigation. The tasks to be fulfilled during this Master Thesis project were to study the interaction between the structural vibrations of a flying vehicle and the flight control system, to understand the causes of it, and to identify, implement, and tested different solutions to the coupling of both simulation and flight tests.

In recent years, aerospace structures have become increasingly thin and slender, due to the introduction of new structural materials and the need to decrease the amount of weight dedicated to the structural elements (Malisani *et. al*, 2021, [1]). Aircraft structures have become more flexible and less rigid, thus structural motions and rigid body motions frequency separation is drastically reduced. Therefore the structural vibration contribution in the sensor measurements is now comparable to the rigid body motion one. Consequently, the structural element contribution to the signal fed to the flight control system is more dominant than for more rigid aircraft (Becker *et al*., 2014, [2]). This generates an undesired interaction between the flight control system and the structural motions that can lead to instability of both rigid body dynamics and structural dynamics.

Incremental Nonlinear Dynamic Inversion-based flight control systems are controllers that aim to linearize the system dynamics to allow them to be controlled using classical control theory, are known for their robustness to model uncertainties and their disturbance rejection capabilities. INDI-based controllers have been implemented and tested on a variety of platforms, among which there is the Nederdrone a tail-sitter drone with vertical take-off and landing capabilities. Due to its slender shape, it has low-frequency structural modes which interact with the INDI controller on the yaw axis. Therefore, despite its high robustness and disturbance rejection performances, this flight controller was found to interact with the structural modes of the vehicle for which it was designed and to lead to unstable or limit-cycle oscillation behaviors. Hence, the Nederdrone was chosen as a test platform to investigate the coupling between its structural characteristics and the flight control system designed for its hover flight phase.

## 1.2. Research objective and research questions

The research objective is to study different INDI implementations designed to reduce the coupled interaction between the controller and the structural modes and to assess their behaviour when implemented in an aircraft with low frequency, low damping structural eigenmodes. To achieve this objective and to better define the direction of the research, the following research questions and related sub-questions were defined:

> *RQ.1* INDI-based flight control systems have high disturbance rejection performances. What is INDI controller behaviour when it is designed for rigid body motion stabilization but is applied to a highly flexible aircraft?

*1.1* How are INDI-based controllers usually improved to avoid coupling with structural modes?

*RQ.2* The Nederdrone is a two fixed-wing tailsitter MAV eVTOL (De Wagter *et al*.2021, [3]), mounting a FCS which has two nested INDI control loops. How can INDI based flight control system be applied to this vehicle while avoiding structural vibrations excitation due to control input?

*2.1* What structural eigenmotions are coupled with the FCS and for what reason it makes the whole system unstable?
*2.2* How can the use of signal filtering for low-frequency dynamics be avoided (or reduced)?
*2.3* What are the performances of an "interactionless" INDI flight control system compared to the ones of a benchmark INDI FCS in terms of the presence of structural vibration and flight quality (nonlinear dynamic inversion qualities, closed-loop response, and disturbance rejection)?

## 1.3. Document layout

This Master Thesis document contains the descriptions of all the various steps taken to execute and conclude the aforementioned research project.

The literature survey conducted in preparation for the main research activity and the following preliminary analysis study are reported after this introduction. Their goal was to obtain the necessary theoretical background on structural dynamics, servo-elastic phenomena, and Incremental Nonlinear Dynamic Inversion controller design before starting the main research activity. The preliminary analysis of the thesis topic was operated on a smaller and more accessible test platform affected by the same coupled behaviour of the Nederdrone. It was conducted to develop a general understanding of the flight control system (INDI) - structural vibration interaction and to gather experience on the testing platform framework and testing procedures. Both the literature survey and the preliminary analysis together contribute to answering the first research question.

The main research activity is reported and described in the scientific paper, which follows the literary survey and the preliminary analysis. It contains the main part of the research activity, which is constituted by the ground vibration test, system identification process with relative validation from flight test data, implementation of different investigated solutions both in simulation and on the real system, and performance assessment both in simulation and flight test. In the first paper appendix, a brief derivation of the INDI is reported, while the second appendix contains a report on the ground vibration test set-up and results. There, pictures regarding the test setup are reported, and graphs and schemes describing the structural modes of the Nederdrone are shown. This part of the report aims to answer the second research question. After the scientific paper, a conclusion chapter closes up this document.

# 2

# Literature survey and preliminary analysis

# Literature Survey & Preliminary Analysis report

## Flight control system - structural eigenmodes interaction
## Consequences and implemented solutions

by


Alessandro Collicelli

| Student Name | Student Number |
|---|---|
| Alessandro Collicelli | 5133769 |


| | |
|---|---|
| Supervisor: | dr. Ir. Ewoud Smeur & Ir. Tijmen Pollack |
| Institution: | Delft University of Technology |
| Department: | Control and Simulation & MavLab |
| Place: | Faculty of Aerospace Engineering, Delft |
| Project Duration: | March, 2021 - September, 2022 |
| Hand in date: | October, 2021 |



TU Delft

# Contents

# Nomenclature

## Abbreviations

| Abbreviation | Definition |
|---|---|
| AFS | Active Flutter Suppression |
| ASE | Aeroservoelastic |
| C&S | Control & Simulation |
| EVTOL | Electrical Vertical Take Off Landing |
| FCS | Flight Control System |
| FT | Fourier Transform |
| GVT | Ground Vibration Test |
| HALE | High Altitude Long Endurance |
| INDI | Incremental Nonlinear Dynamic Inversion |
| LCO | Limit Cycle Oscillations |
| LQR | Linear Quadratic Regulator |
| MAV | Micro Air Vehicle |
| MIMO | Multiple Input Multiple Output |
| NDI | Nonlinear Dynamic Inversion |
| ODE | Ordinary Differential Equation |
| PDE | Partial Differential Equation |
| PID | Proportional Integral Derivative |
| PINDI | Predictive Incremental Nonlinear Dynamic Inversion |
| PSD | Power Spectral Density |
| RFA | Rational Function Approximation |
| SISO | Single Input Single Output |

# List of Figures

1

# Introduction

This document is the result of a literature survey conducted to acquire knowledge and insight on structural vibration phenomena and nonlinear dynamic inversion control system, prior to the beginning of the master thesis project for the attainment of the master's degree on Control & Simulation profile at Delft University of Technology. The thesis topic aims at the analysis of the interaction between structural elastic eigenmotions and nonlinear dynamic inversion based flight control system.

In recent years, aerospace structures have become increasingly thin and slender, due to the introduction of new structural materials and the need to decrease the amount of weight dedicated to the structural elements (Malisani *et. al*, 2021, [14]). Therefore, aircraft structures have become more flexible and less rigid, increasing the maximum displacement allowed from their undeformed position. Moreover, the natural frequencies of the structural vibrations have decreased due to the decrease in structural stiffness. Thus, structural motions and rigid body motions frequency separation is drastically reduced, and therefore the structural vibration contribution in the sensor measurements is now comparable to the rigid body motion one. Therefore, the structural element contribution to the signal fed to the flight control system (FCS) is more dominant than for more rigid aircraft (Becker *et al*., 2014, [3]). This generates an undesired interaction between the flight control system and the structural motions that can lead to instability of both rigid body dynamics and structural dynamics. If the aerospace industry wants to keep this trend going, it is of key importance to investigate the aforementioned interaction between FCS and structural vibrations.

The thesis project testing platform will be provided by MavLab laboratory as in unmanned air vehicles experiencing structural vibration - flight control system destructive interaction. The vehicles will be the Parrot Bebop 2, a commercial quadrotor, and the Nederdrone, a two fixed wings tail-sitter vehicle developed by MavLab researchers.

Throughout the years, Control & Simulation (C&S) department researchers have studied, developed, and tested a multitude of nonlinear inversion-based controllers such as in Groondman *et al*.[11] where INDI base control system has been designed and tested in flight for a passenger aircraft and in Sieberling *et al*.[21], where the standard INDI control loop is improved via the implementation of a predictive signal to compensate for sampling lag. Moreover, in Wang *et al*.[30] an INDI based flight control and gust load alleviation system is designed and tested in simulation for a passenger aircraft. Nonlinear inversion control strategies have been tested over the years on unmanned air vehicles configurations for example in Smeur *et al*.2016 [23] and 2018 [24] where an angular rate and an attitude controller for a Parrot Bebop 2 are designed, showing easiness on implementation and effectiveness in achieving the assigned control task and robustness in the performances. Another example is the FCS of the Nederdrone as shown by de Wagter *et al*.in [6], where an INDI is implemented in cascade to ensure position and attitude angle tracking. Lately, particular attention has been given to Incremental Nonlinear Dynamic Inversion (INDI) based controller, due to its proven robustness and disturbance rejection characteristics.

Thus, the literature study and the following master thesis project intend to contribute to the research on the interaction between incremental nonlinear dynamic inversion flight control systems and structural vibration motions. The two main contributions will be to provide a better understanding of the phenomena involved and to investigate possible solutions to this problem.

This document aims to provide a description of the phenomena involved in the structural eigenmotion - flight control system interaction and to find preliminary answers to some research question in the available literature.

Thus, the relevant literature regarding different aspects of the aforementioned phenomena is reported and analysed. The concerning literature space contains fields that are very different from one another, going from dynamic of continuous bodies to aerodynamic, to flight control system design. Therefore, due to the broadness of each field, only the subjects of each topic overlapping with other fields relevant to the analyzed problem will be discussed. For a deeper and more extensive dissertation on every single topic, the relevant literature is mentioned. Moreover, the case for nonlinear dynamic inversion controller being a suitable control strategy to effectively cope with the aforementioned destructive interaction will be made.

The document is structured as follows: in chapter 2, the theoretical background for continuous vibration modelling is laid out, together with the description of possible coupling effects between flight control systems and flexible dynamics. Aeroelastic phenomena are included in the coupling effect discussion. In chapter 3, currently implemented solutions for flight control system - flexible motion interaction attenuation and aeroelastic phenomena suppression are described. Then, in chapter 4 the description of two nonlinear dynamic inversion control strategies is provided, together with a discussion on the strengths and the drawbacks of the aforementioned control techniques. Later, in chapter 5, a preliminary analysis of the research questions will be carried out both in simulation and with flight test, to investigate the FCS - structural eigenmotion interaction in the simplified case of the Bebop 2 roll dynamic. The conclusion in chapter 6 will end the literature study report with a discussion of the literature survey findings.

# Structural flexibility in aerospace structures

In this first chapter, the theoretical background behind the description of structural eigenmodes and how their presence influences the aircraft motion, and the flight control system performance will be laid out. Initially, in section 2.1, a general discussion about how to represent the vibration of continuous bodies will be carried out 2.1.1, together with solution of the relative equations and description of solution reduction methods for structural modelling 2.1.2. Later in section 2.2, the derived structural modes will be integrated into the equations of motion of an aircraft and coupled with aerodynamic state space system to obtain aeroservoelastic aircraft models. Therefore, it will be possible to analyse the aforementioned aircraft plant and to highlight the critical phenomena related to the presence of flexible body dynamics, such as flutter and limit cycle oscillation. Finally, phenomena related to the interaction between structural eigenmodes, unsteady aerodynamic and flight control systems will be discussed.

## 2.1. Equation of motion for vibration of continuous bodies: derivation and solution

In order to better explain the derivation of the general description of structural eigenmodes, an auxiliary example will be used to make the dissertation clearer to the reader. To keep the example simple and short the longitudinal vibration of a bar will be considered. The equation describing the bending or torsion of a continuous body can be derived in multiple ways and can assume different forms. In our example, the variational approach is chosen, and the Hamilton principle is applied to write the equation of motion. Hamilton principle states that the variation in the total energy of a system is equal to the virtual work done on the system by non-conservative external forces. Once both the variation of the total energy and the work of the non-conservative external forces are explicitly defined as well as the boundary conditions, the equation describing the longitudinal vibration of a bar will be obtained. For a complete and exhaustive dissertation about the cinematic and the stress-strain relation in the longitudinal bar please refer to Rao 2007 [20].

### 2.1.1. Equation of motion derivation

Given the relations in equation 2.1, where $u(x,t)$ is the longitudinal displacement, $x$ is the longitudinal coordinate and $\sigma_{xx}(u)$ is the longitudinal stress. $\varepsilon_{xx}(u)$ is the longitudinal strain, $\pi$ is the internal or strain energy, $T$ is the kinetic energy and $W$ is the virtual work of non-conservative forces. Assuming the bar is with constant section $A(x) = A$ and homogeneous $\rho(x) = \rho$.

$$\begin{aligned} \sigma_{xx} &= E\frac{\partial u}{\partial x} = E\varepsilon_{xx} \\ \pi &= \frac{1}{2}\int_0^l \sigma_{xx}\varepsilon_{xx}A\,dx = \frac{1}{2}\int_0^l EA\left(\frac{\partial u}{\partial x}\right)^2 dx \\ T &= \frac{1}{2}\int_0^l \rho A\left(\frac{\partial u}{\partial t}\right)^2 dx \\ W &= \int_0^l f(x,t)u\,dx \end{aligned} \quad . \tag{2.1}$$

The Hamilton principle is outlined in equation 2.2.

$$\delta\int_{t_1}^{t_2}(T-\pi+W)dt = 0 \tag{2.2}$$

Substituting equations from 2.1 into 2.2 and operating the due simplifications, the following partial derivative equations are obtained:

$$\begin{aligned} EA\frac{\partial^2 u}{\partial x^2} + f(x,t) &= \rho A \frac{\partial^2 u}{\partial t^2} \\ EA\frac{\partial u}{\partial x}\delta u\Big|_0^l &= 0 \end{aligned} \tag{2.3}$$

where $f(x,t)$ is the external distributed force that is known. In addition to these equations, the boundary condition must be defined depending on the structural setup. For a bar cantilever at one end, $x = 0$, and free to vibrate on the other end, $x = l$, then the boundary conditions are:

$$\begin{aligned} &u(0,t) = 0 \\ &\sigma_{xx} = AE\frac{\partial u(x,t)}{\partial x}\Big|_{x=l} = 0 \end{aligned} \tag{2.4}$$

and the initial condition are:

$$\begin{aligned} &u(x,t=0) = u_0(x) \\ &\frac{\partial u}{\partial t}(x,t=0) = \dot{u}_0(x) \end{aligned} \tag{2.5}$$

### 2.1.2. Induction to general eigenvalue problem

To solve equation 2.3, which has the form of an eigenvalue problem, a modal analysis approach will be adopted. This solution method can solve a class of partial differential equations of the form:

$$M(\vec{X})\frac{\partial^2 w(\vec{X},t)}{\partial t^2}) + L[w(\vec{X},t)] = f(\vec{X},t) + \sum_{j=1}^{s} F_j(t)\delta(\vec{X} - \vec{X}_j) \tag{2.6}$$

where $\vec{X}$ is spatial coordinate, which varies inside its domain $V$, that in this case is the volume occupied by the flexible body. $M(\vec{X})$ is the mass distribution and $w(\vec{X},t)$ is the displacement on the system which depend on both the spatial variables and the time. $L[w(\vec{X},t)]$ is the so-called stiffness distribution of the system and $f(\vec{X},t)$ is the set of distributed forces acting on a system as function of the spatial variable and time. $F_j(t)$ is the j-th concentrated force acting on the point $\vec{X} = \vec{X}_j$. Generally speaking, $L$ and $M$ are linear homogeneous differential operators involving derivative with respect to spatial variables but not with respect to time, up to the orders $2p$ and $2q$ respectively where $p$ and $q$ are integers with $p > q$. Moreover, the boundary conditions have the form:

$$A_i[w] = \lambda B_i[w], \qquad i = 1,2,..,p \tag{2.7}$$

where $A_i$ and $B_i$ are linear homogeneous differential operators involving derivatives of $w$, with respect to the normal and tangential direction of the boundary, up to the order $2p-1$, and $\lambda$ is a parameter known as the eigenvalue of the system. In some problems the boundary conditions do not involve eigenvalues in which case the equation reduces to:

$$A_i[w] = 0, \qquad i = 1,2,..,p \tag{2.8}$$

Referring to our example, it's easy to see that:

$$\begin{aligned} &M(\vec{X}) = -\rho A \\ &L[w(\vec{X},t)] = EA\frac{\partial^2 u}{\partial x^2} \\ &\begin{bmatrix} A_1(w) \\ A_2(w) \end{bmatrix} = \begin{bmatrix} u(0,t) \\ AE\frac{\partial u(x,t)}{\partial x}\Big|_{x=l} \end{bmatrix} = \begin{bmatrix} 0 \\ 0 \end{bmatrix} \\ &w(\vec{X},t) = u(x,t) \end{aligned} \tag{2.9}$$

where $x = l$ subscript on the partial derivative of the last equation in 2.9 describe the condition in the boundary $x$ domain $V$. Obviously, depending on the vibration problem considered, $L$ and $M$ operators are different. For sake of clarity, below in equations 2.10 and 2.11, examples of $L$ and $M$ for different cases are given:

$$\begin{aligned} M &= \rho(x) \\ L &= P\frac{\partial^2}{\partial x^2} \end{aligned} \tag{2.10}$$

$$\begin{aligned} M &= I_0(x) \\ L &= \frac{\partial}{\partial x}\left(GI_P\frac{\partial}{\partial x}\right) \end{aligned} \tag{2.11}$$

where 2.10 refers to the case of a string of mass distribution $\rho(x)$ subjected to a constant tension $P$ and 2.11 refers to the case of torsional vibration of a shaft with $G$, $I_0(x)$ and $I_P$ being respectively the shear modulus, the mass polar moment of inertia of the shaft per unit length and the polar moment of inertia of the cross-section of the shaft. To solve the general equation 2.6 it is required a two-step procedure, which first involves the solution of the homogeneous equation, namely setting $f(\vec{X},t)+\sum_{j=1}^{s}F_j(t)\delta(\vec{X}-\vec{X}_j)=0$, to obtain the eigenvalues and the corresponding eigenfunctions. Subsequently, the general equation can be solved. In both steps, the variable separation method is utilized. Thus the solution of the eigenvalue problem has the form $w(\vec{X},t)=W(\vec{X})\eta(t)$,

### 2.1.3. Homogeneous equation solution

In the first step of the solution procedure, also know as variable separation technique [20], equation 2.6 becomes

$$M(\vec{X})\frac{\partial^2}{\partial t^2}[w(\vec{X},t)]+L[w(\vec{X},t)]=0 \tag{2.12}$$

and the structure of the solution function is chosen to be as in equation 2.13, with an arbitrary time domain contribution.

$$w(\vec{X},t)=W(\vec{X})e^{i\omega t} \tag{2.13}$$

where $W(\vec{X})$ is the eigenfunction or shape mode. Substituting 2.13 into 2.12 we obtain

$$\begin{aligned} M(\vec{X})\frac{\partial^2}{\partial t^2}[W(\vec{X})e^{i\omega t}]+L[W(\vec{X})e^{i\omega t}]&=0 \\ -\omega^2 M(\vec{X})W(\vec{X})e^{i\omega t}+L[W(\vec{X})]e^{i\omega t}&=0 \\ L[W(\vec{X})]&=\lambda M[W(\vec{X})] \end{aligned} \tag{2.14}$$

with $\lambda=\omega^2$ and $M[W(\vec{X})]=M(\vec{X})W(\vec{X})$. From the second to the third equation in 2.14, all the terms on the left are divided by $e^{i\omega t}$. The last equation from 2.14 turns out to be a set of ordinary differential equations on the spatial variable, which can be solved knowing the boundary conditions of the homogeneous problem. Therefore, the solution of the eigenvalue problem yields to an infinite number of eigenvalues $\lambda_1,\lambda_2,...$ and their respective eigenfunction or shape modes $W_1(\vec{X}),W_2(\vec{X}),....$ The eigenfunction are orthogonal to one another in the sense of given two distinct shape modes $W_m(\vec{X})$ and $W_n(\vec{X})$, then it can be proved that:

$$\int_V M(\vec{X})W_m(\vec{X})W_n(\vec{X})dV=\delta_{mn} \tag{2.15}$$

where $\delta_{mn}$ is the Kronecker delta function described in 2.16.

$$\begin{aligned} \delta_{mn}&=0 \;\; m\neq n \\ \delta_{mn}&=1 \;\; m=n \end{aligned} \tag{2.16}$$

Since the just obtained solution comes from a homogeneous problem and the time component has been dropped, only the shape of the eigenfunctions can be determined uniquely, while the amplitude is arbitrary. It is worth mentioning that this last property allows the eigenfunction to be normalized in the following way. With shape of the eigenfunction is meant the value of the component of $\omega(\vec{X},t)$ which affect the the spatial structural displacement, namely $W(\vec{X})$. Meanwhile, the term that in equation 2.14 is constituted by $e^{i\omega t}$, can be generalized to a $\eta(t)$ function of time, which describe the amplitude of the structural displacement throughout a series of instants.

$$\int_V W_m(\vec{X})L[W_n(\vec{X})]dV = \omega_m^2\delta_{mn} = \lambda_m\delta_{mn} \tag{2.17}$$

Finally, it is worth mentioning that the solution of the eigenvalue problems having the structure as equation 2.6 benefits from the expansion theorem, which allows the solution function to be expressed as it follows

$$w(\vec{X},t) = \sum_{m=1}^{\infty} W_m(\vec{X})\eta_m(t) \tag{2.18}$$

The orthogonality property, the normalization property and the expansion theorem are properties of the homogeneous problem solution which will later be used to solve the non-homogeneous problem.

### 2.1.4. Non-homogeneous equation solution

Considering equation 2.6, which describes the equation of motion of a continuous system, or body, under the excitation of external forces, with the boundary conditions expressed by equation 2.8 and initial condition depicted as in equation 2.19

$$\begin{aligned} w(\vec{X},0) &= h(\vec{X}) \\ \frac{\partial w(\vec{X},0)}{\partial t} &= g(\vec{X}) \end{aligned} \tag{2.19}$$

Given that, according to the expansion theorem[1], the forced response of the system which solves the just mentioned problem can be expressed as in equation 2.18,where $\eta_m(t)$ is the time dependent generalized coordinate. Then, if the aforementioned equation is inserted in 2.6 the results are

$$M(\vec{X})\frac{\partial^2}{\partial t^2}\left[\sum_{m=1}^{\infty} W_m(\vec{X})\eta_m(t)\right] + L\left[\sum_{m=1}^{\infty} W_m(\vec{X})\eta_m(t)\right] = f(\vec{X},t) + \sum_{j=1}^{s} F_j(t)\delta(\vec{X}-\vec{X}_j) \tag{2.20}$$

which can be rearranged as it follows, with $\ddot{\eta}_m(t) = d^2\eta_m(t)/dt^2$

$$\sum_{m=1}^{\infty} \ddot{\eta}_m(t)M(\vec{X})W_m(\vec{X}) + \sum_{m=1}^{\infty} \eta_m(t)L[W_m(\vec{X})] = f(\vec{X},t) + \sum_{j=1}^{s} F_j(t)\delta(\vec{X}-\vec{X}_j) \tag{2.21}$$

Now, to continue with the solving procedure and to utilize the orthogonality property, equation 2.21 is multiplied by $W_n(\vec{X})$ and integrated over the whole domain $V$ of the rigid body

$$\begin{aligned} \sum_{m=1}^{\infty} \ddot{\eta}_m(t)\int_V W_n(\vec{X})M(\vec{X})W_m(\vec{X})dV + \sum_{m=1}^{\infty} \eta_m(t)\int_V W_n(\vec{X})L[W_m(\vec{X})]dV = \\ \int_V W_n(\vec{X})f(\vec{X},t)dV + \sum_{j=1}^{s}\int_V W_n(\vec{X})F_j(t)\delta(\vec{X}-\vec{X}_j)dV \end{aligned} \tag{2.22}$$

By using the orthogonality property[1] showed in equation 2.15, the first term of 2.22 under the integral is equal to one only when $m = n$. Moreover, according to the normalization[1] of the shape mode operated earlier in 2.17, the second term of 2.22 under the integral is equal to $\omega^2$, again only when $m = n$. Finally using the property of the Dirac delta, the last term of equation 2.22 is simplified as shown in the below equation, where 2.22 becomes

$$\ddot{\eta}_m(t) + \omega_m^2\eta_m(t) = \int_V W_m(\vec{X})f(\vec{X},t)dV + \sum_{j=1}^{s} W_m(\vec{X}_j)F_j(t) = Q_m(t) \qquad m = 1,2,... \tag{2.23}$$

which is an infinite set of second-order ordinary differential equation with respect to the time variable, where $Q_m(t)$ is called the $m^{th}$ generalized force. The solution of equation 2.23 can be expressed as

$$\eta_m(t) = \frac{1}{\omega_m}\int_0^t Q_m(\tau) sin(\omega_m(t-\tau))d\tau + \eta_m(0)cos(\omega_m t) + \dot{\eta}_m(0)\frac{sin(\omega_m t)}{\omega_m t} \tag{2.24}$$

where $\dot{\eta}_m(0)$ and $\eta_m(0)$ can be calculated from the initial condition specified in equation 2.19. It is clear by looking at 2.24 that the solution function of the eigenvalue problem describing the equation of motion of a continuous body $w(\vec{X},t)$ has space dependant part in the eigenfunction or shape mode $W_m(\vec{X})$, and a time-dependant part in the generalized coordinate $\eta_m(t)$. Given that the solution of the eigenvalue problem has the structure specified in 2.24, this means that the time response has an infinite number of contribution in the frequency domain, each of those contribution associated with an eigenvalue $\lambda_m = \omega_m^2$.

It is worth mentioning that in the above discussion of continuous body vibration, a damping term, which could have been considered in the problem description, has been omitted for sake of simplicity. As in real applications continuous bodies do not oscillate for an infinite time, a viscous damping contribution can be added on the right-hand side of the equation 2.6 as

$$-\frac{\partial}{\partial t}C[w(\vec{X},t)] \tag{2.25}$$

where $C[w(\vec{X},t)]$ must have the same properties of $L[w(\vec{X},t)]$. When solving the augmented eigenvalue problem, an extra term will be present in equation 2.23, accounting for a damping contribution in the time response equation depending on $\dot{\eta}_m(t)$. In a practical situation, the value or structure of the damping term is not known and it is usually approximated as a linear combination of the operators $L$ and $M$ as $C = \alpha_1 L + \alpha_2 M$.

### 2.1.5. Model reduction

In order to utilize the equation obtained above to model the structural eigenmodes of an aircraft to later base on those the design of a control system, it is necessary to reduce the contributions considered for the solution of the eigenvalue problem to a finite number. Different approaches can be adopted and below three of the most common reduction techniques will be described. As first approach, it is possible to just consider only the first $a < \infty$ terms of the solution. In this case, the considered solution is not to be regarded as exact but as an approximation

$$w(\vec{X},t) \approx \hat{w}(\vec{X},t) = \sum_{m=1}^{a} W_m(\vec{X})\eta_m(t) \tag{2.26}$$

This coarse reduction neglects all the components for $m > a$. Therefore, because the eigenvalues are expressed in the form $\lambda_1 < \lambda_2 < ... < \lambda_a < ... < \lambda_\infty$, the high frequency component of the structural vibration are not taken into account. For this specific model reduction, the choice of the number of considered components depends on what is the purpose of the model (E.g. Numerical simulation, flight control system design, flight control system implementation), therefore on the accuracy required to the model and on the computational power available to execute numerical calculation using the reduced model. It is of key importance to analyse if the unmodelled frequencies can affect the rest of the model (E.g., aerodynamic coupling, servo actuator dynamic coupling) on which the structural vibration is integrated. Or in case the structural eigenmodes are used to design a control system, that the frequency contents of the measured signals have all the frequencies above $\sqrt{\lambda_a} = \omega_a$ filtered out.

The other two model reductions are obtained via theoretical procedures, starting from the integral formulation of the eigenvalue problem and are namely the Rayleigh-Ritz and the Galerkin method. These two methods, which are widely popular in the literature and are used for structure numerical simulations (Avanzini *et. al*, 2014,[2] and Malisani *et. al* [14]), differ from the just described ones since they approximate the solution of the integral formulation of the eigenvalue problem instead of calculating the close analytical solution and arbitrarily consider a certain amount of eigenfunctions. Therefore, instead of excluding components, the eigenvalue problem solutions are on purpose approximated to be kept limited in their number.

[1] For more information about expansion theorem, orthogonality and normalization of the shape modes please refer to [20], chapter 6 section 5.2 and 5.3

**Rayleigh-Ritz method** This method approximates the solution of the eigenvalue problem in the integral form as $w(\vec{X},t) = \sum_{i=1}^{n} u_i(\vec{X})\eta_i(t)$, where $n$ is the number of admissible functions $u_i(\vec{X})$. For this reason, this method is also called the *assumed modes method*, since the shape modes are assumed to be known. It is important to highlight that the assumed shape mode must satisfy the geometric boundary condition of the specific eigenvalue problem. Then, the total kinetic energy $T(t)$ and the total potential energy $U(t)$ of the flexible body are calculated respectively in equations 2.27 and 2.28.

$$\begin{aligned} T(t) = \frac{1}{2}\int_V M(\vec{X})[w((\vec{X},t))]^2 dV = \frac{1}{2}\sum_{i=1}^{n}\sum_{j=1}^{n} m_{ij}\dot{\eta}_i(t)\dot{\eta}_j(t) \\ m_{ij} = m_{ji} = \int_V M(\vec{X})u_i(\vec{X})u_j(\vec{X})dV \end{aligned} \tag{2.27}$$

$$\begin{aligned} U(t) = \frac{1}{2}\int_V f(\vec{X},t)\left[\int_V g(\vec{X},\xi)f(\xi,t)d\xi\right]dV \\ f(\vec{X},t) = \omega^2 M(\vec{X})w(\vec{X},t) \\ U(t) = \frac{1}{2}\tilde{\lambda}^2\sum_{i=1}^{n}\sum_{j=1}^{n} k_{ij}\eta_i(t)\eta_j(t) \\ k_{ij} = k_{ji} = \int_V M(\vec{X})u_i(\vec{X})\left[\int_V g(\vec{X},\xi)m(\xi)u_j(\xi)d\xi\right]dV \end{aligned} \tag{2.28}$$

where $\tilde{\lambda}$ describes the approximation of $\omega^2$, $f(\vec{X},t)$ is the distributed load depending on the spatial and time coordinates $\vec{X}$ and $g(\vec{X},\vec{\xi})$ is the flexibility influence function and $m_{ij} = m_{ji}$ and $k_{ij} = k_{ji}$ are a short nomenclature for the components of the kinetic energy and the potential energy sum respectively. This last function is a component obtained during the integration operation required to derive the integral form of the eigenvalue problem or the equation of motions [2]. Now that both the kinetic energy and the potential energy depend only on $n_i(t)$ generalized coordinates, with $i = 1,2,..,n < \infty$, it is possible to use Lagrange equation for a n-degree conservative system 2.29, which result in 2.30 when substituting 2.27 and 2.28 in 2.29.

$$\frac{d}{dt}\left(\frac{\partial T}{\partial \dot{\eta}_k}\right) - \frac{\partial T}{\partial \eta_k} + \frac{\partial U}{\partial \eta_k} = 0 \tag{2.29}$$

$$\sum_{i=1}^{n} m_{ki}\ddot{\eta}_i + \tilde{\lambda}^2\sum_{i=1}^{n} k_{ki}\eta_i = 0 \qquad k = 1,2,...,n \tag{2.30}$$

If considering harmonic variation of $\eta_i(t)$ then $\ddot{\eta}_i = -\tilde{\lambda}\eta_i$, equation 2.30 can be expressed as

$$\tilde{\lambda}[k]\vec{\eta} = [m]\vec{\eta} \qquad [k] = [k_{ij}] \qquad [m] = [m_{ij}] \tag{2.31}$$

where $[k_{ij}]$ and $[m_{ij}]$ are symmetric matrices and thus equation 2.1.5 can be solved to find the eigenvalue $\tilde{\lambda}$ and the corresponding eigenvectors $\vec{\eta}$

**Galerkin method** In the Galerkin method the integral form of the eigenvalue problem of the continuous system is considered and is described in equation 2.32. The function $\phi(\vec{X}) = \sum_{i=1}^{n} u_i(\vec{X})\eta_i = \sqrt{m(\vec{X})}W(\vec{X})$ is approximated by a linear combination of $n$ comparison functions $u_i(\vec{X})$

$$W(\vec{X}) = \lambda\int_V g(\vec{X},\vec{\xi})m(\vec{\xi})W(\vec{\xi})dV(\vec{xi}) \tag{2.32}$$

where $W(\vec{X})$ is the shape function or eigenfunction. If 2.32 is multiplied in both sides by $\sqrt{m(\vec{X})}$ then the following equation is obtained:

[2] For more information about flexibility influence function refer to [20], chapter 5 section 5.5

$$\begin{aligned} \phi(\vec{X}) &= \lambda \int_V K(\vec{X},\vec{\xi})\phi(\vec{\xi})dV(\vec{\xi}) \\ K(\vec{X},\vec{\xi}) &= g(\vec{X},\vec{\xi})\sqrt{m(\vec{X})}\sqrt{m(\vec{\xi})} \end{aligned} \tag{2.33}$$

where $K(\vec{X},\vec{\xi})$ is the symmetric kernel. When the approximate solution of $\phi(\vec{X}) = \sum_{i=1}^{n} u_i(\vec{X})\eta_i$ is inserted into 2.33, the equation does not hold anymore and a residual or error function can be defined as in equation 2.34, where $\tilde{\lambda}$ indicates the approximated value of the eigenvalue.

$$\varepsilon(\vec{X}) = \phi(\vec{X}) - \tilde{\lambda} \int_V K(\vec{X},\vec{\xi})\phi(\vec{\xi})dV(\vec{\xi}) \tag{2.34}$$

Then, to determine the coefficient $\eta_k$, $n$ extra constraints are added, each of those having the following structure, where $u_k(\vec{X})$ are used as weighting functions.

$$\int_v \epsilon(\vec{X})u_k(\vec{X})dV(\vec{X}) \qquad k = 1,2,...,n \tag{2.35}$$

Finally, by substituting 2.34 into 2.35 the result is

$$\sum_{i=1}^{n} \eta_i \int_V u_i(\vec{X})u_j(\vec{X})dV(\vec{X}) - \tilde{\lambda} \sum_{i=1}^{n} \eta_i \int_V u_k \left[ \int_V K(\vec{X},\vec{\xi})u_i(\vec{\xi})dV(\vec{\xi}) \right] dV(\vec{X}) = 0 \tag{2.36}$$

which can be further simplified into 2.38 when defining $[k]$ and $[m]$ as in 2.37

$$\begin{aligned} k_{ik} = k_{ki} &= \int_V u_k(\vec{X}) \left[ \int_V K(\vec{X},\vec{\xi})u_i(\vec{\xi})dV(\vec{\xi}) \right] dV(\vec{X}) \\ m_{ik} = m_{ki} &= \int_V u_k(\vec{X})u_i(\vec{X})dV(\vec{X}) \end{aligned} \tag{2.37}$$

$$\tilde{\lambda}[k]\vec{\eta} = [m]\vec{\eta} \tag{2.38}$$

Equation 2.38 is similar to the one obtained for the Rayleigh-Ritz method and can be solved using the same procedure.

## 2.2. Consequences of flexible modes in aircraft structure

Since the purpose of this literature survey is to analyse the interaction between structural eigenmodes, aerodynamic modes and flight control system, it is necessary to explain how flexible eigenmodes mutually interact with classical flight control system and unsteady aerodynamic. It comes by itself that a full review of the aerodynamic theory is out of the scope of this chapter. Thus, only the specific state-space representation currently used to describe the aforementioned interaction will be presented. First, the aerodynamic contribution in a rigid body state space for fixed-wing aircraft motion derived by the linearization of the Newton-Euler equation of motion will be described. Then, an example for the interaction between longitudinal modes FCS and flexible dynamics will be presented. Later, flexible modes will be introduced in the plant dynamics, an aeroelastic model will be derived and unstable aeroelastic effects will be presented.

### 2.2.1. Rigid aircraft state space derivation

Rigid body aircraft state-space representation is one of the simplest and certainly the most widely used. It is based on the Newton-Euler equations of motion for an aircraft, as extensively discussed in Moulder (2013) [16]. The aforementioned equation can be linearized around different trim conditions depending on the flight state or manoeuvre to be analyzed. In this specific case, the chosen trim condition is the steady, straight, symmetric flight condition. In the following pages the hypothesis behind this basic state-space representation is outlined and the most relevant equation will be reported.

#### Simplifying hypothesis

The assumptions made for the derivation of the rigid aircraft state space are:

- The aircraft is a rigid body
- Vehicle mass and inertial momentum are constant
- The Earth is assumed to be flat and non-rotating
- The body-fixed reference frame is chosen such that $I_{xy}$ and $I_{yz}$ are zero, thus the $X_b - Z_b$ body plane is a plane of mass symmetry
- The effects of rotating masses are neglected
- There is no wind, therefore $\vec{V}_{ground} = \vec{V}_{air}$
- Thrust vector lies in the symmetry plane and thus it only contributes in the external force on the $X^b$ and $Z^b$ and the external moment around the $Y^b$, as shown in figure 2.1

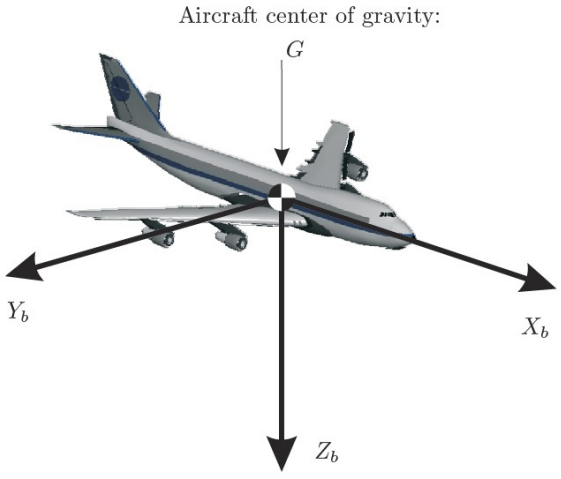


**Figure 2.1:** Body reference frame representation (Mulder 2013 [16])

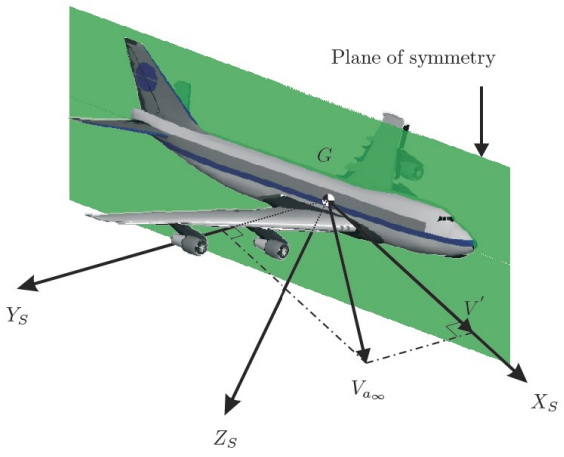


**Figure 2.2:** Stability reference frame representation (Moulder 2013 [16])

Newton-Euler equations of motion are expressed in body reference frame, shown in figure 2.2, for sake of simplicity as follows

$$m\dot{\vec{V}}^b + m\vec{\omega}\times\vec{V}^b = mT_E^b\vec{g} + F_{ext}^b \longrightarrow \begin{bmatrix} m(\dot{u}+qw-rv) = -W\,sin\theta + X = F_x \\ m(\dot{v}+ru-pw) = -W\,cos\theta\,sin\varphi + Y = F_y \\ m(\dot{w}+pv-qu) = -W\,cos\theta\,cos\varphi + Z = F_z \end{bmatrix} \tag{2.39}$$

$$I\dot{\omega} + \vec{\omega}\times I\vec{\omega} = \vec{M}_{ext} \longrightarrow \begin{bmatrix} I_{xx}\dot{p} + (I_{zz}-I_{xx})qr - I_{xz}(\dot{r}+pq) = M_x = L \\ I_{yy}\dot{q} + (I_{xx}-I_{zz})rp - I_{xz}(p^2-r^2) = M_y = M \\ I_{zz}\dot{r} + (I_{yy}-I_{xx})pq - I_{xz}(\dot{p}+rq) = M_z = N \end{bmatrix} \tag{2.40}$$

$$\begin{aligned} \dot{\varphi} &= p + q\,sin\varphi\,tan\theta + r\,cos\varphi\,tan\theta \\ \dot{\theta} &= q\,cos\varphi - r\,sin\varphi \\ \dot{\psi} &= q\,\tfrac{sin\varphi}{cos\theta} + r\,\tfrac{cos\varphi}{cos\theta} \end{aligned} \tag{2.41}$$

where $\vec{\omega} = [p, q, r]^T$ is the rotation rate of the body reference frame expressed in body coordinates. $[\varphi\,\theta\,\psi]$ are the Euler angles and $\vec{V} = [u, v, w]^T$ is the airflow speed. $I$ is the moment of inertia matrix and $m$ is the mass of the aircraft. The aerodynamic forces and moments, namely $[X, Y, Z, L, M, N]$, are regarded as function of the linear and angular velocities and of the control surface deflections $\vec{\delta} = [\delta_a, \delta_e, \delta_r, \delta_t]^T$ and all the time derivatives of the aforementioned quantities. Thus we can restate equation 2.39 as 2.42 and equation 2.40 as 2.43

$$\begin{aligned} F_x &= f_x(W,\theta,X(\vec{\delta},\vec{V},\vec{\omega})) = g_{fx}(\dot{u},\vec{V},\vec{\omega}) \\ F_y &= f_y(W,\theta,\varphi,Y(\vec{\delta},\vec{V},\vec{\omega})) = g_{fy}(\dot{v},\vec{V},\vec{\omega}) \\ F_z &= f_z(W,\theta,\varphi,Z(\vec{\delta},\vec{V},\vec{\omega})) = g_{fz}(\dot{w},\vec{V},\vec{\omega}) \end{aligned} \tag{2.42}$$

$$\begin{aligned} M_x &= L(\vec{\delta},\vec{V},\vec{\omega}) = g_{mx}(\vec{\omega},\dot{\vec{\omega}}) \\ M_y &= M(\vec{\delta},\vec{V},\vec{\omega}) = g_{my}(\vec{\omega},\dot{\vec{\omega}}) \\ M_z &= N(\vec{\delta},\vec{V},\vec{\omega}) = g_{mz}(\vec{\omega},\dot{\vec{\omega}}) \end{aligned} \tag{2.43}$$

Thus, the state vector is defined as $\vec{X} = [\vec{V}^T, \vec{\omega}^T, \varphi, \theta, \psi]^T$ and the input vector is $\vec{u} = \vec{\delta}$. Then equations 2.43 and 2.42 can be linearized and they become dependent only on $\Delta\vec{X}$ since the contributions of $\Delta\vec{X}_0$ cancels out due to the definition of steady-state condition. When linearized, the equation of motion can be decoupled in symmetric and asymmetric motion, due to the consideration that in the linearized system description, disturbances (forces or moments) laying in the symmetry plane $X_b - Z_b$ do not influence the asymmetric motion. Similarly, disturbances laying outside the symmetry plane do not influence symmetric motion. Therefore, the aerodynamic is decoupled and two different sub-state-space are obtained by grouping the Newton-Euler equations as follows: for the symmetric motion equations for $F_x, F_z$ and $M_y$ are considered. For the asymmetric motion the remaining $M_x, M_Z$ and $F_y$ equation constitute the asymmetric motion sub-state space. For sake of convenience the stability frame is introduced, the equations are made non-dimensional and some algebraic manipulation is operated to obtain states which are more intelligible and which can explicitly show aerodynamic states. Also the kinematic equations 2.41 are linearized and included in the two sub-state spaces. Below the symmetric aircraft motion 2.44 and the asymmetric one 2.45 are reported in the classical state space form $\dot{\vec{X}} = A\vec{X} + B\vec{u}$.

$$\begin{bmatrix} \dot{\hat{u}} \\ \dot{\alpha} \\ \dot{\theta} \\ \frac{q\bar{c}}{V} \end{bmatrix} = \begin{bmatrix} x_u & x_\alpha & x_\theta & 0 \\ z_u & z_\alpha & z_\theta & z_q \\ 0 & 0 & 0 & \frac{V}{\bar{c}} \\ m_u & m_\alpha & m_\theta & m_q \end{bmatrix} \begin{bmatrix} \hat{u} \\ \alpha \\ \theta \\ \frac{q\bar{c}}{V} \end{bmatrix} + \begin{bmatrix} x_{\delta_e} & x_{\delta_t} \\ z_{\delta_e} & z_{\delta_t} \\ 0 & 0 \\ m_{\delta_e} & m_{\delta_t} \end{bmatrix} \begin{bmatrix} \delta_e \\ \delta_t \end{bmatrix} \tag{2.44}$$

$$\begin{bmatrix} \dot{\beta} \\ \dot{\varphi} \\ \frac{\dot{p}b}{2V} \\ \frac{rb}{2V} \end{bmatrix} = \begin{bmatrix} y_\beta & y_\varphi & y_p & y_r \\ 0 & 0 & 2\frac{V}{b} & 0 \\ l_\beta & 0 & l_p & l_r \\ n_\beta & 0 & n_p & n_r \end{bmatrix} \begin{bmatrix} \beta \\ \varphi \\ \frac{pb}{2V} \\ \frac{rb}{2V} \end{bmatrix} + \begin{bmatrix} 0 & y_{\delta_r} \\ 0 & 0 \\ l_{\delta_a} & l_{\delta_r} \\ n_{\delta_a} & n_{\delta_r} \end{bmatrix} \begin{bmatrix} \delta_a \\ \delta_r \end{bmatrix} \tag{2.45}$$

Although this state-space representation has been successfully utilized for a very long time and still accurately represent the rigid body motion of an aircraft flying in a steady, straight and symmetric flight condition, due to the rigid body assumption, the coupling between aerodynamic and flexible eigenmodes is not present because the structural modes are not modelled. The consequences of not considering structural eigenmodes are multiple. Firstly, whatever unstable mode related to the aerodynamic-structure interaction cannot be stabilized. Moreover, regardless of how stiff the fuselage and wing structures are or if the structural modes are critically or over-damped by nature, those will still be measured by the sensors utilized to close the feedback control loop, for the Stability Augmentation System (SAS). This basically introduces a new dynamic, namely the structural one, on the feedback loop. Generally speaking, if the natural frequency of the measured bending mode is much higher than the rigid body eigenmotion frequency then the FCS will filter out the structural mode contribution due to its own low pass filter characteristics.

If the natural frequency of the structural eigenmodes is close or lower than the cut-off frequency of the FCS, some interactions can be experienced. For high gain controllers, the flexible mode could enter in a divergent resonance with the FCS internal dynamics. For high-performance aircraft with high feedback gain and which are design to be statically unstable in order to achieve higher manoeuvrability, this hidden interaction could make the whole system unstable. A very detailed description of such a case is developed and thoroughly discussed by Tewari (2015) in Chapter 5.6.1,[27]. In this example, a SAS for unstable short period[3]eigenmotion is designed. The short period mode approximation is used as aircraft model, alongside an elevator actuator with a second-order dynamic and four structural modes considered to fall within the bandwidth of the closed-loop control system, which is identified as $\omega_c \approx 10\,\text{Hz}$. The accelerometer measuring the load factor $a_z$ is placed behind the centre of gravity of the aircraft. This makes the state space system a non-minimum phase one. Then a state observer is implemented using a Kalman filter approach. Finally, the control loop is closed with a linear control law together with a feed-forward gain, stabilizing the short period eigenmode. The control system is designed to stabilize the short period motion, while it is completely neglecting the aeroelastic modes. It is shown that before the implementation of the control loop, only the poles related to short period eigenmotion were on the right-hand plane, while both the aeroelastic and the actuator poles were stable. However, the neglecting of structural eigenmodes during the FCS design moved the aeroservoelastic poles to the right side of the imaginary plane. This leads to a normal acceleration of 15 g being measured after just 0.5 s, while the rigid body short period approximation model should have a settling time of about 2 s. Is mentioned by Tewari that this very mistake has been responsible for the crashes of several fighter prototypes, such as Lockheed F-22. Moreover, this kind of aircraft which has high gain feedback usually has a wide flight envelope which can include regions where aeroelastic effects become prominent, as will be discussed in the next section.

### 2.2.2. Aeroelastic phenomena - finite state space representation

When flying at specific flight conditions, the interaction between deformable aircraft structure and unsteady aerodynamic can lead to self-excited aeroelastic phenomena such as flutter, limit cycle oscillation, free body oscillation and divergence. These phenomena can be generated by different occurrences, such as a change of density in the air or a change in flight speed, or by a gust acting as an impulse for a specific aeroelastic mode. Moreover, those can be oscillatory dynamics with constant amplitude or very low damping coefficient or can be exponentially divergent motions. In order to describe these phenomena and eventually to design a control system that can damp down and/or avoid the interaction with those, it is of key importance to derive a state-space representation.

In the early '40s, aircraft started to be build using metallic materials, known to have an elastic behaviour close to the theoretical elastic representation. Moreover, airplanes began to reach speeds comparable to the sound speed in the air. The combination of fuselages and wings being "long" and "thin" structures which could elastically bend under the excitation of high inertial and aerodynamic loads and the capability of generating such loads due to the ability to reach high airspeed generated the first event of aeroelastic phenomena. Therefore, some early aeroelastic models were developed to describe the time behaviour of such a structure. The main goal of calculating the time response is to determine which and where are the boundaries that separate damped structural motion from the divergent one, which will ultimately lead to a failure in the structure. However, the calculations of the structural time response coupled with unsteady aerodynamic are highly coupled linear partial derivative equations, which require

[3]For more detailed information on short period approximation, please refer to Mulder (2013) [16]

a great number of iterations and computational power to be solved accurately enough. Thus, to model the aerodynamic is preferred to derive a Laplace domain description and then numerically integrate it to obtain the time response.

One of the early attempts to describe unsteady aerodynamic phenomena to successively couple those with structural model to obtain an aeroelastic phenomena mathematical description was carried out by Theodorsen (Tewari 2015 ), with the analysis of a bi-dimensional wing in an incompressible, two-dimensional airflow of speed U. The airfoil only has two degrees of freedom: one in the pitch angle $\theta$ (angle between the chord line and the air stream direction) and one in the plunge direction (linear displacement perpendicularly to the airflow direction). The lift has two contribution in the frequency domain, one due to the circulatory stream and one due to the non-circulatory stream The second contribution is neglected due to its smaller magnitude with respect to the circulatory one. Theodorsen related the circulatory lift to the upwash, $w(ik)$, induced by the wake

$$\ell(ik) = \ell_c(ik) = C(ik)w(ik) \qquad C(ik) = \frac{\int_1^\infty \frac{x}{\sqrt{x^2-1}} e^{-ikx}\,dx}{\int_1^\infty \frac{x+1}{\sqrt{x^2-1}} e^{-ikx}\,dx} = \frac{H_1(k)}{H_1(k)+H_0(k)} \tag{2.46}$$

where in 2.46 $H_x$ is the Hankel function of the second kind of order $x$

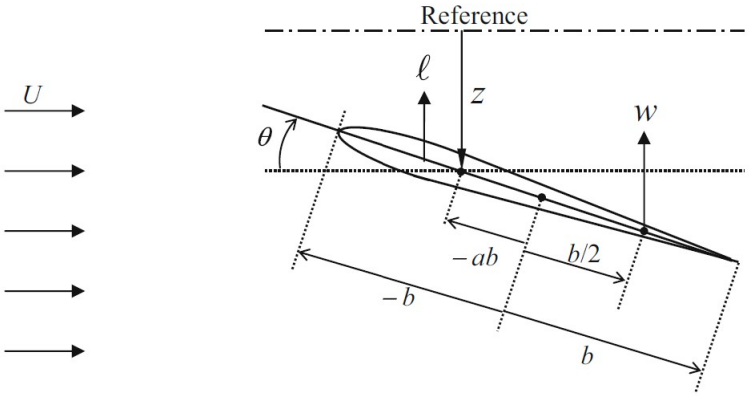


**Figure 2.3:** Cinematic of Theodorsen bi-dimensional system analysis (Tewari, 2015 [27])

To obtain the function $C(ik)$, Theodorsen derived first the non-circulatory potential $\Delta\phi_{nc}$ as the flow potential on a circular surface with a flow source and a flow sink placed diametrically opposed positions in the surface. Later, Theodorsen defined the circulatory potential $\Delta\phi_c$ such as it would cancel the circulatory contribution. Both the integrals related to the non-circulatory and circulatory potentials were solved by the used of conformal mapping. "The circulatory pressure difference on the airfoil is derived by accounting for the fact that the unsteadiness in the velocity potential is caused only by the motion of wake" Tewari 2015 [27]. Regardless this simplification, the circulatory pressure difference formula still contains a difficult integral to solve, which was approximated by Theodorsen with the left equation in 2.46[4]. From the airfoil kinematic described in figure 2.3 we can derive the wake equation

$$\begin{aligned} w(t) &= \dot{z} + U\theta + b\left(\tfrac{1}{2} - a\right)\dot{\theta} & z(t) &= z_0 e^{ikt} \\ w(ik) &= ikz_0 + \left[U + ikb\left(\tfrac{1}{2} - a\right)\right]\theta_0 & \theta(t) &= \theta_0 e^{ikt} \end{aligned} \tag{2.47}$$

It is worth to mention that frequency considered is a non-dimensional reduced frequency $k = \omega b/U$. The Theodorsen function represents the transfer function relating the wake, or angle of attack if $\alpha(ik) = w(ik)/U$, and the lift in the frequency domain. Thus, it can be generalized as a linear aerodynamic operator using analytical continuation. Since the transfer function is considered to have negative poles, the time response function calculated by the inverse Fourier transform of the Theodorsen function can be expressed as a Wagner function of the non-dimensional time $\tau = U\,t/b$

$$\Phi(\tau) = 1 + \frac{2}{\pi}\int_0^\infty \frac{C(ik)-1}{ik} e^{ik\tau}\,dk \tag{2.48}$$

[4]For more information about the derivation of the Theodorsen function, please refer to Theodorsen (1935) [28]

Jones approximation of Wagner function $\Phi(\tau) \approx 1 - 0.165\,e^{-0.0455\tau} + -0.3352\,e^{-0.3\tau}$ shows that a series of exponential decaying function in the adimensional time domain is used (Tewari 2015 [27]). Proceeding with the analytical continuation process, the frequency variable $ik$ is substituted by the Laplace variable $s = \sigma + ik$. Hence, the Theodorsen function can be expressed in the Laplace domain as

$$C_a(s) = \frac{N(s)}{D(s)} = a_0 + \sum_{n=1}^{N} \frac{a_n\, s}{s + b_n} \tag{2.49}$$

and the Wagner function is approximated as

$$\Phi(\tau) \approx a_0 + \sum_{n=1}^{N} a_n\, e^{-b_n\,\tau} \tag{2.50}$$

where the coefficient $a_x$ and $b_x$ are calculated by curve fitting using a least squared process. The squared fit error over a set of selected frequencies is the quantity to be minimized with respect to the numerator coefficients. The just depicted Theodorsen function approximation is the simplest one. Throughout the years more approximations have been successfully implemented, with an increase in accuracy. Regardless of the approximation method, the result is a function in Laplace domain built as a summation of rational functions. Thus, this approximation method is called rational function approximation (RFA). From a state-space representation point of view, it is easy to translate a series of rational transfer function into a state-space description.

The aforementioned transient aerodynamic response was developed just for the wing section, while to obtain a better approximation a three-dimensional wing should be considered. In the '50s and '60s, the Theodorsen function formulation for wing strips was first applied throughout the length of the wing, by breaking the wing itself into a finite number of chordwise rigid strips. Each strip had the two d.o.f. of the one in fig 2.3 and was connected to the neighbours strip with a linear and rotational spring. Moreover, the equations for the system in 2.3 were derived also for flow condition different from the non-compressible steady airflow condition. Later during the '70s, the Laplace domain RFA technique was enhanced to describe the transient response of a three-dimensional lifting surface. Then, a finite state aerodynamic model for a 3-D wing, still based on exponential series type approximation but combined with a series approximation of the continuous wing and fuselage structure using a finite number of structural modes was available. This led to the possibility to calculate a transfer matrix in the Laplace domain $G(s)$, which relates the structural finite number of states $\vec{q}(s)$ to the unsteady aerodynamic generalized force vector $\vec{Q}(s) = G(s)\vec{q}(s)$. As an example for the Laplace domain transfer function matrix, here is presented the calculation technique elaborated by Sevart, Roger et al. with the pole optimization by Tiffany, Adam, Tewari and Eversman, as reported by Tewari (2015) in [27].

$$G(s) = A_0 + A_1 s + A_2 s^2 + \sum_{j=1}^{N} A_{j+2} \frac{1}{s + b_j} \tag{2.51}$$

with $A_j$ numerator coefficient matrices. The fitting of $G(s)$ can be carried out with the same procedure of the RFA, where a fitting error between the Laplace domain transfer function and the aerodynamic data is defined over an a priori defined set of frequencies. The aerodynamic data are calculated using the doublet-lattice model, which is an analytically derived solution for the governing equations of lift distribution and upwash for linearized compressible flows. The linearization process implies that the aerodynamic data are significant only around the steady-state condition around which the equations have been linearized. Thus, if an aircraft has a wide flight envelope, multiple Laplace domain transfer matrices need to be calculated. Then, a minimization is carried out using again a least square method. It must be highlighted that the number of poles $N$ is arbitrary and that the optimization procedure must be carried out multiple times to obtain a proper transfer function approximation. On each iteration of the method, the position of the poles is checked to avoid having poles with almost identical values, which will eventually result in a non-consistent state-space representation. The whole method can be summarized as the following procedure:

1. Structural characterization of the aircraft via theoretical calculation or ground vibration test and following model reduction using approximation methods (e.g. Galerkin method)

[4] For more detailed information, refer to Tewari 2015 [27], Chapter 3

2. Calculation of aerodynamic data using "Lifting surface theory"
3. Calculation of the aerodynamic Laplace domain transfer matrix
4. Evaluation of the reached level of accuracy and analysis of poles position
5. If the result does not fit the data well enough, restart from (3)

Now that the interaction between the structural modes and the aerodynamic is characterized, it is possible to derive a general state-space representation for the aeroservoelastic system. Defining $\vec{q}(s)$ as the vector of structural modes generalized coordinates and $\vec{Q}(s)$, $\vec{Q}_c(s)$ as aerodynamic forces, respectively due to aerodynamic states and to the deflection of control surfaces, the state space and its components can be represented as follows

$$\begin{aligned} M\ddot{\vec{q}} + C\dot{\vec{q}} + K\vec{q} &= \vec{Q} + \vec{Q}_c \\ \vec{Q} &= M_a\ddot{\vec{q}} + C_a\dot{\vec{q}} + K_a\vec{q} + N_g\vec{x}_g + N_a\vec{x}_a \end{aligned} \tag{2.52}$$

where $M$, $C$, $K$ are the inertia, damping and stiffness matrices for the structural modes, $M_a$, $C_a$, $K_a$ are the generalized aerodynamic inertia, aerodynamic damping, and aerodynamic stiffness matrices, respectively. In 2.52 the gust state vector $\vec{x}_g$ is mentioned for sake of completeness but it will not be considered from now on. Finally, $\vec{x}_a$ is the aerodynamic lag state vector. When considering a three-dimensional wing and the Laplace domain transfer function obtained via data fitting, 2.52 becomes 2.53 when we substitute $\vec{Q}(s) = G(s)\vec{q}(s)$, which describes only the lift due to the circulatory and non-circulatory flow, neglecting the gust dynamics.

$$\begin{aligned} (Ms^2 + Cs + K)\vec{q}(s) &= \left[ A_0 + A_1 s + A_2 s^2 + \sum_{j=1}^{N} A_{j+2}\frac{1}{s+b_j} \right]\vec{q}(s) + \vec{Q}_c(s) \\ G(s)\vec{q}(s) &= M_a\ddot{\vec{q}} + C_a\dot{\vec{q}} + K_a\vec{q} + N_a\vec{x}_a \end{aligned} \tag{2.53}$$

$$\begin{bmatrix} \dot{\vec{q}} \\ \ddot{\vec{q}} \end{bmatrix} = \begin{bmatrix} 0 & I \\ -\bar{M}^{-1}\bar{K} & -\bar{M}^{-1}\bar{K} \end{bmatrix}\begin{bmatrix} \vec{q} \\ \vec{q} \end{bmatrix} + \begin{bmatrix} 0 \\ -\bar{M}^{-1}N_a \end{bmatrix}\vec{x}_a + \begin{bmatrix} 0 \\ -\bar{M}^{-1} \end{bmatrix}\vec{Q}_c \tag{2.54}$$

where the lag state $\vec{x}_a$ has its own dynamic, which takes the structural generalized coordinates as inputs, as shown in equations 2.55

$$\dot{\vec{x}}_a = A_a\vec{x}_a + \Gamma_a\begin{bmatrix} \vec{q} \\ \vec{q} \end{bmatrix} \tag{2.55}$$

When equations 2.54 and 2.55 are put together, the resulting state space is

$$\begin{bmatrix} \dot{\vec{q}} \\ \ddot{\vec{q}} \\ \dot{\vec{x}}_a \end{bmatrix} = \begin{bmatrix} 0 & I & 0 \\ -\bar{M}^{-1}\bar{K} & -\bar{M}^{-1}\bar{C} & -\bar{M}^{-1}N_a \\ \Gamma_a & & A_a \end{bmatrix}\begin{bmatrix} \vec{q} \\ \dot{\vec{q}} \\ \vec{x}_a \end{bmatrix} + \begin{bmatrix} 0 \\ -\bar{M}^{-1} \\ 0 \end{bmatrix}\vec{Q}_c \tag{2.56}$$

Generally speaking, the values and structure of the matrices $A_a$, $N_a$ and $\Gamma_a$ depend on the calculation method applied to obtain the Laplace domain transfer matrix $G(s)$. By recalling the structure of $G(s)$ from equation 2.51 the relations in 2.57 come along

$$\begin{aligned} \bar{M} &= M - M_a = M - A_2 \\ \bar{C} &= C - C_a = C - A_1 \\ \bar{K} &= K - K_a = K - A_0 \\ N_a &= [A_3, A_4, ..., A_N] \end{aligned} \tag{2.57}$$

Where $A_3$, $A_4$, ... , $A_{N_2}$ are $n \times n$ matrices. This leads equation 2.55 express matrices $A_a$ and $I_n$ as

$$A_a = \begin{pmatrix} -b_1 I_n & 0 & 0 & \cdots & 0 \\ 0 & -b_2 I_n & 0 & \cdots & 0 \\ \vdots & \vdots & \vdots & \vdots & \vdots \\ 0 & 0 & 0 & \cdots & -b_N I_n \end{pmatrix} \quad \Gamma_a = \begin{pmatrix} I_n \\ I_n \\ \vdots \\ I_n \end{pmatrix} \tag{2.58}$$

It is extremely important to keep in mind that the Laplace domain transfer function calculation is carried out with frequency data obtained from the linearization of aerodynamic equations around a specific airflow condition. Therefore, even if the equations are made non-dimensional during the calculations, it is of key importance to fix quantities such as airspeed, Mach number and air density at the beginning of the aerodynamic state-space representation process. The control surfaces can be modelled as a dynamic system, and their dynamics can be included in the state space description. Usually, actuator dynamic is modelled as second-order systems subjected to external excitation. Extra aerodynamic states can be added to better describe the mutual effect between the control surface deflection and the other component of the state space such as structural eigenmodes and unsteady aerodynamic.

When the aeroelastic interactions are considered and modelled as in the previous pages, it is possible to design SAS which does not inadvertently excite dangerous structural modes, as it can happen in the example discussed by Tewari (2015) in Chapter 5.6.1 [27] and briefly reported at the end of section 2.2.1.

Moreover, by analysing the just obtained linear representation of an aeroelastic system, lightly damped or unstable oscillatory eigenmodes related to the flexible or aerodynamic states can be highlighted. As described by Livne (2018) in [12], current flight conditions, Mach number, altitude, load factor and other manoeuvre parameters can influence the nature of the experienced aeroelastic phenomena. Flutter and divergence are two main aeroelastic phenomena related to a linear representation of the aircraft system. Those can be oscillatory at a constant amplitude, with amplitude meaning the displacement of the structure from its undeformed configuration, or divergent. Both can lead to violent dynamics generating structural deformations which can eventually induce structural failures. Via linear aeroelastic analysis, it is possible to determine the "flutter boundary", which is the airspeed or dynamic pressure value, below which the flutter phenomenon is stable and damped and above which the same phenomenon is self-sustained, and it can violently diverge. It is also possible to determine the so-called "flutter region", which is a sub-region of the flight envelope in which flutter oscillations can be experienced. Moving forward from the linear phenomena, other aeroelastic effects due to the presence of non-linearity in the system have been recorded and studied over the years. Nonlinearities are introduced in multiple ways such as excessive structural deformation which are not accurately described by linear structural theory, presence of shock waves or flow separation, presence of non-linearity in the actuators (free play for example) or damping nonlinearities (Livne, 2018 [12]).

The presence of nonlinear phenomena generates additional self-excited oscillation like Limit Cycle Oscillations. Unlike flutter and divergence, LCOs arise at lower airspeed with respect to linear aeroelastic phenomena, but the oscillations generated have a limited amplitude, which can be sustained from the aircraft structure for some time, with the hypothesis of excluding structural failure due to fatigue. LCO can become flutter phenomena due to an increase in the airspeed or in the dynamic pressure. Moreover, as described by Dowell et al (2003) in [7], the presence of non-linearities introduce hysteresis behaviour on the airspeed - LCO amplitude relations. Thus, the airspeed at which LCO starts from a previous non-oscillatory condition is higher than the airspeed at which LCO are stabilized and damped out.

# Survey on structural modes - flight control systems interaction avoidance techniques

In this chapter, the results of the literary survey conducted on which solutions have been implemented to counteract the issue generated by the presence of structural eigenmodes will be discussed. The standard procedure to design a flight control system has been to design a flight control system to stabilize the rigid body motions and, if necessary, to add a separate control system to damp or cancel flexible aircraft modes. The goal of this procedure is to reduce the dimension and the complexity of the control task into two smaller problems. This separation implies that it is possible to separately measure only the rigid body and the flexible motions. In some cases, the flexible motion is willingly neglected and cancelled out from the sensor's measurement signal. In other cases, observers are designed to provide a separate description for both motions. Lately, the flight control system design has shifted towards an approach that integrates it with the aerodynamic and structural design of the aircraft (Becker, Caldwell and Vaccaro, 2014) [3]. Thus, the control of the aeroelastic motions must be implemented. This chapter is structured as follows: first, the implementation of notch filters for flexible mode signal cancellation will be described and both strengths and flaws will be highlighted. Later, solutions for damping of aeroelastic phenomena will be discussed. Finally, some significant papers describing control system design for flexible aircraft will be presented and discussed.

## 3.1. Notch filters

With the term "Notch Filter" are pointed all those systems that can reduce the magnitude of a signal around a specific frequency. The implementation of such a filter can reduce the influence of the structural modes in the acceleration measurements by cancelling the frequency contribution of the flexible eigenmodes. This solution has been widely implemented to comply with certifying agency specifications, which recommend attenuation for elastic modes [8]. The goal of the implementation of notch filters is to avoid interactions of aeroelastic dynamics with the flight control system designed only for rigid body motion stabilization and control.

Some key points must be highlighted. Firstly, it is worth explicitly mention the underlying hypothesis behind the use of notch filters. The hypothesis is that the poles of the rigid body motions and of the flexible eigen motions are separated enough so the filter action does not affect the rigid body motion. Otherwise, the notch filter would also cancel the frequency contribution of the rigid body dynamics, making it impossible for the sensors to properly provide an accurate description of the current rigid aircraft states. In short, if the natural frequencies of the rigid and flexible eigenmodes have values that are too similar to one another, the notch filter would cancel both out. Secondly, the introduction of such a filter into the feedback signal will introduce a phase lag in the aforementioned signal. As shown by Wei Xu et al. (2019) in [33], if the numerator and the denominator of the notch filter transfer function have the same polynomial order, then the phase shift is reduced in amplitude and experienced only around the frequency cancelled by the filter if compared to common low pass filter. On the other side, if the denominator of the filter transfer function has a higher polynomial degree than the numerator, and depending on the transfer function structure, the lag effect can be significant. Notch filters are used by Mooij (2020) in [15] to compensate for the effect of flexibility on gyroscope measurement in space launch systems. In this particular case, the first longitudinal bending mode contribution is removed by the pitch rate measurements. Mooij also mentions that it is possible to design an adaptive notch filter to counter incomplete or partial knowledge of the flexible modes [9]. Moreover, it is clear from the graphs in [15] that the notch filter implementation adds some phase lag in the pitch rate time signal. In [22], Silvestre et al. (2017) show what are the effects of applying a notch filter to neglect the aeroelastic contribution after the implementation of the close loop of the SAS, as that is standard practice in the current aeronautical industry. In the paper, it is acknowledged that the implementation of several notch filters in a single system leads to a decrease in stability margins. Moreover, the implementation of notch filters requires knowledge of the characteristics of the structural

bending modes to be filtered out. Regardless of the proven effectiveness of the notch filter solution, most of the research on flight dynamic and flight control system design is moving away from the use of such a filter due to the increase in flexibility of more recent aircraft model and the consequent decrease of the natural frequencies of the firsts structural bending modes, which leads to a smaller separation between the structural modes frequencies and rigid body frequencies.

## 3.2. Unstable aeroelastic phenomena - flutter suppression

As already mentioned in 2.2.2, for unstable high-performance aircraft flight control system design stabilization of aeroelastic modes must be implemented, since their mission specifically requires a flight envelope containing a non-negligible flutter region. Dangerous eigen motion can be stabilized either using passive or active flutter suppression. Inside the passive flutter suppression definition are included techniques such as structural stiffening and mass distribution management. The implementation of such solutions is quite unpractical, usually it leads to an increase in the aircraft mass and its adaptation to later changes in aircraft configuration it is complex and expensive.

Inside the active flutter suppression (AFS) techniques definition are included all the aeroelastic motions damping solutions requiring actions on the system by the (automatic) controller via actuators. Before starting the discussion on ASE control technique, it must be mentioned that to perform a feedback control action on such a system, it is necessary that the actuator dynamics are fast enough to effectively provide inputs in the aeroelastic system and that the available sensors can measure most of the structural eigen motions, or at the very least the ones which are required to be suppressed.

### 3.2.1. Active flutter suppression

After having obtained a state-space representation as in 2.2.2, it is possible to apply known LTI control techniques to achieve the desired performances. As reported by Livne (2018) in [12], multiple control law synthesis approaches have been implemented for linear aeroservoelastic flutter suppression, such as Nyquist, Nichols and Bode compensation methods, linear quadratic regulator/linear quadratic Gaussian and pole placement. Moreover, also model-free controllers have been implemented based on a linear aeroservoelastic representation using fuzzy controllers and neural networks.

Due to the need for a control system that is able to stabilize flutter in the entire flight envelope, adaptive AFS is the most desirable solution. With adaptive, it is depicted a control system that not only can act with specific control strategies depending on the flight condition but which can also detect failure and changes in the aeroelastic model and act accordingly. Gain scheduling has been implemented, showing to be a reliable solution to provide adequate AFS throughout different flight phases, although not being adequate to respond to failure occurrences. In [27], Tewari (2015) shows that once the linearized ASE system representation is obtained, it can be stabilized using linear feedback control law together with a state observer. Then, also optimal control solutions using Hamilton-Jacobi-Bellman equation, Kalman filters, robust control techniques such as linear quadratic Gaussian with loop transfer recovery and $H_2/H_\infty$ and infinite horizon linear optimal control techniques are suitable to stabilize aeroelastic oscillations (Tewari 2015, [27]). Almost all the aforementioned solutions require the implementation of a state observer based on the aeroelastic model, thus state estimation plays a key role. Because of the use of linear aeroelastic model for the control system design, linear state observer is the most common. Recently, other state observer solutions have also been implemented, such as "Extended State observer" and "Generalized extended state observer" which can be applied to nonlinear systems and can reject non-modelled plant dynamic by considering those as disturbances (Radke and Gao, 2006) [19]. Since most of the aeroservoelastic studies have been carried out on aircraft size flying vehicles, such as experimental fighter XF-18, space launcher and HALE NASA test vehicle, there has not been lack of space for sensor placement. Thus, most of the literature about aeroelastic control implicitly assumes that all the structural and aerodynamic states of the selected aeroelastic model are observable and can be measured. This condition is not verified in the case of micro air vehicles where space and weight are two major issues and sensors cannot be easily placed everywhere in the airframe.

## 3.3. Examples of flight control system design accounting for aeroelastic effects

Aeroservoelasticity is a complex and extensive topic, which is present in every aspect of flight control system design, starting from system modelling, moving to the actual design of the FCS and finally to the sensing and actuation tasks. Due to a large number of possible solution combinations, it is very challenging to provide a complete and exhaustive dictionary of all the aeroelastic modelling methods, aeroelastic control strategies and aeroelastic state estimator techniques and is not within the goals of this document. Therefore, a selection of relevant paper about aeroelastic modelling and control will be briefly described and discussed. The papers have been selected to describe solutions different from one another to

In [18], Paranjape et al. (2012) model the wings of a a tail-less MAV with flexible articulated wings as Euler-Bernoulli linear elastic beam being able to twist around the span direction and to bend along the vertical body direction. The aerodynamic model is derived according to the one developed by Goman and Khrabrov (Goman *et. al* 1992, [10]). This aerodynamic model is preferred to the more utilized Theodorsen aerodynamic approximation because it is simpler to implement, it is constituted by one ordinary differential equation (ODE), it is nonlinear and it captures hysteresis behaviour of lift coefficient due to periodic variation on the angle of attack. Finally, this aerodynamic model describes the change in lift as function of the wingspan coordinate. Moreover, because of the morphing wing, the changes in the position of the centre of gravity are considered. An interesting observation arises from the analysis of the first bending and torsion modes natural frequencies. It is shown that the ratio of the first torsional mode frequency and the first bending mode frequency is proportional to the airspeed to structural Young modulus ratio.

$$\frac{\omega_\theta}{\omega_\xi} \propto \frac{V}{E} \tag{3.1}$$

where $E$ is the Young modulus of the wing and $V$ is the airspeed. Thus, depending on the value of the frequencies ratio, the time scale separation principle con be applied to decouple the two dynamic. Therefore, the design of control systems for aeroelastic mode stabilization of the first torsional and bending mode can be executed separately. The flight control system used for these analyses is explicitly mentioned. However, Paranjape et al. show that taking into account also structural dynamics does not significantly improve flight performances. Moreover, the rigid body dynamic stability investigated in simulation including flexible dynamics is not different from the one experienced in simulations where structural modes were neglected. Finally, Paranjape et al. point out that, generally speaking, "MAVs are usually designed to fly at relatively slower speeds, and hence it is reasonable to expect that a large degree of flexibility can be safely introduced without risking aeroelastic instability" In [18], only simulations are executed, thus sensor placement and eigenmodes identification are not investigated.

On the contrary, in [5], Danowski et al. (2013) designed modal isolation and damping control system for aeroservoelastic adaptive suppression (MIDAAS), as an alternative to the use of notch filters. The modal description of the analyzed system is used to stabilize aeroelastic modes while avoiding adverse control system interactions. In MIDAAS, the mode suppression is carried out one mode at the time, by calculating the optimal output blending for each mode representation transforming a MIMO system into a MISO system. Then, a linear quadratic regulator is used to find the optimal blending of the input for the specific modal damping and the optimal feedback gain. Each modal damping loop is implemented in parallel with the others, by using the orthogonality property of the modal system description. Moreover, since MIDAAS is intended to suppress only aeroelastic modes, it can be implemented aside from rigid body motion SAS, without experiencing any control system adverse interactions. Then MIDAAS is made adaptive via continuous update of the control gains calculated using LQR. The state-space matrices utilized in LQR calculations are estimated using subspace identification method (SSID) developed by Miller and de Callofon. MIDAAS was validated on an F-18C dedicated implementation, showing good results in both modal damping and subsystem identification. To obtain the necessary measurements, multiple inertial sensors measuring rotational and linear velocities and linear accelerations were placed in nine different positions on the aircraft resulting in a total of 81 sensor output. This highlights the key role of having enough sensor to measure and describe structural eigenmodes.

In [30], Wang et al. (2019) design a gust load alleviation FCS using incremental nonlinear dynamic inversion (INDI) for a Cessna Citation aeroelastic model including torsional and bending motions of the wing. Structural modes shape functions and generalized coordinates are discretized using the Galerkin method. Unsteady aerodynamic is described through the calculation of lift, moment and drag sectional coefficients around the elastic axis of the wing, summing up contributions from airfoil motion, control surface deflections and atmospheric disturbances. Each of those has both circulatory and non-circulatory contribution. For the circulatory part, the Theodorsen function is utilized. Gust dynamics are modelled according to Dryden and von Karman spectra. Then, to estimate the required states, a linear Kalman filter is implemented to capture aerodynamic states, gust states, and rigid and flexible body motions. This choice is motivated by the assumption that the flight control system keeps the aircraft states around the equilibrium point, thus linear Kalman filter is regarded as sufficiently accurate. For the controller design, nonlinear equations for translational, rotational, bending and torsional dynamics are linearized around the equilibrium point, then the linear system is inverted to calculate the input required to stir the system towards a reference acceleration value. For both INDI design and Kalman state observer design, a reduced aeroelastic model comprehensive of 24 states is defined to reduce the computational power required for the state estimation and control tasks. Then the whole FCS is tested in simulation using a more extensive model, providing a more accurate description of aerodynamic and structural modes than the one available for FCS design. The designed controller is effective and it proves that reduced models can be used for aeroelastic eigenmotion control.

In the last example, in [13] Mohamed et al. (2020) define a longitudinal aircraft model including bending modes for wing and fuselage. The aeroelastic coupling between rigid body motion, aerodynamic states, such as angle of attack and pitch rate, and structural mode is defined according to Waszak and Schmidt model (Waszak and Schmidt, 1986 [32]). The state-space model is expressed in modal form to decouple dynamics. Then the states are grouped into relevant $z_r$ and negligible $z_d$ states. $z_d$ dynamic transient behaviour is neglected and reduced to the steady-state value of the transfer function describing the $z_d$ to elevator deflection relation. After some substitutions, relevant state dynamics are obtained as a function of inputs and of the reduced contribution of the neglected states. Thus the system only consists of relevant states dynamics. Then a performance criterion to be minimized for the full system is defined as in equation 3.2.

$$J = \frac{1}{2}\int_0^\infty \left(x^T Q\, x + \delta_e^T R\, \delta_e\right) dt \tag{3.2}$$

The same substitutions are carried out to exclude the neglected dynamics. The procedure is carried out multiple times. For each iteration one extra flexible dynamic, thus two extra flexible states, is included in the reduced model and the performances of the obtained controller assessed. Flexible states are estimated using a Luenberger observer[12] fit for the state space only considering $x_r$. The reduced model proved to be a good representation of the full plant when only two structural motions were considered. The two structural modes are the first torsional mode of the fuselage and the first bending mode of the wing. By substituting the system matrices in the cost function described in equation 3.2, a gain matrix to be multiplied by the state for optimal control input is obtained. The control law showed good performance when applied to the full flexible aircraft model and tested for a tracking task in simulation. "Optimal control law derived for the reduced order system can be used as a suboptimal control for a flexible aircraft represented by the full order system" Mohammed 2020 [13].

All the papers mentioned provides a different insights and approaches on different control goals, while all dealing with the non negligible flexible nature of modern aircraft.

As already said previously, most of the solution proposed in the literature and almost all the ones mentioned in this chapter have the underlying hypothesis that there is the possibility to measure as many structural eigenmotion as required from their task or goal. This is indeed a nice hypothesis to use during research, and it certainly stands when working only with simulation models, but it is find to not hold as soon as the testing is shifted to real life applications.

[2]For more information about Luenberger observer, please refer to Radke (2006) [19]

4

# Nonlinear dynamic inversion based control systems

Nonlinear dynamic inversion (NDI) based flight control systems are model-based control strategies for nonlinear dynamic systems. The plant model is algebraically manipulated to express the system inputs as a function of the states and states derivative. From this latter formulation, the input required to obtain a certain state is calculated and then used as commands for the actual plant input, for example as an aileron deflection command. By applying the dynamic inversion block before the aircraft model, input-output linearization is realized and it is possible to design a linear controller for the newly obtained system. Firstly, the theoretical background for NDI is laid out. Later, it is complemented with the description of the incremental nonlinear dynamic inversion control technique, which is derived from NDI and it requires less knowledge of the system. As it will be shown later, INDI control strategy has been widely studied and applied to different vehicles, as it is simpler in its implementation compared to NDI and more robust towards model inaccuracies and disturbances. Although INDI controllers have shown to be robust, their implementation remains confined only at the research level, since at the best knowledge of the author, no production aircraft is mounting nonlinear dynamic inversion based flight control system. Thus, NDI and INDI implementation examples are provided and finally a discussion to evaluate performances, strengths and drawbacks of NDI and INDI will conclude this chapter.

## 4.1. Theoretical description

NDI and INDI share most of their theoretical background and they only differ from one another in some final passages. Therefore, firstly the NDI controller derivation is laid out. Then, for the INDI controller, only the steps that differentiate it from the NDI formulation will be mentioned.

### 4.1.1. Nonlinear Dynamic Inversion - NDI

[1]

Given a nonlinear SISO system, which is affine in the input variable $u$.

$$\begin{aligned} \dot{\vec{x}} &= \vec{f}(\vec{x}) + \vec{g}(\vec{x})\,u \\ y &= h(\vec{x}) \end{aligned} \tag{4.1}$$

The relative degree $r$ of the system in equations 4.1 is defined in as the minimum number of time differentiation required to be operated on the output $y$ to obtain an explicit relation between input $u$ and output (Van Kampen, de Visser 2020 [29]). For partial and fully controllable system of degree $n$ then the relation $r \leq n$ holds. If $r < n$ then there are $n - r$ hidden or internal dynamics. Then, the following change of coordinates is defined

$$\begin{aligned} \phi_1(\vec{x}) &= h(\vec{x}) \\ \phi_2(\vec{x}) &= L_f\, h(\vec{x}) \\ &\vdots \\ \phi_r(\vec{x}) &= L_f^{r-1}\, h(\vec{x}) \end{aligned} \tag{4.2}$$

Where $L_f^m\, h(\vec{x})$ is the $m^{th}$ Lie derivative of $h(\vec{x})$, which is defined as in equations 4.3

[1] For a more in depth and complete derivation and explanation of nonlinear dynamic inversion (NDI) controller, please refer to Van Kampen and de Visser, 2020 [29]

$$
\begin{aligned}
L_f^0 h(\vec{x}) &= h(\vec{x}) \\
L_f^k h(\vec{x}) &= L_f \left[ L_f^{k-1} h(\vec{x}) \right] = \nabla^T \left[ L_f^{k-1} h(\vec{x}) \right] \vec{f}(\vec{x}) \\
L_g L_f h(\vec{x}) &= \nabla^T \left[ L_f h(\vec{x}) \right] \vec{g}(\vec{x})
\end{aligned}
\tag{4.3}
$$

It is always possible to add $n-r$ functions $\phi_i(\vec{x})$ such as $L_g \phi_i(\vec{x}) = 0 \; \forall \; r+1 \leqslant i \leqslant n$ to complete the coordinate transformation in 4.2 and have a system of the same degree of the initial one.

$$
\vec{z} = \vec{\Phi}(\vec{x}) = \begin{bmatrix} \phi_1(\vec{x}) \\ \vdots \\ \phi_r(\vec{x}) \\ \phi_{r+1}(\vec{x}) \\ \vdots \\ \phi_n(\vec{x}) \end{bmatrix}
\tag{4.4}
$$

When operating the time derivative to $\vec{z}$, the time derivative of the first $r-1$ coordinates are:

$$
\begin{aligned}
\dot{z}_i = \dot{\phi}_i(\vec{x}) = \frac{\partial \phi_i(\vec{x})}{\partial \vec{x}} \dot{\vec{x}} = \frac{\partial \phi_i(\vec{x})}{\partial \vec{x}} \left[ \vec{f}(\vec{x}) + \vec{g}(\vec{x}) u \right] = \\
\frac{\partial L_f^{i-1} h(\vec{x})}{\partial \vec{x}} \vec{f}(\vec{x}) = L_f^i h(\vec{x}) = \phi(\vec{x}) = z_{i+1}
\end{aligned}
\tag{4.5}
$$

The $r^{th}$ coordinate time derivative is

$$
\begin{aligned}
\dot{z}_r = \dot{\phi}_r(\vec{x}) = \frac{\partial \phi_r(\vec{x})}{\partial \vec{x}} \dot{\vec{x}} = \frac{\partial \phi_r(\vec{x})}{\partial \vec{x}} \left[ \vec{f}(\vec{x}) + \vec{g}(\vec{x}) u \right] = \\
\frac{\partial L_f^{r-1} h(\vec{x})}{\partial \vec{x}} \vec{f}(\vec{x}) + \frac{\partial L_f^{r-1} h(\vec{x})}{\partial \vec{x}} \vec{g}(\vec{x}) u = L_f^r h(\vec{x}) + L_g L_f^{r-1} h(\vec{x}) u
\end{aligned}
\tag{4.6}
$$

Finally, the last $n-r$ elements describing the internal dynamics are reported in equation 4.7, with $i \in [r+1, n]$.

$$
\dot{z}_i = L_f \phi_i(\vec{x}) + L_g \phi_i(\vec{x}) u = q_{i-r}(\vec{x})
\tag{4.7}
$$

As said before, in the above equation the Lie derivative of $q_{i-r}(\vec{x}) = 0$ along $\vec{g}(\vec{x})$ is equal to zero. By looking at equations 4.4 and 4.5, the canonical form of a SISO system can be recognized. In order to conclude the coordinate transformation, the dependency of equations 4.4 and 4.5 on $\vec{x}$ has to be substituted with $\vec{x} = \vec{\Phi}^{-1}(\vec{z})$, thus equation 4.6 becomes

$$
\begin{aligned}
\dot{z}_r = L_f^r h \left[ \vec{\Phi}^{-1}(\vec{z}) \right] + L_g L_f^{r-1} h \left[ \vec{\Phi}^{-1}(\vec{z}) \right] u = a(\vec{z}) + b(\vec{z}) u \\
a(\vec{z}) = L_f^r h \left[ \vec{\Phi}^{-1}(\vec{z}) \right] \qquad b(\vec{z}) = L_g L_f^{r-1} h \left[ \vec{\Phi}^{-1}(\vec{z}) \right]
\end{aligned}
\tag{4.8}
$$

For the internal dynamics coordinates the substitution is trivial and not useful for the purpose of control system design and will not be discussed further. Then, from the system formulation expressed in equation 4.8, the input required to obtain a certain $\dot{z}_r$ given the state vector $\vec{z}$ can be described as $u = b^{-1}(z_r)[\dot{z}_r - a(\vec{z})]$. Expressing $\dot{z}_r$ as the desired change of the system behaviour $v$, or virtual input, the final formulation of equation 4.8 is

$$
u = b^{-1}(z_r)[v - a(z)]
\tag{4.9}
$$

If we combine the equation 4.9 and equation 4.1 as in figure 4.1, input ($v$) output ($y$) linearization is obtained. The system behaves like a $r^{th}$ degree integrator and can be stabilized using linear control theory.

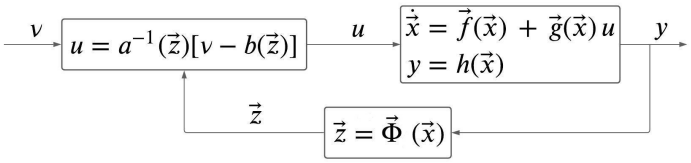


**Figure 4.1:** Input-output linearization system

It must be noticed that in order to obtain the desired output, the virtual input $v$ must be expressed as the $r^{th}$ desired time derivative of the output.

The final system has the same states and outputs as 4.1, but a different input in ($\vec{v}$) and the input-output relation is linearized. Thus the resulting system can be described as in equation 4.10 (Wang *et al.*2019, [31]).

$$\begin{aligned} \dot{\vec{\eta}} &= \vec{q}(\vec{\eta},\vec{\xi}) \\ \dot{\vec{\xi}} &= A_c\vec{\xi} + B_c\vec{v} \\ y &= C_c\vec{\xi} \end{aligned} \tag{4.10}$$

$A_c$, $B_c$ and $C_c$ are the canonical form representation of a chain of $r$ integrators. $\vec{\eta}$ has $n-r$ elements and $\vec{\xi}$ has $r$ elements and those describe namely the non-observable and the observable part of $\vec{z}$.

$$\vec{z} = \vec{\Phi} = \begin{bmatrix} \vec{\xi} \\ \vec{\eta} \end{bmatrix} \tag{4.11}$$

The extension of the just discussed method for MIMO systems requires some prior algebraic manipulations. Given a system as in equation 4.12

$$\begin{aligned} \dot{\vec{x}} &= \vec{f}(\vec{x}) + G(\vec{x})\,\vec{u} \\ \vec{y} &= \vec{h}(\vec{x}) \end{aligned} \tag{4.12}$$

Where $G(\vec{x})$, $\vec{u}$ and $\vec{h}(\vec{x})$ are expressed as in equation 4.13 with $\ell$ being the number of inputs and $m$ the number of output.

$$\begin{aligned} \vec{h}(\vec{x}) &= [h_1(\vec{x}), h_2(\vec{x}), ..., h_i(\vec{x}), ..., h_m(\vec{x})]^T \\ \vec{u} &= \left[u_1(\vec{x}), u_2(\vec{x}), ..., u_j(\vec{x}), ..., u_\ell(\vec{x})\right]^T \\ G(\vec{x}) &= \left[\vec{g}_1(\vec{x}), \vec{g}_2(\vec{x}), ..., \vec{g}_j(\vec{x}), ..., \vec{g}_\ell(\vec{x})\right] \end{aligned} \tag{4.13}$$

For each output variable, the respective relative degree can be defined as previously done for the SISO case. Thus, a relative degree vector is defined as $\vec{r} = [r_1, r_2, ..., r_i, ..., r_m]^T$ and a set of coordinates can be defined to express each inputs in the canonical form. Similar to the SISO case, we can define the $r_i^{th}$ Lie derivative for the $i^{th}$ output as components of the new coordinate system

$$\begin{aligned} \phi^i_{r_i}(\vec{x}) &= L_f^{r_i} h_i(\vec{x}) \\ \dot{\phi}^i_{r_i}(\vec{x}) &= L_f^{r_i} h_i(\vec{x}) + \sum_{j=1}^{m} L_{g_j} L_f^{r_i - 1} h_i(\vec{x}) u_j \end{aligned} \tag{4.14}$$

Collecting all $v^i = \dot{\phi}^i_{r_i}$ into a vector, the vector of the desired change in behaviour for each output is obtained as in equation 4.15

$$\vec{v}(\vec{x}) = \vec{\Psi}(\vec{x}) = \begin{bmatrix} \dot{\phi}^1_{r_i}(\vec{x}) \\ \dot{\phi}^2_{r_2}(\vec{x}) \\ \vdots \\ \dot{\phi}^m_{r_m}(\vec{x}) \end{bmatrix} = \begin{bmatrix} L_f^{r_i} h_1(\vec{x}) \\ L_f^2 h_2(\vec{x}) \\ \vdots \\ L_f^{r_m} h_m(\vec{x}) \end{bmatrix} + \begin{bmatrix} L_{g_1} L_f^{\mathrm{r}_1-1} h_1(\vec{x}) & L_{g_2} L_f^{\mathrm{r}_1-1} h_1(\vec{x}) & \cdots & L_{g_\ell} L_f^{\mathrm{r}-1} h_1(\vec{x}) \\ L_{g_1} L_f^{r_2-1} h_2(\vec{x}) & L_{g_2} L_f^{r_2-1} h_2(\vec{x}) & \cdots & L_{g_\ell} L_f^{r_2-1} h_2(\vec{x}) \\ \vdots & \vdots & \vdots & \vdots \\ L_{g_1} L_f^{r_m-1} h_m(\upsilon) & L_{g_2} L_f^{r_m-1} h_m(\vec{x}) & \cdots & L_{g_\ell} L_f^{r_m-1} h_m(\vec{x}) \end{bmatrix} \vec{u} \tag{4.15}$$

$$\vec{v}(\vec{x}) = \vec{a}(\vec{x}) + B(\vec{x})\,\vec{u} \tag{4.16}$$

Finally, $\vec{u}$ can be expressed as a function of $\vec{v}$ and the states, according to the structure in figure 4.1. The only difference lies on the linearization block, where now $\vec{u} = B^{-1}(\vec{x})[\vec{v}(\vec{x}) - \vec{a}(\vec{x})]$. As for the SISO case, the dependency of 4.16 on $(\vec{x})$ can be cancelled by applying the corresponding coordinate transformation to each element of $\vec{v}$.

### 4.1.2. Incremental Nonlinear Dynamic Inversion - INDI

The theoretical background of INDI is very similar to the NDI one, thus only the main differences will be highlighted[2].

INDI control strategy can be extended also for systems that are not affine in the input variable, but to better highlight similarities and differences, the analysed system will be considered the same as the one used before for the NDI theoretical discussion. Starting the discussion from equation 4.16, it is clear that the NDI linearization is based on the analytical and exact cancellation of the nonlinear terms $B(\vec{x})$ and $\vec{a}(\vec{x})$. When implementing NDI methods, this goal is almost impossible to achieve due to model simplifications and inaccuracies, computational errors and approximations and non-modelled disturbances. Thus, to simplify the input-output linearization method and to reduce the dependency of the method to the model used to design it, the first-order Taylor approximation of equation as reported in 4.17

$$\vec{\Psi} \approx \vec{\Psi}_0 + \left.\frac{\partial[\vec{a}(\vec{x}) + B(\vec{x})]}{\partial \vec{x}}\right|_{\substack{\vec{x}=\vec{x}_0 \\ \vec{u}=\vec{u}_0}} \Delta\vec{x} + \left.\frac{\partial[\vec{a}(\vec{x}) + B(\vec{x})]}{\partial \vec{u}}\right|_{\substack{\vec{x}=\vec{x}_0 \\ \vec{u}=\vec{u}_0}} \Delta\vec{u} + \mathcal{O}(\Delta\vec{x}^2, \Delta\vec{u}^2) \tag{4.17}$$

After due simplifications and terms grouping, equation 4.17 can be expressed as in equation 4.18. There, the terms related to the state vector derivative and increment is neglected and included in the calculation error (Wang *et al.*2019, [31]).

$$\begin{aligned} \vec{\Psi} &\approx \vec{\Psi}_0 + B(\vec{x}_0)\Delta\vec{u} + \vec{\delta}(\Delta\vec{x}^2, \Delta\vec{u}^2, \Delta t) \\ \vec{\delta}(\Delta\vec{x}^2, \Delta\vec{u}^2, \Delta t) &= \left.\frac{\partial[\vec{a}(\vec{x}) + B(\vec{x})]}{\partial \vec{x}}\right|_{\substack{\vec{x}=\vec{x}_0 \\ \vec{u}=\vec{u}_0}} \Delta\vec{x} + \mathcal{O}(\Delta\vec{x}^2, \Delta\vec{u}^2) \end{aligned} \tag{4.18}$$

Where $\vec{\Psi}_0$ is assumed to be measurable, $\Delta u$ is the increment to be added to the actuator command, $\vec{x}_0$ and $\vec{u}_0$ are the state values and actuator position values at the instant $t = t_0$, which are assumed to be measurable. $B(\vec{x}_0)$ is the control effectiveness matrix evaluated at the instant $t = t_0$ and $\vec{\delta}(\Delta\vec{x}^2, \Delta\vec{u}^2, \delta t)$ is the error committed by using the first order Taylor approximation. By making explicit the actuator command increment in equation 4.18 and defining $\vec{\Psi} = \vec{v}$

$$\Delta\vec{u} = B^{-1}(\vec{x}_0)[\vec{v} - \vec{\Psi}_0] \tag{4.19}$$

Which if substituted in equation 4.18 provides the input-output linearization for the linearized model. Similarly to the NDI case 4.10, also the INDI linearized plant model can be expressed as in equation 4.20 when applying the same coordinate change as described above in equations 4.2, 4.4 and 4.11

$$\begin{aligned} \dot{\vec{\eta}} &= \vec{q}(\vec{\eta}, \vec{\xi}) \\ \dot{\vec{\xi}} &= A_c\vec{\xi} + B_c[\vec{v} + \vec{\delta}(\vec{z}, \Delta t,)] \\ y &= C_c\vec{\xi} \end{aligned} \tag{4.20}$$

[2]For an exhaustive and complete dissertation please refer to Wang *et al.*(2019) [31].

In the actuator command increment calculation equation 4.19, $\vec{\delta}$ is neglected. It must be kept in mind that even if the nonlinear plant model is linearized in equation 4.17, the coefficients of the linearization, only $B(\vec{x}_0)$ in our case, can still show a nonlinear behaviour. Moreover, the total control input is obtained through the sum of the previous actuator state and the currently calculated increment

$$\vec{u} = \vec{u}_0 + \Delta\vec{u} = \vec{u}_0 + B^{-1}(\vec{x}_0)[\vec{\nu} - \vec{\Phi}_0] \tag{4.21}$$

It is worth to highlight one key difference between NDI and INDI. The latter relies less on model information than the former to calculate the control input (or actuator input). INDI only relies on information about control effectiveness $B(\vec{x}_0)$, while it is assumed that information on plant transient behaviour can be obtained by sensor measurements. On the contrary, NDI requires the knowledge of the plant observable dynamics, expressed by the term $\vec{a}(\vec{x})$. The downside of this difference is that INDI relies more on sensors measurements and it is mainly affected by the sensors sampling frequency, which is inversely proportional to the linearization error $\vec{\delta}$. For this reasons, INDI is often classified as sensor-based control strategy rather than a model base one.

## 4.2. Implementation examples

Although,both NDI and INDI has been widely studied, only the latter has shown more robustness, versatility and ease in implementation than the former. INDI control strategies have been developed, implemented, and successfully tested for a wide range of flying vehicles.

First, some NDI implementation examples will be provided and later different successful implementations will be briefly described and mentioned, starting from space application, moving to aircraft and finally to Micro Air Vehicles.

### 4.2.1. NDI based flight control system implemetation examples

In [17], Papageorgiou (2006) first design an NDI pitch rate controller using a longitudinal aeroelastic aircraft model. First, a so-called full aeroelastic model is developed to be used in the simulation as plant model. Later, it is reduced in the number of states and the reduced model is used to derive the linearization feedback via NDI technique. Finally, a PI controller is designed to stabilize the linearized plant and the sensor position is optimized to obtain the best measure of the pitch rate and to minimize the number of flexible modes to be used in the inversion controller. By doing so, only four flexible modes need to be considered in the reduced model. Then FCS performances are evaluated with respect to model uncertainties in both aerodynamic coefficients and flexible mode frequencies. The robustness of the developed control system is verified only for uncertainty on aerodynamic coefficients. A destabilizing perturbation is found to be related to incorrect modelling of frequencies of the flexible modes. The author suggests that to remove undesired contributions of flexible modes in the sensors measurements it is necessary the implementation of a notch filter for frequencies outside the bandwidth of rigid body motion frequencies.

In another NDI design example, James et al. (2016) [4] propose an attitude controller for a HALE aircraft, based on NDI input-output linearization nested in a PI control loop using direction cosine matrix. After the description of the elastic plant model, the NDI loop is developed by using translational and rotational speed output. Then the responses to a step in the attitudes angle reference are analysed for different conditions, which include combinations of neglection or consideration of actuator saturation and full or non-existent knowledge of the flexible states. The results show that, for this specific case and implementation, actuator saturation introduces relevant oscillations in the time response, and it increases the states settling time. It must be mentioned that the actuator dynamics are not modelled and it is assumed that the control surface deflection generates a pure torque on the aircraft. It also must be noticed that in real applications the actuator dynamics cannot be omitted during the NDI design process. Also, the neglection of flexible mode contribution increases the settling time, but in a minor way and it does not introduce any other effects.

As a final NDI based control system example, in [1], Alabsi et al. (2017) develop an NDI controller which uses frequency domain parameter estimation for control system parameters reconfiguration. In the specific case, a nonlinear dynamic inversion loop is designed for attitude rate control of a quadcopter. The actuator contribution to the plant dynamic or the control effectiveness is described through parameters that are

estimated using a linear regressor model. The model is then transposed in the frequency domain where both independent and dependant variable are Fourier transformed using recursive Fourier transform. Once the parameters are estimated, those can be used in the nonlinear dynamic inversion loop.

While not being fully able to deal with unmodelled dynamics and with rotational dynamic parameters identification, the algorithm showed excellent performances on recognizing reduced actuator effectiveness or recovering from wrongly initialized control effectiveness parameters. While for NDI both model parameters and control effectiveness are crucial for a successful implementation, this is not the case for INDI, where only the description of how inputs affect plant dynamic is relevant.

### 4.2.2. INDI based flight control system implemetation examples

Moving on to Incremental NDI, in [15], Mooij (2020) compares INDI and "Simple Adaptive control" performances, as in states deviation from the reference and control effort, with a benchmark PID FCS. The control task is to design an attitude controller for a flexible launch vehicle. The INDI design presents two nested linearization loops, the inner one to linearize the dynamic and the outer one to linearize the kinematics. Moreover, the plant model used to design the INDI controller only includes rigid-body motions. This choice was made to assess to what extent those flight control systems are affected by the flexible dynamics and to evaluate different types of measurement signal filtering. Mooij shows through simulations and consequent FCS performance analysis that INDI control strategy is the least affected by the unmodelled flexible dynamics. Analysis of the results shows that INDI controllers has better performances and that it is the least affected by the neglected flexible dynamics.

One of the first to introduce the INDI control technique was Smith (1998) [26], when he defined it as a "Simplified approach to nonlinear dynamic inversion". In his paper, Smith develops an attitude INDI controller and performs some test to assess performances and robustness. When analysing the sensor requirements, Smith claims that the sensors available at the time were accurate enough. However, since the plant equations used to develop INDI loop do not include flexible modes, care must be put in choosing the placement of the sensors, to avoid structural motion interference in the measurements. During tests, the designed controller showed to be robust in presence of non-modelled actuator rates and authority limits, sensor noise and variation on the model parameter, such as control effectiveness and inertia matrix.

As shown in 4.1.2, sensors sampling frequency plays an important role in the robustness of the INDI controller. Moreover, in real-life applications, it is unfeasible to remove the measurement delay due to signal digitalization. Thus, in [21], Sieberling et al. (2010) coupled an INDI controller with a predictive filter to compensate for sensors sampling delay. The predictive filter is a linear angular acceleration predictive filter, and its coefficients are calculated based on the INDI controlled closed-loop time response of the aircraft. In their analysis, an NDI controller an INDI controller and a predictive INDI (PINDI) are designed for attitude control of T-tail UAV. Then, the performances of those controllers are assessed via multiple simulations. In each simulation, the reference input is kept constant while parameters describing the aerodynamic model, centre of gravity, moment of inertia and noise in sensor measurements are varied. When comparing step response performances, PINDI facing time delay in sensor measurement achieve the same robustness and time response behaviour of the INDI implementation not subjected to any measurement delay.

Grondman et al. (2018) [11] designed, implemented and tested a manual attitude control based on INDI for a CS-25 certified aircraft. The model used to derive the linearization loop is a six degree of freedom rigid body model. The INDI loop does not include flexible states nor actuator or sensor dynamics. To compensate for the non-modelled actuator dynamic and saturation, pseudo control hedging technique is implemented in the outer loop, affecting the calculation of the virtual input of the INDI attitude rate controller given the pilot command. Both in simulation and real testing, angular acceleration measurements and control deflection measurements must be synchronized to avoid information mismatches in time. Moreover, for performance comparison, an NDI linearization loop is developed. Once again INDI proved to be more robust to model uncertainties, non-modelled effects of actuators, sensors, filters and wind disturbance with respect to NDI based solution. Moreover, the incremental version provides a better compromise between robustness, disturbance rejection and command response.

In [30], Wang et al. (2019) apply INDI based control strategy to regulate rigid body motions, alleviate the load due to gust presence and the wing root bending moment and suppress elastic modes. As usual, a first complete model, comprehensive of aerodynamic states, rigid and flexible body states and gust and turbulence states is developed for simulation purposes. Then the number of flexible states is reduced obtaining a so-called reduced model. This is necessary to lower the computational power required on board and to be able to measure all the required structural eigen motions. From the reduced model, rigid body and flexible accelerations are taken as output to be used for the INDI linearization loop design. Furthermore, aerodynamic gust and lag states are considered external disturbances and are not included in the reduced model. Differently from the derivation in 4.1.2 equation 4.17, the derivative with respect to the states variable is not neglected and it is considered as an additional term in the sum to be multiplied with the inverse of the control effectiveness matrix. Moreover, since the number of control variables is less than the number of states considered for the linearization loop, a weighted least-squares method is used to invert the non-squared control allocation matrix. The outer control loop providing the virtual input reference is designed to achieve desired forces and torques generation and to damp structural modes, depending on the nominal flight condition. Then a command-filtered actuator compensator is designed to deal with actuator saturation and bandwidth. Via simulations, the developed INDI based control system shown to achieve its task also in presence of model uncertainties, external disturbances, and sudden system faults. This proves once more the robustness of this control technique when applied to aircraft.

Finally, INDI control strategy has been successfully applied multiple times on Micro Air Vehicles (MAV). Smeur et al. (2016) [25] implement an attitude controller for an unmanned quadrotor using INDI loop linearization. Propeller dynamics are included in the plant model used to derive the flight control system considering the propellers rotational speed as the system input. Rotational accelerations are calculated via differentiation of attitude rate measurement signal, which must be filtered to avoid bad acceleration estimation. The chosen filter is a second-order one, with a cut-off frequency of 50 Hz. After the implementation of INDI feedback loop, the control effectiveness matrix depends only on two matrices, which can be estimated as adaptive parameters using a least mean squares technique. Multiple experiments are carried out to test the robustness of the control strategy and the performance of the parameter recognition algorithm. The controller developed by Smeur et al. provides consistent disturbance rejection of non-modelled aerodynamic which are extremely complex for MAV. Moreover, the inclusion of the propeller dynamic allows fast yaw control. The control effectiveness parameter estimation algorithm is proven to be fast enough to provide online adaptation of the control effectiveness matrix.

In another work from the same authors [24], Smeur et al. (2018) start from the results obtained in [25] to design and implement a cascade INDI control system for disturbance rejection. An outer INDI loop is designed to provide attitude and position control. Translational Newton equations of motion are considered. Linear accelerations are taken as plant output and attitude position and thrust are considered as system inputs. Then the aforementioned relation is inverted and linearized to provide the desired virtual inputs for the inner INDI linearization loop. Both inner and outer INDI loops are provided with a classical PID controller to obtain the desired steady-state and transient performances from the linearized system. The position controller is then tested under heavy wind condition both indoor, using a fan providing a lateral airflow of 10 $m/s$, and outdoor, by being exposed to Dutch wind. Once again, INDI control strategy has demonstrated to have high robustness and to be minimally affected by measurable external disturbances. INDI performances in position tracking were compared with a benchmark PID controller. While the PID controller was subject to a half a meter displacement due to 10 $m/s$ lateral wind disturbance, INDI controlled MAV experienced only 5 $cm$ displacement.

## 4.3. Nonlinear dynamic inversion control strategies discussion

After the description of different implementations of NDI and INDI based controller, in this final section, the characteristics, strength and drawbacks for both control strategy will be outlined.

Both NDI and INDI aim to obtain an input-output linearization of the plant via inversion of the nonlinear dynamic equations governing the system to be controlled. The use of nonlinear equations already accounts for very different operating conditions, which would have required the implementation of gain scheduling if linearized models for different flight conditions would have instead been considered. After having applied a favourable change of coordinates, the plant governing equations are inverted.

It must be guaranteed that the control effectiveness matrix is non-singular and invertible, or pseudo-invertible for non-squared matrices. Because of the equation inversion, the system must be a minimum phase one, otherwise, during the inversion process the plant zeros having a real positive part introduce unstable dynamics in the plant. The input-output linearization via plant inversion decouples the dynamics to be controlled and thus it makes easier and simpler the design of outer stabilization loops.

Both are model-based control strategies, but one relies on the system model more than the other. NDI is based on the complete analytical cancellation of the plant non-linearity. Thus, the required calculations include two main terms: one describing the transient behaviour of the system based on the current state and one which provides information about the input contribution to the system dynamic. The latter term is also supposed to be invertible. Instead, INDI is based on the inversion of the linearized plant nonlinear equations. Therefore, only the control effectiveness matrix is calculated and inverted while the transient behaviour calculation is substituted by appropriate sensor measurements. It follows that being the computational effort proportional to the complexity and size of the plant model, NDI results more computationally expensive than the INDI. In NDI implementation the number of parameters to be identified is larger than the one for INDI. Furthermore, as proved in Alabsi (2017) [1] and Smeur et al. (2016) [25], control effectiveness parameter identification is more robust than transition matrix parameters identification, especially when including complex aerodynamic. Moreover, NDI showed low robustness to the presence of unmodelled dynamics or disturbances, since those are not included in the plant representation and thus their contribution in sensor measurement will be misinterpreted. On the other side, INDI directly measures external disturbances and it compensates for those, as seen in Smeur (2018) [24].

Synchronization of sensor measurement signals and actuator position signal must be ensured, otherwise, calculations will be executed considering quantities belonging to different instants in time. Actuator nonlinearity and saturation must be kept in consideration, or better modelled into the control effectiveness matrix. Otherwise, NDI and INDI would command an actuator position which is not feasible. INDI error in control input increment is related to the quality of the sensors as it is inversely proportional to the sensors sampling time. If plant states cannot be directly measured, NDI requires to estimate those states via a full state observer. Moreover, if the plant model is partially or not known, system identification techniques must be deployed. On the other side, INDI only requires control effectiveness parameters to be calculated or estimated.

Once the nonlinear inversion loop is implemented, it can be integrated with other stabilization techniques to achieve the desired stability performances.

Overall, it can be said that INDI control system design strategy is easier to implement, and generates controllers which are more robust, more effective in rejecting disturbances than NDI-based ones.

5

# Preliminary analysis experiments and simulations

## Introduction, analysis description and simulations

In this additional chapter added to the literature study report, the analysis of the interaction between flight control systems and structural vibrations is carried out in both simulation and real experiments. First, a MATLAB®Simulink®model was developed to investigate the effects of Incremental Nonlinear Dynamic Inversion (INDI) controller design on different dynamic motions. Secondly, the flight control system - structural vibration interaction has been investigated in the specific case of the Parrot Bebop 2 stabilized using the INDI flight controller for stability augmentation purposes. In the following two sections, both the experiments will be described following the same logical structure. Firstly the description of the experimental setup and of the background theory will be provided, secondly, the goals of the experiment will be stated, then the test will be described and, finally, the results will be laid out and analyzed.

## 5.1. Bebep 2 vibrations generated by flight control system interaction with damper dynamic

As reported by thesis supervisor E.J.J. Smeur, during the flight control system design of the INDI based attitude controller for micro air vehicles (Smeur *et. al*, 2016 [23]), the test platform, namely a Parrot Bebop 2, was showing a sustained but not divergent oscillatory behaviour in the roll motion. Further analysis revealed that such phenomena were due to the presence of a spring-damper connection between the part of the frame where the sensors and the camera are attached to the part of the frame where the propellers are attached. Finally, the design choice was either to remove the spring-damper dynamic by fixing the two parts of the frame to one another or to lower the gains of the roll motion angular rate and position tracking. From now onward, with the camera frame, it will be pointed to the part of the Bebop 2 drone containing the frontal camera, the processing unit, battery and the sensor set (namely accelerometers and gyroscopes). With the motor frame, it will be indicated the lower part of the Bebop 2 where the propeller support attaches to the main body and where the bottom camera is placed. A series of ground vibration tests and flight tests have been carried out to analyze vibration phenomena.

### 5.1.1. Tests description and results

#### Ground vibration test

In order to retrieve the characteristics of the spring-damper system, the impulse response of the system was analyzed both in time and frequency domains. The impulse response was obtained by fixing the motor frame in a horizontal surface, where the measured roll and pitch angle would be null for an unperturbed condition. Then, to simulate the impulse input, an angular displacement was applied to the camera frame, followed by the release of the camera frame itself. The transient behaviour of a system to a non-zero initial condition is mathematically the same as the system impulse response. This test was repeated multiple times and the time domain data were cut to neglect non-relevant time series. The spring-damper system parameters, namely the natural frequency and the damping ratio, were calculated via frequency domain analysis and curve fitting of the time domain transient behaviour to the simulated impulse response of a second-order dynamic system. Thus, an analytical model is obtained, which has a natural frequency of 12.85 Hz and a damping ratio of 0.125. Its numerical transfer function is reported in 5.1

$$F(s) = \frac{6585}{s^2 + 22.62s + 6585} \tag{5.1}$$

The time response of the analytical model and of the Bebop spring-damper system are shown together in figure 5.1, while the PSD functions of the same systems are displayed in figure 5.2.

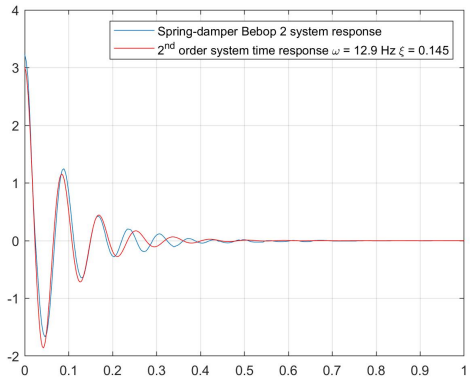


**Figure 5.1:** Time response to impulse input comparison

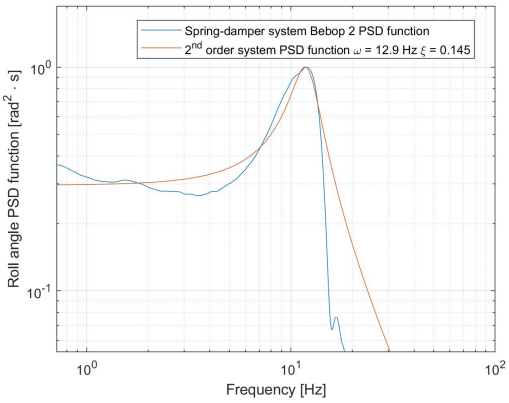


**Figure 5.2:** PSD function comparison

### Flight test

The flight test campaign had two main goals: first to reproduce the vibration motions experienced by E.J.J. Smeur during the design of the INDI flight control system. Secondly, to analyzed by what elements of the flight control system implementation this oscillatory behaviour is affected by and how. The INDI based flight control system is implemented in Paparazzi Autopilot, an open-source flight control system design framework. All the Paparazzi Autopilot FCS implementations are available in the Paparazzi Git repository. The flight control system consists of three nested loops: the inner one is the INDI loop for feedback linearization, the middle one is designed for angular rate tracking and the outer one ensures attitude angle tracking. It is worth mentioning that the inner INDI loop is not modifiable due to the fact that its structure and gain depend respectively on the type of dynamic system the controller is applied to and to the control effectiveness matrix describing the actuators contribution to the system dynamic. The middle and outer loops contain proportional controllers and can be modified. The flight control system contains sensor feedback signal filtering, to cancel the sensor measurement noise.

During preliminary tests, feedback signal filters being removed did not generate the vibration in the drone flight, while the increase of the middle and outer loop gains of the roll dynamic control loop did. Therefore, different flight tests with different gains on the roll angle and rate control loops were carried out to study the contribution of the two to the vibration phenomena. It is worth mentioning that while the gains for the angular position and rate control loop for the pitch and yaw dynamics had the values of 28 and 600 respectively, the same values for the roll control loops were 14 and 170.

The proportional gain for the attitude angle tracking loop is identified with the variable *ref_p* and the proportional gain for the angular rate tracking loop is *err_p* . Therefore, multiple flight tests were executed with different combinations of *ref_p* and *err_p* . For each flight test, measurements from the accelerometers and gyroscopes were recorded, together with the command signals. The goal of the test was to assess whether or not a specific *ref_p* -*err_p* combination would raise the oscillatory phenomena. Hence, each flight consisted of take-off, hovering and landing. In the case the vibration was not present, a high roll angle command would be provided manually to trigger the vibration. Once the data were recorded, relevant time series would be sampled from the complete flight data time history. This procedure was implemented to avoid having the contribution of transient behaviour due to manually provided commands. Once clean time series were obtained, a power spectral density (PSD) analysis was executed for each time series, and a smoothing filter was applied, which equation is provided in 5.1.1, where $\Psi(k)$ represent the PSD function.

$$\Psi(k)_{smoothed} = 0.25 \cdot \Psi(k-1) + 0.5 \cdot \Psi(k) + 0.25 \cdot \Psi(k+1) \tag{5.2}$$

When multiple PSD functions for the same *ref_p* - *err_p* gain combination were obtained one single PSD function was calculated by averaging all the PSD functions available. The sampling rate is 170 Hz and the sampling time is not uniform throughout the different flight tests. Therefore, the Nyquist frequency for this test run would be 85 Hz and the frequency resolution would be variable since it depends on the sampling time. As the final data processing step, the frequency series vector where linearly interpolated to obtain uniform vectors with a frequency step of $\Delta f = 0.1$ Hz.

In the table below 5.1 is reported which *ref_p* - *err_p* gain combination leads to oscillatory behaviour. To show the effects of gain variation on the system response, the PSD functions calculated are displayed in the following fashion. Firstly, in figure 5.3 *ref_p* gain is constant while *err_p* gain varies from 50 to 600. Secondly, in figure 5.4 *err_p* gain is kept constant while *ref_p* is modified giving the values mentioned in table 5.1.

| \ | *ref_p* | 7 | 14 | 21 | 28 |
|---|---|---|---|---|---|
| *err_p* | \ | | | | |
| 50 | | - | - | x | x |
| 170 | | - | - | x | x |
| 400 | | - | - | x | x |
| 600 | | - | - | x | x |

**Table 5.1:** Presence of oscillatory behaviour depending on the *err_p* - *ref_p* gain values

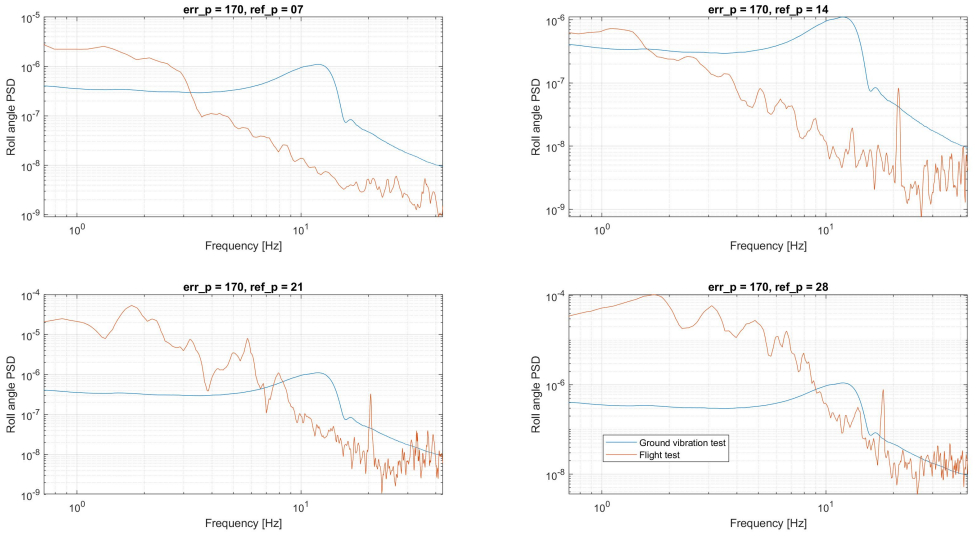


**Figure 5.3:** PSD function for constant *ref_p* and variable *err_p* compared with the one obtained from GVT

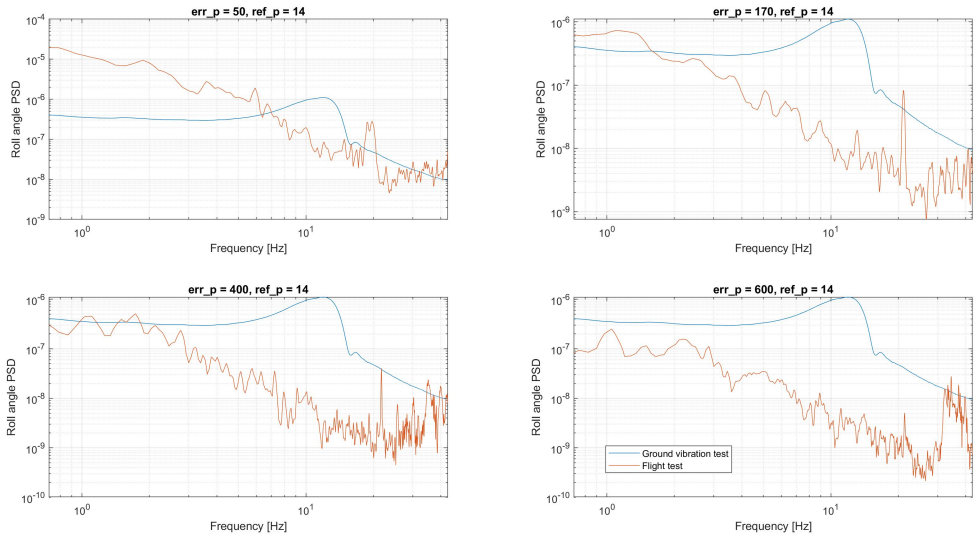


**Figure 5.4:** PSD function for constant *err_p* and variable *ref_p* compared with the one obtained from GVT

### 5.1.2. Flight test result analysis and discussion

As already mentioned in the flight test description subsection 5.1.2 and as clearly understandable from table 5.1, *err_p* gain does not influence neither trigger the Bebop 2 oscillatory behaviour. On the contrary, increasing the value of the outer loop gain decrease the overall magnitude of the PSD function, and therefore also the power contained associated with structural eigenmotion. As it can be noticed in the graphs in both figure 5.3 and 5.4, around the 19.33 Hz frequency it is always present a spike, which corresponds to the structural oscillatory behaviour frequency contribution. It is clear from the graphs in figure 5.4 that the power contained in the structural eigenmotion spike is never comparable with the peak of the ground vibration test PSD function and it is never above the steady-state value of the GVT PSD function.

On the contrary, an increase in *ref_p* value triggers and excites the structural vibration motion. For *ref_p* equal to 7 or 14, the spike related to oscillatory behaviour is one decade lower than the peak of the spring-damper system on the Bebop 2. For higher values of *ref_p* the contribution of the structural vibration starts to be comparable to the ground vibration test response and therefore it starts to be experienced during flights. It can be deduced that the outer loop, namely the attitude tracking loop, high gain can generates the interaction between the flight control system and the structural dynamic of the drone. This was to be expected since the flight control system utilized during the flight tests has been designed assuming the Bebop to be a single rigid body without structural eigenmotion. Thus, the INDI gain is obtained by the inversion of the control effectiveness matrix which is itself the inverse of the inertia momentum matrix of the rigid body. As it will be shown later, this lead to a higher INDI gain than the one obtained when considering the structural dynamic of the drone. Therefore, in the test case, the INDI loop gain is non-optimally designed and therefore the motion control is affected via the interaction between the attitude angle tracking control loop and the structural vibration.

## 5.2. MATLAB®Simulink®model

### 5.2.1. INDI controller derivation

The MATLAB® Simulink® simulation consist in the implementation of two different controllers for angular reference tracking. The dynamic system to which these two controllers are applied is one axis, two degrees of freedom system, describing the roll dynamic of the Parrot Bebop 2 drone. The two controllers are two different INDI implementations for this task: one considering the system as one rigid body and the other one considering the system as two rigid bodies connected via a spring-damper system. Both controller derivations start from the simplification of the Euler rotational equation of motion for a rigid body 5.3, for one rotation axis dynamic.

$$I\ddot{\vec{\theta}} + \dot{\vec{\theta}} \times I\dot{\vec{\theta}} = \sum_i \vec{M}_i \tag{5.3}$$

Moreover, the vector symbol can be dropped $\theta = \vec{\theta}$, since only one rotation axis is considered. In both cases, aerodynamic forces and gravity contribution to the rotational motion are not considered. Therefore for the first INDI implementation is based on the equation of the rotation motion of a single rigid body around one axis 5.4 of inertial momentum $I_{xx}$ and subjected to a torque acting as control input $\tau$. Due to the single dimension of the problem, the cross product term can be neglected. Angular acceleration, rate and position are assumed to be measurable.

$$I_{xx}\ddot{\theta} = \tau \tag{5.4}$$

By taking the first order expansion of equation 5.4, substituting the zero order contribution with the measured angular acceleration $\ddot{\theta}_m = \ddot{\theta}^{(0)}$ and the angular acceleration on the left hand side with the desired virtual input $\nu = \ddot{\theta}$ and solving for $\Delta\tau$, the control input increment is obtained (Wang *et al.*2019 [31]), as in equation 5.5.

$$\begin{aligned} \ddot{\theta} &= \frac{\tau}{I_{xx}} \\ \ddot{\theta} &\approx \ddot{\theta}^{(0)} + \frac{\Delta\tau}{I_{xx}} \\ \nu &= \ddot{\theta}_m + \frac{\Delta\tau}{I_{xx}} \\ I_{xx} &\cdot (\nu - \ddot{\theta}_m) = \Delta\tau \end{aligned} \tag{5.5}$$

For the second INDI implementation, the Bebop 2 model is considered to be constituted by two rigid bodies hinged in the same point and connected via a spring-damper system. Two rotational equations of motions are needed to describe the system, one for each rigid body. The Bebop2 frame is divided into two frames, the first one is the motor frame and it is the point of attachment of the propellers. Therefore, the control torque $\tau$ is applied to this frame. The second frame, or camera frame, is the one containing the camera, the processing unit and the measurement equipment such as gyroscopes and accelerometers. Thus, only the angular position, rate and acceleration of the camera frame are measurable and can be controlled. The angular position of the motor frame and camera frame are respectively $\theta_{motor} = \alpha$ and $\theta_{camera} = \beta$. The inertial momentum of the two frames are $I_{motor} = I_m$ and $I_{camera} = I_c$. The equations of motions considered are displayed in 5.6

$$\begin{aligned} \ddot{\alpha} &= \frac{1}{I_m}\left[(\dot{\beta} - \dot{\alpha})C + (\beta - \alpha)K + \tau\right] \\ \ddot{\beta} &= \frac{1}{I_c}\left[(\dot{\alpha} - \dot{\beta})C + (\alpha - \beta)K\right] \end{aligned} \tag{5.6}$$

Where $K$ and $C$ are respectively the elastic coefficients and the damping coefficient of the spring-damper system. It is worth mentioning that in the second equation in 5.6, there is no explicit relation between the input and the considered output, which in this case is the acceleration of the camera frame $\ddot{\beta}$. To obtain an explicit relation between the control input $\tau$ and the measurable output $\ddot{\beta}$ to design the INDI controller, a change of coordinate can be executed (Wang *et. al*) [31]. Due to the reduced size of the system, it is also possible to operate the time derivative of the output as many times as necessary until the explicit input-output relation is obtained [29]. By deriving the second equation in 5.6 in time and substituting the first for $\ddot{\alpha}$, the required relation is obtained.

$$\begin{aligned} \frac{d\ddot{\beta}}{dt} &= \frac{d}{dt}\left\{\frac{1}{I_c}\left[(\dot{\alpha} - \dot{\beta})C + (\alpha - \beta)K\right]\right\} = \frac{1}{I_c}\left[(\ddot{\alpha} - \ddot{\beta})C + (\dot{\alpha} - \dot{\beta})K\right] \\ \frac{d\ddot{\beta}}{dt} &= \frac{1}{I_c}\left\{\left[\frac{1}{I_m}\left[(\dot{\beta} - \dot{\alpha})C + (\beta - \alpha)K + \tau\right] - \frac{1}{I_c}\left[(\dot{\alpha} - \dot{\beta})C + (\alpha - \beta)K\right]\right]C + (\dot{\alpha} - \dot{\beta})K\right\} \\ \frac{d\ddot{\beta}}{dt} &= \frac{1}{I_c}\left\{\left[\frac{1}{I_m}\left[(\dot{\beta} - \dot{\alpha})C + (\beta - \alpha)K\right] - \frac{1}{I_c}\left[(\dot{\alpha} - \dot{\beta})C + (\alpha - \beta)K\right]\right]C + (\dot{\alpha} - \dot{\beta})K\right\} + \frac{C}{I_m I_c}\tau \\ \frac{d\ddot{\beta}}{dt} &= \Gamma(\alpha, \dot{\alpha}, \beta, \dot{\beta}) + \frac{C}{I_m I_c}\tau \end{aligned} \tag{5.7}$$

Now it is possible to obtain the INDI control input increment executing the same procedure as in equation 5.5, by carrying out the first order Taylor expansion for $d(\ddot{\beta})/dt$ from equation 5.7. For the current analysis, it results in equation 5.8

$$\dddot{\beta} \approx \dddot{\beta}^{(0)} + \frac{\partial \Gamma(\vec{x})}{\partial \vec{x}^T}\Delta\vec{x} + \frac{C}{I_m I_c}\Delta\tau \tag{5.8}$$

Where $\vec{x} = [\alpha, \dot{\alpha}, \beta, \dot{\beta}]^T$ is a vector containing the states of the two body system. Differently from equation 5.5, in 5.8 there is a contribution of $\Gamma(\vec{x})$, which can be neglected (Wang *et. al*) [31]. Solving equation 5.8 for $\Delta\tau$, substituting the virtual control input to the angular acceleration time derivative $\nu = \dddot{\beta}$ and the zero order $\dddot{\beta}$ approximation with the quantity measured on board $\dddot{\beta}_m = \dddot{\beta}^{(0)}$, the INDI control input increment is obtained, as shown in equation 5.9.

$$\begin{aligned} \nu &= \dddot{\beta}_m + \frac{C}{I_m I_c}\Delta\tau \\ \Delta\tau &= \frac{C}{I_m I_c} C\left[\nu - \dddot{\beta}_m\right] \end{aligned} \tag{5.9}$$

The quantity $\Delta\tau$ is then added to the last recorded value of the actuator state in order to provide the actuator command for the next time step. This structure is equivalent to provide positive feedback of the actuator state and it is indeed clear when displaying how the actuator command is calculated, as shown in figure 5.5. The positive feedback of the actuator state has relevant consequences for what concerns both simulation and real-life implementation, which will be discussed later in this chapter when describing the outcomes of the simulations. To better replicate the real behaviour of the drone, it was decided to separate the actuator dynamic simulating the actual actuator transient behaviour from the one usually artificially defined to implement signal synchronization.

For both the INDI controllers, after having designed and implemented the feedback linearization loops, extra external loops have been designed and implemented to pursue an angular position tracking task. Both outer control loops, namely angular rate tracking loop and angular position tracking loop, for both INDI implementations, have been designed to not provide overshoot in time-domain step response. Moreover, to both feedback linearization INDI loops synchronization has been ensured via applying a low pass filter to the torque command feedback signal, as shown in figure 5.5, since information synchronization between actuator position signal and angular acceleration signal must be provided (Grondman *et. al*, 2018 [11]).

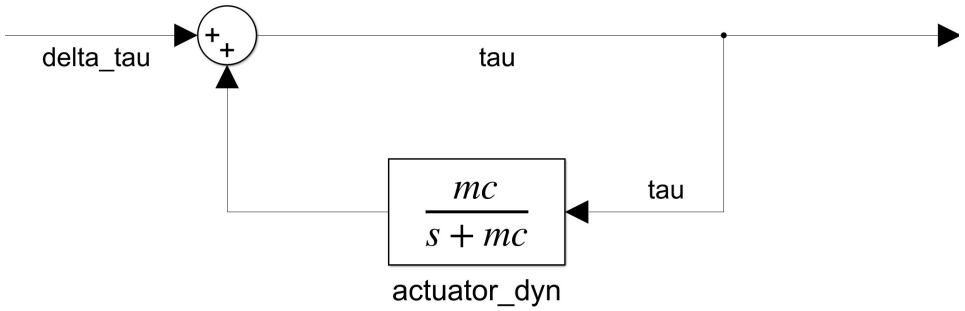


**Figure 5.5:** Simulink®model detail - Actuator signal synchronization loop

### 5.2.2. Simulink®dynamic model description

The Simulink®model replicates the one axis rotational dynamic of two rigid bodies hinged at the same point and connected via a rotational spring and a rotational damper. In one of the bodies, namely the motor frame, a control input, a torque, is applied, meanwhile, only the second body, namely the camera frame, angular position, velocity and acceleration are observable. Moreover, a first-order lag dynamic is introduced to simulate the transient behaviour of the actuator. Finally, a saturation block is added to keep the simulation closer to the real-life case.

The Simulink®model is designed to simulate the roll dynamic of a Parrot Bebop 2 drone. Therefore the natural frequency and the adimensional damping of the system composed by spring, damper and the camera frame have been estimated via ground test vibration and impulse response curve fitting, as mentioned in the previous section 5.1. Then, the rotational spring and damper coefficient have been estimated by assuming that the camera frame has an inertia momentum equal to 45% of the total inertia momentum of the drone. The total drone inertia momentum is a known parameter from previous researches carried out at the MavLab. In the following table 5.2, all the Simulink®model parameters are defined and in figure 5.6 the structure of the model is shown.

| Parameter | Symbol | Value | Unit |
|---|---|---|---|
| Total rotational inertia | $I_{xx}$ | $1.926 \cdot 10^{-3}$ | $Kg \cdot m^2$ |
| Motor frame rotational inertia | $I_m$ | $1.045 \cdot 10^{-2}$ | $Kg \cdot m^2$ |
| Camera frame rotational inertia | $I_c$ | $8.550 \cdot 10^{-3}$ | $Kg \cdot m^2$ |
| Elastic coefficient | $K$ | 6.812 | $N \cdot m \cdot rad^{-1}$ |
| Damping coefficient | $C$ | $2.109 \cdot 10^{-2}$ | $N \cdot m \cdot s$ |
| Propeller dynamic natural frequency | $mc$ | 50.0 | $rad \cdot s^{-1}$ |
| Propeller saturation value | — | $\pm\ 2.388 \cdot 10^{-2}$ | $N \cdot m$ |

**Table 5.2:** Dynamic model parameters.

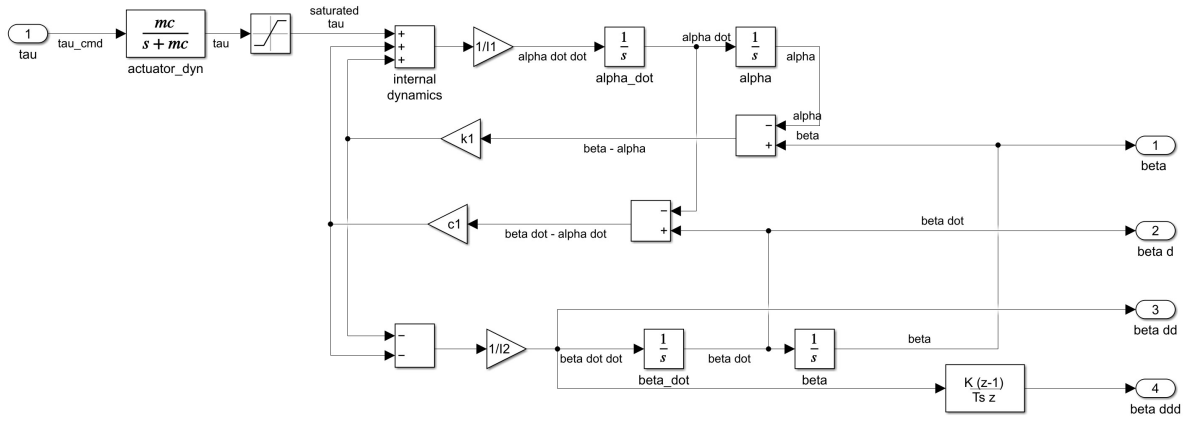


**Figure 5.6:** Two bodies Simulink®model for Bebop 2 roll dynamic

As already mentioned at the beginning of this subsection, in the above figure 5.6 a saturation block is added to simulate saturation of the propeller rotational speed on the Bebop 2. The saturation value is defined for the control torque to provide a maximum angular acceleration of $4\pi \mathrm{rad\,s^{-2}} = 2\,\mathrm{Hz\,s^{-1}}$. The third-order time derivative of the camera frame angle is calculated by applying a discrete-time derivative to the continuous-time signal $\ddot{\beta}$. The simulation time step is set to 0.001 s and the chosen solver is *ode5*.

In order to verify the performance of the one body model based INDI controller and to properly design the control attitude rate and angle tracking controllers, also the one rigid body model of the Bebop roll dynamic has been implemented. It is described by the equation of motion in 5.4 and it takes into account the actuator saturation. The only input to the system is the control torque, which is provided again considering the actuator dynamic as first-order lag system, with the same cutoff frequency of the two bodies model $mc$. The system Simulink®diagram is displayed in figure 5.7 The simulation solver parameters are the same mentioned before: the time step is 0.001 s and the chosen solver is *ode5*.

### 5.2.3. Final control system implementation

Both one body model based and two bodies model based have been designed to fulfil an attitude angle tracking task, to be stable for both impulse input, or for non zero attitude angle initial conditions, and step input and to not show any overshoot in the impulse and the step response. With the exception of the INDI linearization loop gains, all the controller gains values were found via manual tuning of each control loop, following an inside out loop tuning order.

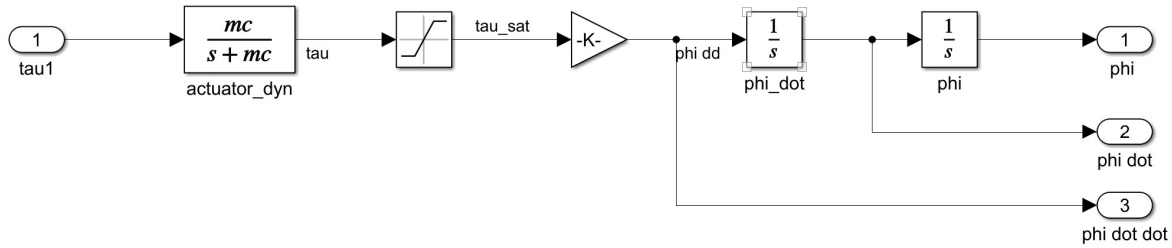


**Figure 5.7:** One body Simulink®for Bebop 2 roll dynamic

| | Proportional | Integral | Derivative |
|---|---|---|---|
| INDI loop | $1.926 \cdot 10^{-3}$ | 0 | 0 |
| attitude rate tracking | 13 | 0 | 0 |
| attitude angle tracking | 2.1 | 0 | 0 |

**Table 5.3:** List of gains for one body model based control system

### One rigid body based INDI control system

The one body model based INDI control system consists of three nested loops as it does the attitude control system described in 5.1.1. The complete structure of the control system is shown in figure 5.8, where different control loops are marked with different colours. Each of the three loops has a PID block but only the proportional gain of each block is non-zero. The inner loop, marked in green, is the INDI linearization loop, which gains calculation is described in 5.7 and correspond to the total roll inertia momentum $Ixx$ mentioned in table 5.2. The middle loop is ensuring the attitude rate tracking and is marked in red and the outer and last loop is designed for attitude angle tracking and is marked in blue. The gains for each loop are reported in table 5.3.

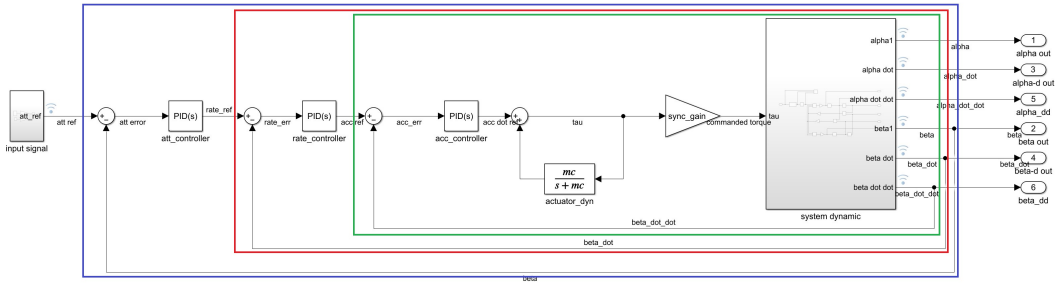


**Figure 5.8:** One body model based INDI controller

### Two rigid body based INDI control system

This control system contains one extra loop with respect to the previous one since the INDI linearization loop now takes as input the derivative of the angular acceleration. In figure 5.9, the four nested loops are displayed and marked with different colours.

The attitude angle tracking loop is marked in blue, the attitude rate control loop, the attitude acceleration control loop and the INDI linearization loop are marked in red, green and orange respectively. Each loop has a PID block which gains are reported in the table below 5.4.

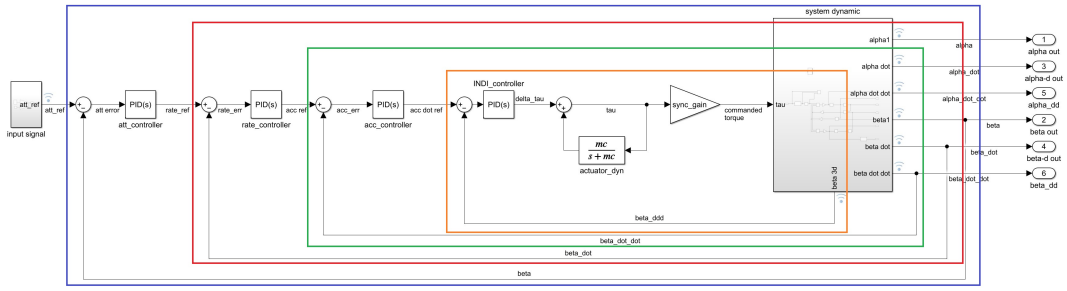


**Figure 5.9:** Two bodies model based INDI controller

| | Proportional | Integral | Derivative |
|---|---|---|---|
| INDI loop | $3.832 \cdot 10^{-05}$ | 0 | 0 |
| attitude acceleration tracking | 25 | 0 | 6 |
| attitude rate tracking | 22 | 0 | 0 |
| attitude angle tracking | 2.5 | 0 | 0 |

**Table 5.4:** List of gains for two body model based control system

### 5.2.4. Simulation description and outcomes

Both the designed and previously described control systems have been excited with two different inputs as attitude angle reference signals. The first input is a step signal of the amplitude of 90 ° with the step in the signal occurring 1 s after the starting instant of the simulation. The second one is an impulse spike provided at the initial instant of the simulation as a non-zero initial condition for the attitude angles. The one body model-based controller has been applied also to the one body model described in 5.2.2. Therefore, the combination of system model and controllers are the following:

| | Control system | Simulink®model |
|---|---|---|
| 1 | One body model based | One body |
| 2 | One body model based | Two bodies |
| 3 | Two body model based | Two bodies |

The systems time responses from all three combinations will be displayed and spectral analysis will be executed on each time history signal. Consequently, due considerations and discussion will be carried out concerning key points of the frequency domain analysis. All the figures mentioned in the following subsection, are reported in appendix A 6.

#### One rigid body based INDI control system

Both systems response to both input signals are displayed in figures 7, 1, 9, 3, 11 and 5 where $\phi$ and its derivative represent the attitude quantities of the one rigid body Simulink®model, and $\alpha$, its derivative, $\beta$ and its derivative describe the roll angle related quantities of respectively the motor frame and the camera frame of the two bodies Simulink®model.

As can be noticed in the time domain response graphs zooms in figures 8, 2, 10, 4, 12 and 6, the two bodies system has an oscillatory component, which increase in magnitude with the increase of the time derivative order. This characteristic of the system response is better highlighted in the graphs showing the power spectral density function of the output signals. In the aforementioned graphs, reported in figures 27, 24, 28, 25, 29 and 26, show a peak in around the 19.33 Hz frequency which is generated by the interaction between the INDI controller and the structural dynamic. This is supported by the evidence that the one body Simulink®model to which is applied the analysed controller is not showing this feature, as displayed in the time and frequency domain figures mentioned above. Moreover, similar results have been obtained during the flight test described in section 5.1, where the flight control system interaction

with the structural eigenmotion of the Parrot Bebop 2 generates a frequency contribution component around 19.33 Hz.

The effects of different gain combinations in the different rate and attitude control loops do not affect the interaction between the controller itself and the structural eigenmotion, since the interaction is already excited by the INDI loop itself. The attitude rate control loop contains only proportional gains because the addition of the integral gain generates a highly damped low-frequency oscillation which increases the settling time of the angular position time response to a step input. Also, the derivative gain in the rate control loop is set to zero because it does not bring any beneficial contribution to the system performance. Similarly, in the attitude PID controllers both the integral and the derivative gains are set to zero. The presence of the integral gain introduces overshoot in the time domain response of the system, while the derivative gain introduces a highly damped low-frequency oscillation which increases the step response settling time.

### One rigid body based INDI control system combined with signal filtering

In order to not excite the structural modes at the frequency of 19.33 Hz as the above-described flight control system does, a notch filter has been implemented in the simulation, using the relative MATLAB®Simulink®block. The transfer function of the filter is reported in equation 5.10 and its Bode plot is shown in figure 5.10.

$$F(s) = \frac{s^2 + 2g\xi\omega_c + \omega_c^2}{s^2 + 2\xi\omega_c + \omega_c^2} \tag{5.10}$$

Where $\omega_c$ = 19.33 Hz is the working frequency of the filter, $g$ = 0.001 is the filter signal attenuation at the working frequency and $\xi$ = 0.25 is a damping parameter that determines the width of the filter negative spike. The Bode plot in figure 5.10 represent the filter described in equation 5.10 with the above mentioned numerical parameters.

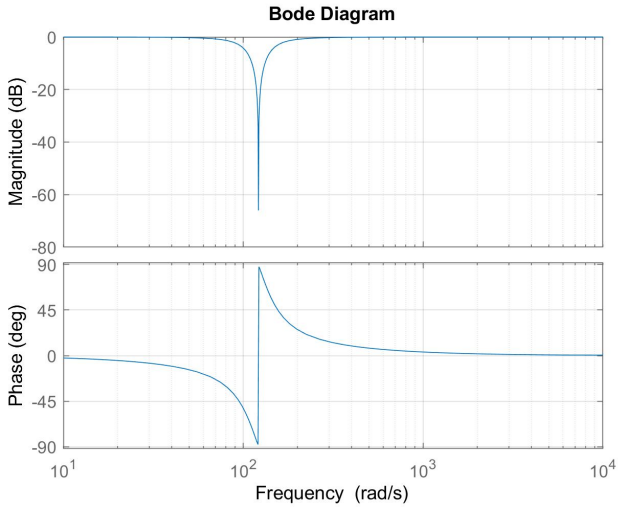


**Figure 5.10:** Notch filter Bode plot

When the filter is place anywhere in the INDI inner control loop (marked in green in figure 5.8), the system response to an impulse first peak in the PSD frequency content get shifted to the frequency of 15.4 Hz, as shown in the PSD function plots for accelerations and rates in figures 5.11 and 5.12. Regardless of the notch filter placement in the INDI loop, it could be placed either before or after both the synchronization loop or the INDI proportional controller, the system response would be the same. When the notch filter is applied to the outer loops signal or to other feedback signals, attitude rate or attitude position, it shows no effects on the system response.

In the above graphs, the x-axis represents the frequency in $Hz$ while the y-axis represents the []/$Hz$, where [] is the measuring unit of the analysed quantity.

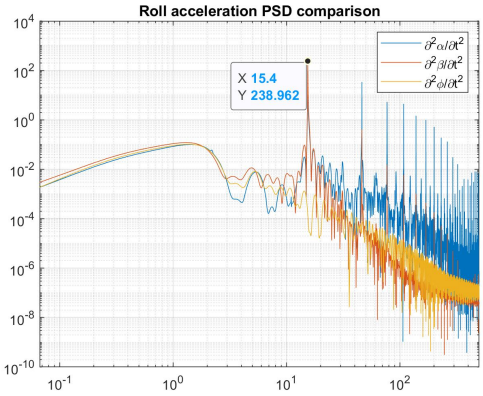


**Figure 5.11:** Angular acceleration PSD function for impulse response - first filter configuration

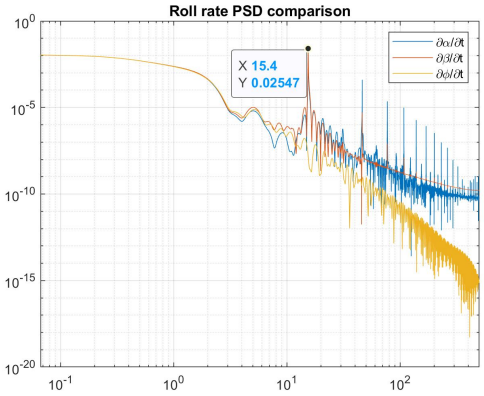


**Figure 5.12:** Angular rate PSD function for impulse response - first filter configuration

Then, to suppress the new peak, another notch filer, with the same structure as the first one but with a working frequency of 15.4 Hz is placed after the rate controller. The placement of the second filter appeared useless since the newly found frequency contribution is present in both the acceleration feedback and in the acceleration reference signal (which is calculated in the rate controller). Therefore, another notch filter with a $\omega_c = 15.4$ Hz was placed in the acceleration feedback signal. The PSD analysis of the system with the three notch filters response to an impulse is shown in figures 5.13 and 5.14. For sake of brevity, only the attitude rates and acceleration graphs are shown.

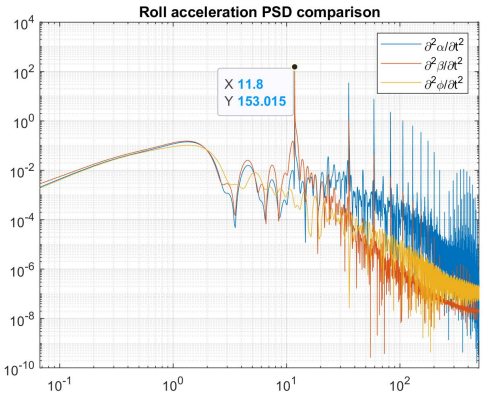


**Figure 5.13:** Angular acceleration PSD function for impulse response - second filter configuration

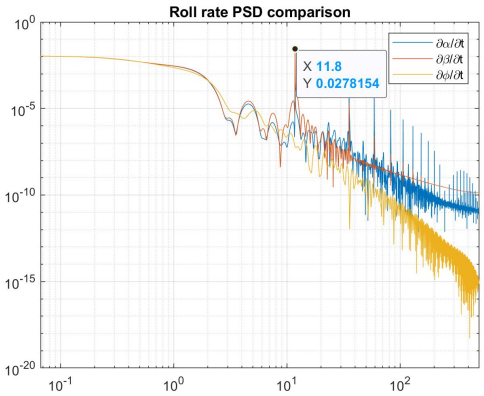


**Figure 5.14:** Angular rate PSD function for impulse response - second filter configuration

In the above graphs, the x-axis represents the frequency in $Hz$ while the y-axis represents the []/$Hz$, where [] is the measuring unit of the analysed quantity.

From the graphs can be deduced the peak has just been moved once more to a lower frequency. Therefore, the use of notch filters for frequency content cancellation has not been successful in this case. One of the possible causes can be that no open-loop analysis has been carried to assess which are the open loop major frequency domain contributors.

### Two rigid body based INDI control system

System responses to both impulse and step input show no visible oscillations in the roll angle time series data of both bodies, neither do they in the frequency domain analysis. The PSD function of both $\alpha$ and $\beta$ impulse response, displayed in figure 35, resemble a second order low pass filter and no spikes are present in those functions. For what concerns $\dot{\alpha}$ and $\dot{\beta}$, $\ddot{\alpha}$ and $\ddot{\beta}$ time responses to both input, which

are shown in figures 20, 15, 17 and 17, even if some high frequency oscillations are present, those are not relevant in magnitude for the drone dynamic. As can be seen in the power spectral density function of the aforementioned variables in figures 34, 31, 35 and 32 never exceed the steady state PSD function value. Therefore, the designed controller avoid interacting with the structural dynamics of the drone, allowing higher gains in outer loops and faster settling time to the provided reference. From the PSD function graphs it can be noticed that the two bodies model based INDI controller does not trigger the structural vibration in the two bodies Simulink®model, in contrast with the one body model based which does.

It is interesting to notice in figures 18 and 14 how the actuator reach its saturation point almost immediately and the angular accelerations of both bodies settle to the value of $\pm 2\,\mathrm{Hz\,s^{-1}}$.

The PID controllers for the attitude and rate control only consist in the proportional component because adding integral gains at the configuration described in table 5.4, add overshoot in the time domain response. Moreover, adding the derivative component of the PID triggers the interaction between the structural dynamic and the control system. On the contrary, the controller for the angular acceleration control loop has the derivative contribution of the PID. Indeed would have been possible to design another controller containing only proportional gains, but its performances in terms of transient response quickness would be worse than the one from the implemented controller. In the specific case and for the roll angle tracking task, the settling time of the controller containing only proportional gains would be three times higher than the controller containing a derivative gain on the angular acceleration control loop.

#### Additional remarks

During the design of the two INDI based controllers, some non-expected behaviours have been encountered which investigation led to this final remark paragraph.

During the design of the inner INDI loop for the one body model based controller, an initial stability issue was present and temporary solved by applying a gain $\mu = 0.125$ to the actuator command signal provided by the controller. Further investigations showed that the synchronization loop indeed acts as an integrator for the $\Delta u$ signal while keeping track of the actual actuator position. However, at the same time, it provides an additional loop gain related to the actuator characteristics. Given an actuator whose dynamic can be approximated by a first-order lag system with a cut-off frequency of $\omega_c = \bar{\omega}$. The related transfer function would be $F(s) = \bar{\omega}/(s+\bar{\omega})$. As reported in figure 5.5, the transfer function of the positive feedback would be $L(s) = 1/(1-F(s))$. Therefore, the value of $L(s)$ would be as reported in equation 5.11.

$$L(s) = \frac{1}{1-F(s)} = \frac{1}{1-\frac{\bar{\omega}}{s+\bar{\omega}}} = \frac{s+\bar{\omega}}{s\bar{\omega}} \tag{5.11}$$

This transfer function is a pure lag - lead filter with a $|L(s)| \geqslant 1$ gain for every frequency contribution to the input signal. As matter of fact, the gain is higher for frequencies closer to zero and smaller and close to 1 for frequencies $\geqslant \bar{\omega}$. This increase the loop gain, decreasing the phase margin at low frequency.

Another key remark rose during the integration of the saturation block on the Simulink®model design. While divergent oscillations of the states are not countered by a system with no limits on the control input, those are limited and converted from divergent oscillations to periodic ones when actuators have saturation limits. When a system has a divergent oscillatory dynamic, the amplitude of the oscillation keeps increasing, while its frequency remains constant. Therefore, when a saturation block is applied to such a signal, the result is a squared wave which does necessarily makes the system response diverge.

It also must be mentioned that in the INDI based control system designed for the two bodies model, the state to be controlled is directly observable and its dynamic includes the structural eigenmotion. Therefore, the oscillatory contribution is not to be discarded, otherwise, the control task will not be achieved. On the contrary, in more common applications, drones are provided with one set of gyroscopes that measures different contributions from many structural eigenmotion. Therefore, when the state to be controlled is not directly observable, a change in the state space representation base must be applied to better implement the INDI control system design procedure described in 4.

## 5.3. Preliminary analysis conclusion

During the preliminary analysis projects, the interaction between INDI based flight control systems and structural dynamics in drones have been studied in depth.

Firstly, ground vibration tests for system characterization and flight tests for phenomena analysis have been executed. From the frequency domain analysis of flight, tests emerged that indeed the aforementioned interaction is present, but the specific implementation can be avoided by decreasing the attitude angle tracking loop proportional gain. Moreover, it was shown that the inner attitude rate controller has little to no influence on the structural vibration recorded during the tests.

Secondly, two different notch filters were implemented and integrated into the control system with the goal to damp specific frequency components. The effect of the aforementioned filters was to lower the frequency of the lightly damped structural eigenmotion.

Finally, two dynamic systems simulating the roll dynamic of a Parrot Bebop 2 were implemented in Simulink®, one considering the to be simulated system as constituted by one rigid body and one considering the Bebop two roll dynamic as a system composed of two rigid bodies hinged in the same point and connected via a spring-damper system. Two different INDI controllers were implemented, one meant to control the angular position of the one body dynamic model and the other meant to fulfil the same task but for the two bodies model. Then, each controller is applied to the respective system. Moreover, the one body dynamic controller is also applied to the two bodies dynamic model to simulate the flight test mentioned above.

From the spectral analysis of the dynamic system - control system couples emerge that on one side, structural dynamics are lightly excited when the control system is applied to the designated system. On the other hand, when the control system developed for the one body model is applied to the two bodies model, the structural dynamic is excited and contributes to the system response with self-sustained oscillations.

6

# Conclusion

The literature survey touched on different subjects such as structural dynamics, aerodynamic and nonlinear control system design. First, the derivation of the analytical equations describing the vibrations of continuous bodies and their reduction in a state-space like-form was presented. It was followed by the description of the structural integrity implication and rigid motion stability when flexible eigenmodes interact with flight control systems and unsteady aerodynamics. This interaction can lead to both unstable rigid body dynamics and to divergent structural vibration which eventually generates structure failures. Later, current methods for avoiding FCS - flexible motions interaction and for flexible mode stabilization were presented. Finally, a nonlinear dynamic inversion-based flight control system theoretical description was provided, followed by a review of successful NDI and INDI controller implementations, to end with a discussion regarding both control strategies characteristics. All the different research fields have been studied in-depth, providing a solid and extensive theoretical background for the execution of the incoming master thesis project.

The literature survey has highlighted some key aspects and trends of the recent academic research about flight control systems and aeroservoelasticity. Due to the introduction of new materials and the need of saving weight on aircraft, the structure of aeroplanes has become slenderer and thinner (Malisani *et al*., 2021 [14]; Silvestre *et al*., 2017 [22]). This has led to an overlapping of rigid body motion frequencies and structural eigenmodes frequency which does not allow flight control system designers to neglect or filter out aeroelastic or vibration phenomena.

Similar phenomena can be experienced also in smaller air vehicles such as Parrot Bebop 2 as previously shown in chapter 5, and the Nederdrone (de Wagter *et al*., 2021, [6]) Therefore, MAVs are a perfect testbed for innovative aircraft design and flight control system design ideas due to them being cheap and not imposing any limit on the possible configurations. Thus, research on interactions between aeroelastic phenomena and flight control systems can be carried out on a MAV vehicle without losing generality or relevance. In addition, due to the high customization level and the easiness and quickness on apply modifications on different subsystems of the air vehicle, the research process is subjected to an enhancement in its progress rate, allowing the researcher to be more effective in his or her work.

Moreover, while executing the literature survey, some research questions partially found an answer. It was proved by Mooij (2020) [15] and Groondman (2018) [11] that INDI controller can be applied to flexible aircraft when structural dynamics are not present in the plant model utilized to design the flight control system. Furthermore, it is shown that structural dynamics can be considered in the INDI FCS design and an appropriate virtual input can be given to reach the control objective (Wang, 2019 [30]). Moreover, in the work by Wang et al. (2019) [30], the wing stiffness was reduced by 80% showing that phugoid motion-related poles are moved to the right half complex plane, introducing instability. Thus, a rough estimation of how the stability of an INDI controlled plant is affected by structure characteristics is provided. Clearly, this is only a qualitative result and which heavily depends on the plant model itself and it differs for each aircraft configuration.

It was found in many papers ([13], [30] ) that it is always possible to reduce the structural model in terms of the number of solutions of the partial derivative differential equation considered for the structural vibration description. Most of the time the choice is driven by the impossibility to place as many accelerometers as required to capture the behaviour of all the desired flexible motions. Other times the reduction is operated to keep the computational effort bounded. Generally speaking, the more bending functions are considered in the PDE solution, the higher is the associated frequency of the last contribution considered. Therefore, for high-frequency bending modes, the implementation of a notch filter is still a viable solution, which does not drastically affect the flight control system performances for high cut-off frequency. However, in the aforementioned case, high-frequency bending modes should not interact with rigid body flight control systems due to the high separation in frequency content.

As reported in 3.2.1, the implementation of notch filters, or more in general of signal filtering, is always discouraged due to the phase lag those introduce on the feedback loop.

Finally, once again Wang *et al.* (2019) [30] show that INDI control systems can include structural flexible dynamics in the model used to design the controller. Therefore, by showing solid robustness qualities and effectiveness in the assigned task of providing gust load alleviation, INDI proves itself to be a good candidate to provide a reduction of the structural motion interaction with flight control systems via the integration of elastic modes in the controller design.

The preliminary analysis studies have also provided some useful insight into the research questions. In chapter 5 is showed how a properly designed INDI based flight control system can avoid interacting with structural eigenmotions. Meanwhile, they also showed what are the consequences of the application of a non optimally designed INDI control system to a non strictly related system and how to mitigate such consequences, with the lowering of the outer control loop gains, therefore providing initial answers for subquestions 1.2 and 2.2. The simulation tests showed how it is a better practice to include the structural model of the drone into the INDI implementation rather than apply filters lately.

Additionally, it allowed to already experience what kind of implementation and test issues will be likely to encounter later on in the thesis project during the phases of development, design and implementation of the flight control system.

# References


[1] M. I. Alabsi and T. D. Fields. "*Quadcopter Experimental Evaluation of Nonlinear Dynamic Inversion Coupled with Fourier Transform Regression*". In: *AIAA Guidance, Navigation, and Control Conference AIAA* January (2017), pp. 1–13. DOI: 10.2514/6.2017-1911.

[2] G. Avanzini, E. Capello, and I. A. Piacenza. "*Mixed newtonian-lagrangian approach for the analysis of flexible aircraft dynamics*". In: *Journal of Aircraft* 51.5 (2014), pp. 1410–1421. DOI: 10.2514/1.C032235.

[3] J. Becker, B. Caldwell, and V. Vaccaro. "*The interaction of flight control system and aircraft structure / Structural Aspects of Flexible Aircraft Control*". In: (2014).

[4] R. J. Caverly et al. "*Nonlinear Dynamic Inversion of a Flexible Aircraft*". In: *IFAC-PapersOnLine* 49.17 (2016), pp. 338–342. DOI: 10.1016/j.ifacol.2016.09.058.

[5] B. P. Danowsky et al. "*Modal isolation and damping for adaptive aeroservoelastic suppression*". In: *AIAA Atmospheric Flight Mechanics (AFM) Conference* (2013), pp. 1–19. DOI: 10.2514/6.2013-4743.

[6] C. De Wagter et al. "*The NederDrone: A hybrid lift, hybrid energy hydrogen UAV*". In: *International Journal of Hydrogen Energy* 46.29 (2021), pp. 16003–16018. DOI: 10.1016/j.ijhydene.2021.02.053.

[7] E. Dowell, J. Edwards, and T. Strganac. "*Nonlinear aeroelasticity*". In: *Journal of Aircraft* 40.5 (2003), pp. 857–874. DOI: 10.2514/2.6876.

[8] D. Drewiacki, F.J. Silvestre, and A. B. Guimarães Neto. "*Advantages of using aeroelastic feedback in flexible aircraft control instead of applying notch-filtering*". In: *International Forum on Aeroelasticity and Structural Dynamics 2019, IFASD 2019* June (2019), pp. 1–10.

[9] A. Elmelhi. "*Modified Adaptive Notch Filter Based on Neural Network for Flexible Dynamic Control*". In: *International Journal of Computer and Electrical Engineering* 6.2 (2014), pp. 185–190. ISSN: 17938163. DOI: 10.7763/ijcee.2014.v6.819.

[10] M. Goman and A. Khrabrov. "*State-space representation of aerodynamic characteristics of an aircraft at high angles of attack*". In: *Astrodynamics Conference, 1992* 31.5 (1992), pp. 759–766. DOI: 10.2514/6.1992-4651.

[11] F. Grondman et al. "*Design and flight testing of incremental nonlinear dynamic inversion based control laws for a passenger aircraft*". In: *AIAA Guidance, Navigation, and Control Conference, 2018* 0.210039 (2018). DOI: 10.2514/6.2018-0385.

[12] E. Livne. "*Aircraft active flutter suppression: State of the art and technology maturation needs*". In: *Journal of Aircraft* 55.1 (2018), pp. 410–450. DOI: 10.2514/1.C034442.

[13] M. Majeed and G. Madhavan. "Reduced Order Model Based Flight Control System for a Flexible Aircraft". In: *IFAC-PapersOnLine* 53.1 (2020). 6th Conference on Advances in Control and Optimization of Dynamical Systems ACODS 2020, pp. 75–80. DOI: https://doi.org/10.1016/j.ifacol.2020.06.013.

[14] S. Malisani, E. Capello, and G. Guglieri. "Development of a Flight Mechanics Simulation Computer based on a Flexible Aircraft Model for a Regional Aircraft". In: *IOP Conference Series: Materials Science and Engineering* 1024 (Jan. 2021), p. 012066. DOI: 10.1088/1757-899x/1024/1/012066.

[15] E. Mooij. "*Robust control of a conventional aeroelastic launch vehicle*". In: *AIAA Scitech 2020 Forum* 1 - Part F, Orlando - FL, United States.January (2020), pp. 1–25. DOI: 10.2514/6.2020-1103.

[16] J.A Mulder et al. *Flight Dynamics - AE3202 Lecture Notes*. Kluyverweg 1, 2629 HS Delft, The Netherlands: TU Delft - Faculty of Aerospace Engineering, 2013.

[17] C. Papageorgiou. "*Robustness analysis of a nonlinear dynamic inversion controller for an aeroservoelastic flight vehicle*". In: *European Space Agency, (Special Publication) ESA SP* 606 (2006), pp. 573–582.

[18] A. A. Paranjape et al. “Dynamics and performance of tailless micro aerial vehicle with flexible articulated wings”. In: *AIAA Journal* 50.5 (2012), pp. 1177–1188. DOI: 10.2514/1.J051447.

[19] A. Radke and Z. Gao. “*A survey of state and disturbance observers for practitioners*”. In: *Proceedings of the American Control Conference* 2006.July 2006 (2006), pp. 5183–5188. DOI: 10.1109/acc.2006.1657545.

[20] Singiresu S. Rao. *Vibration of Continuous Systems*. Hoboken, NJ, United states of America: John Wiley & Sons - Digital edition, 2007. ISBN: 978-0-471-77171-5.

[21] S Sieberling, Q P Chu, and J. A. Mulder. “*Robust Flight Control Using Incremental Nonlinear Dynamic Inversion and Angular Acceleration Prediction*”. In: *Journal of Guidance, Control, and Dynamics* 33.6 (2010). DOI: 10.2514/1.49978.

[22] Flávio J. Silvestre et al. “*Aircraft control based on flexible aircraft dynamics*”. In: *Journal of Aircraft* 54.1 (2017), pp. 262–271. DOI: 10.2514/1.C033834.

[23] E.J.J. Smeur, Q. Chu, and G.C.H.E. de Croon. “*Adaptive Incremental Nonlinear Dynamic Inversion for Attitude Control of Micro Air Vehicles*”. In: *Journal of Guidance, Control, and Dynamics* 39.3 (2016). DOI: 10.2514/1.G001490.

[24] E.J.J. Smeur, G.C.H.E. de Croon, and Q. Chu. “*Cascaded incremental nonlinear dynamic inversion for MAV disturbance rejection*”. In: *Control Engineering Practice* 73.January (2018), pp. 79–90. DOI: 10.1016/j.conengprac.2018.01.003. arXiv: 1701.07254.

[25] E.J.J. Smeur, G.C.H.E. De Croon, and Q. Chu. “*Gust disturbance alleviation with incremental nonlinear dynamic inversion*”. In: *IEEE International Conference on Intelligent Robots and Systems* 2016-Novem (2016), pp. 5626–5631. DOI: 10.1109/IROS.2016.7759827.

[26] P. R. Smith. “A simplified approach to nonlinear dynamic inversion based flight control”. In: 1998, pp. 762–770. DOI: 10.2514/6.1998-4461.

[27] Ashish Tewari. *Aeroservoelasticity - Modelling and control*. New York, NY, United States of America: Springer - Digital edition, 2015. DOI: 10.1007/978-1-4939-2368-7.

[28] T. Theodorsen, W.H. Mutchler, and United States. National Advisory Committee for Aeronautics. *General Theory of Aerodynamic Instability and the Mechanism of Flutter*. NACA R-496. National Advisory Committee for Aeronautics, 1935.

[29] C.C. Van Kampen E. J. de Visser. *Lecture notes - Nonlinear and adaptive flight control system design*. Kluyverweg 1, 2629 HS Delft, The Netherlands, 2020.

[30] X. Wang et al. “*Flexible aircraft gust load alleviation with incremental nonlinear dynamic inversion*”. In: *Journal of Guidance, Control, and Dynamics* 42.7 (2019), pp. 1519–1536. DOI: 10.2514/1.G003980.

[31] X. Wang et al. “*Stability analysis for incremental nonlinear dynamic inversion control*”. In: *Journal of Guidance, Control, and Dynamics* 42.5 (2019), pp. 1116–1129. DOI: 10.2514/1.G003791.

[32] M. R. Waszak and D. K. Schmidt. “*On the flight dynamics of aeroelastic vehicles*”. In: *Astrodynamics Conference, 1986* 25.6 (1986), pp. 120–133. DOI: 10.2514/6.1986-2077.

[33] Wei Xu et al. “*Full Attitude Control of an Efficient Quadrotor Tail-sitter VTOL UAV with Flexible Modes*”. In: *International Conference on Unmanned Aircraft Systems (ICUAS)* (2019).

# Appendix A: MATLAB®Simulink®simulation graphs

## Time domain responses

All the time domain responses graphs has time $[s]$ as variable on the x-axis and $[deg]$, $[Hz]$ or $[Hz^2]$ on the y-axis, respectively for the attitude angle, angular rate and angular acceleration variables.

### One body model based INDI controller - step response

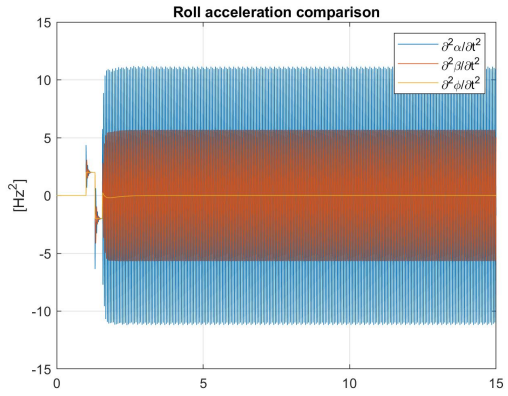


**Figure 1:** Angular acceleration response to step input time history

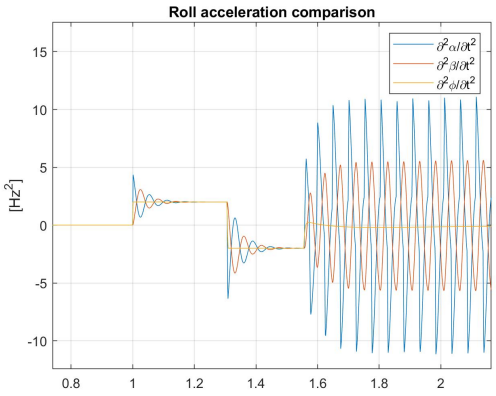


**Figure 2:** Angular acceleration response to step input time history - detail

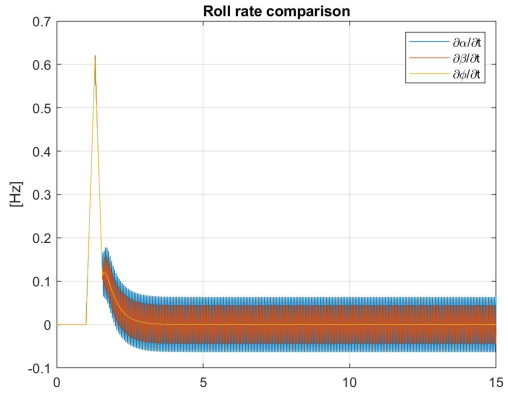


**Figure 3:** Angular rate response to step input time history

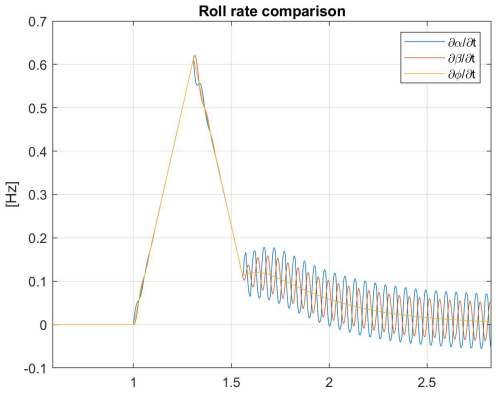


**Figure 4:** Angular rate response to step input time history - detail

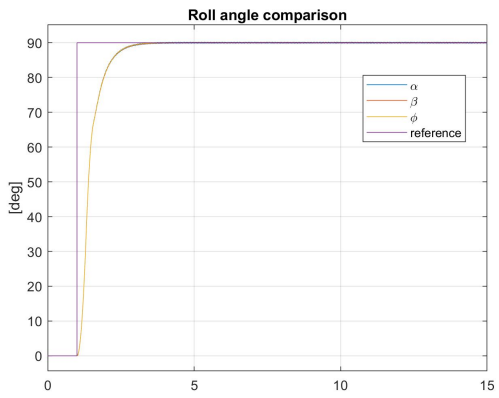


**Figure 5:** Angular position response to step input time history

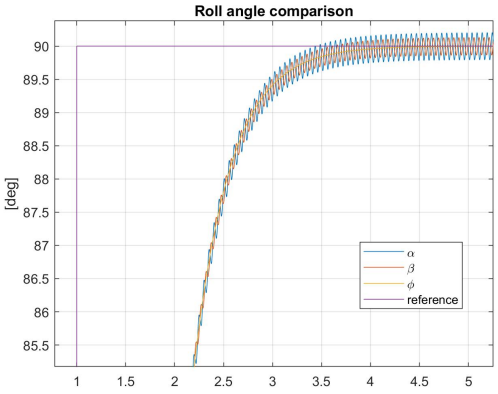


**Figure 6:** Angular position response to step input time history - detail

## One body model based INDI controller - impulse response

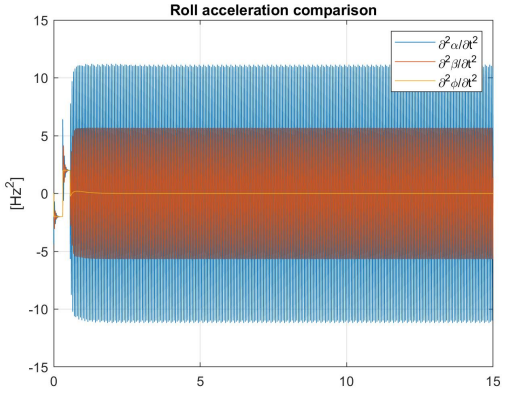


**Figure 7:** Angular acceleration response to step input time history

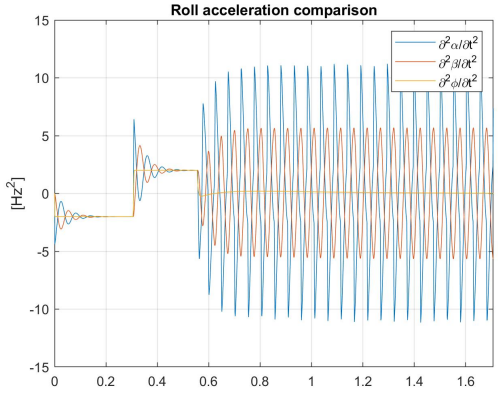


**Figure 8:** Angular acceleration response to step input time history - detail

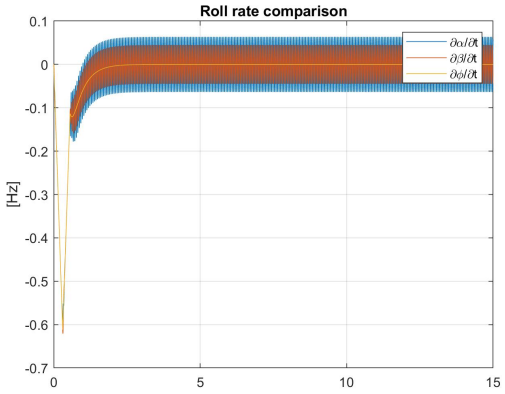


**Figure 9:** Angular rate response to step input time history

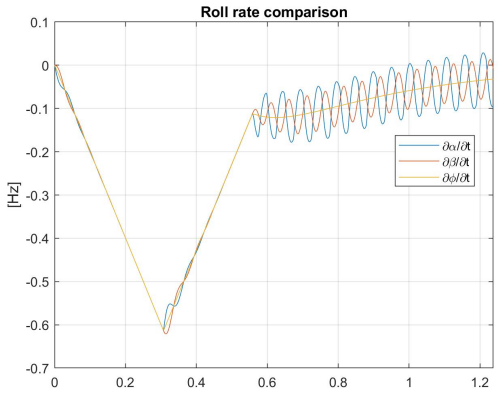


**Figure 10:** Angular rate response to impulse input time history - detail

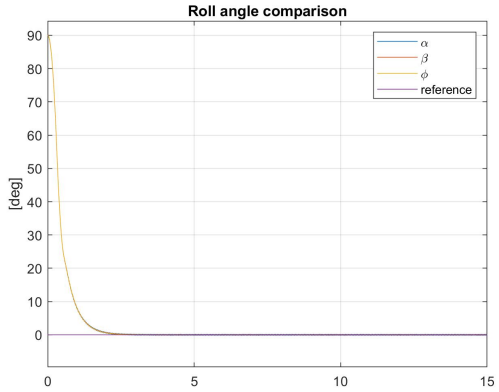


**Figure 11:** Angular position response to impulse input time history

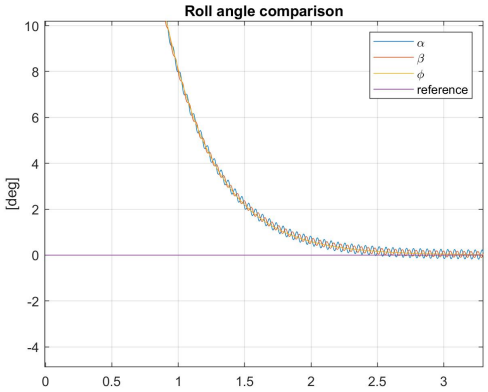


**Figure 12:** Angular position response to impulse input time history - detail

## Two bodies model based INDI controller - step response

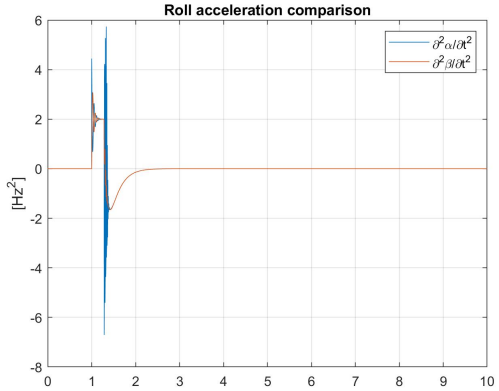


**Figure 13:** Angular acceleration response to step input time history

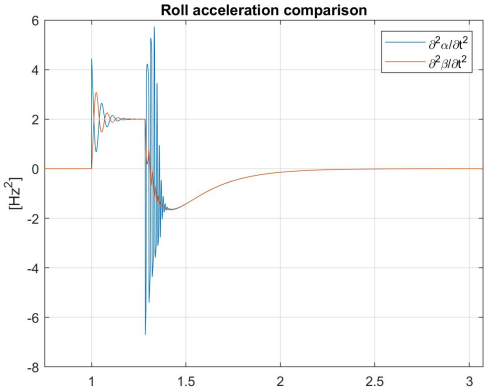


**Figure 14:** Angular acceleration response to step input time history - detail

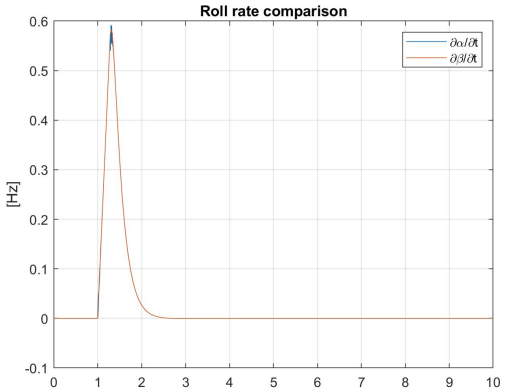


**Figure 15:** Angular rate response to step input time history

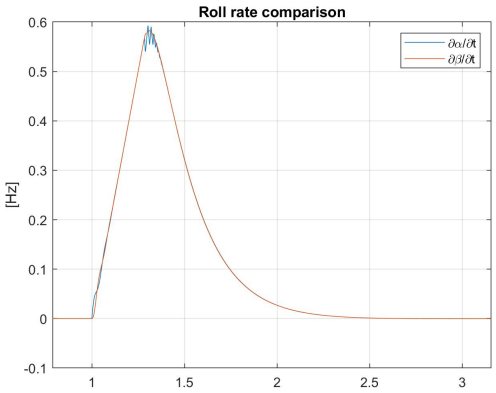


**Figure 16:** Angular rate response to step input time history - detail

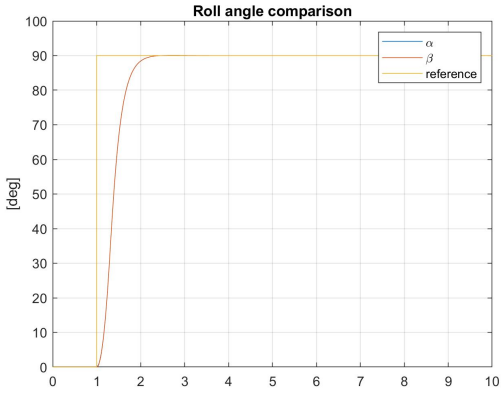


**Figure 17:** Angular position response to step input time history

## Two bodies model based INDI controller - impulse response

All the time domain responses graphs has time $[Hz]$ as variable on the x-axis and $[rad^2/hz]$, $[rad^2/s]$ or $[rad^2/s^3]$ on the y-axis, respectively for the attitude angle, angular rate and angular acceleration variables.

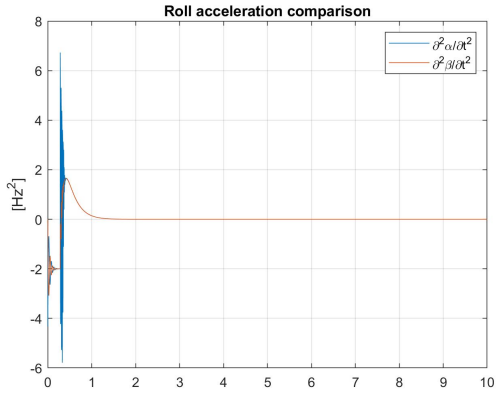


**Figure 18:** Angular acceleration response to impulse input time history

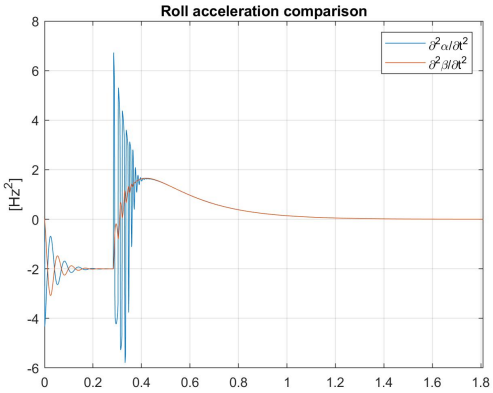


**Figure 19:** Angular acceleration response to impulse input time history - detail

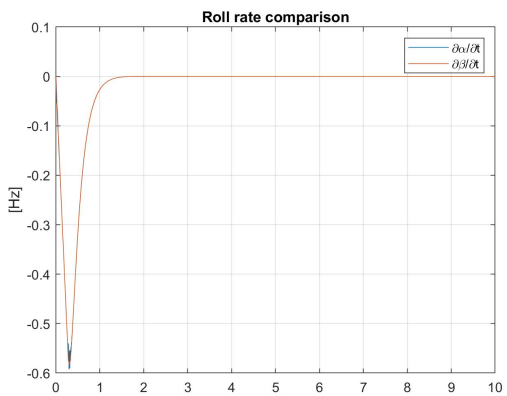


**Figure 20:** Angular rate response to impulse input time history

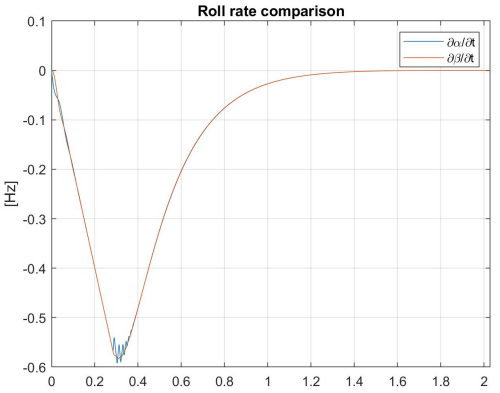


**Figure 21:** Angular rate response to impulse input time history - detail

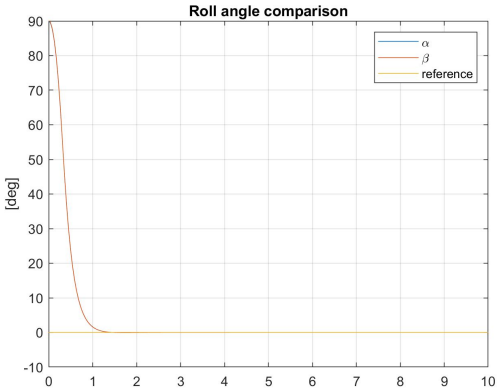


**Figure 22:** Angular position response to impulse input time history

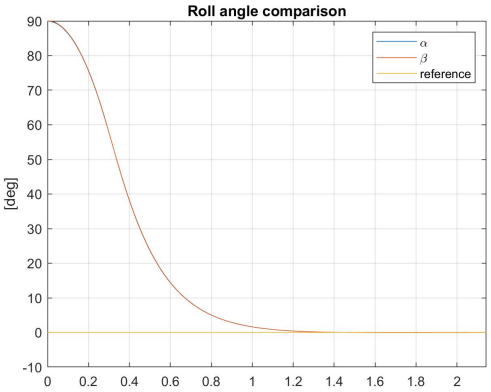


**Figure 23:** Angular position response to impulse input time history - detail

# Frequency domain responses

## One body model based INDI controller - step response

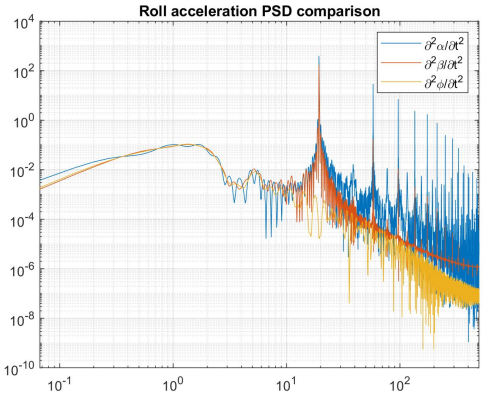


**Figure 24:** Angular acceleration response to step input PSD function

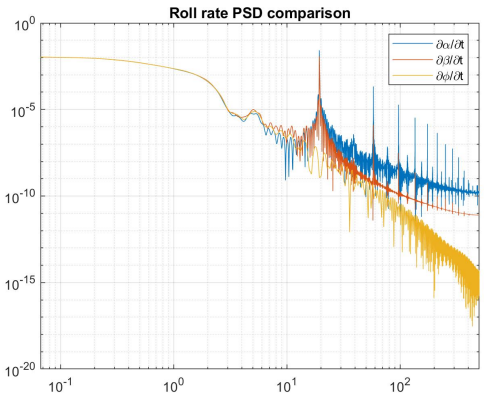


**Figure 25:** Angular rate response to step input PSD function

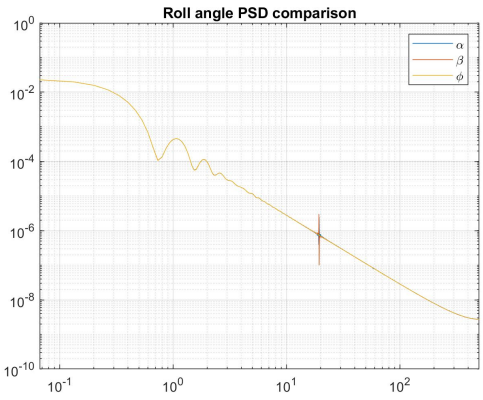


**Figure 26:** Angular position response to step input PSD function

## One body model based INDI controller - impulse response

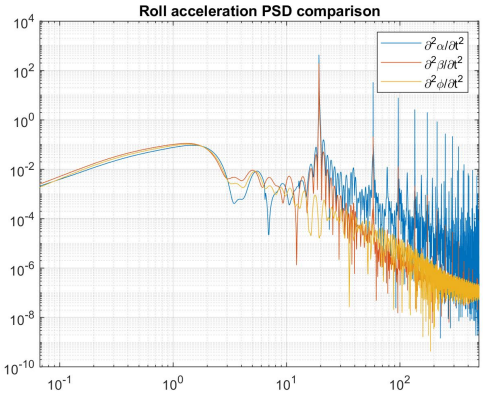


**Figure 27:** Angular acceleration response to impulse input PSD function

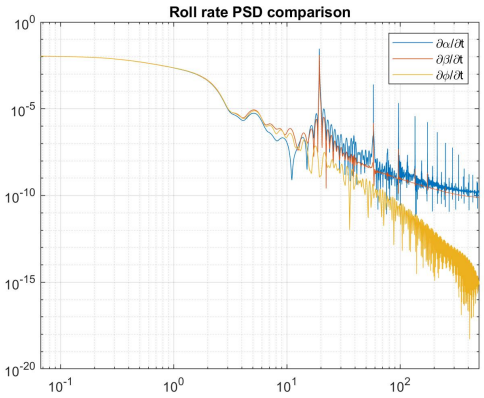


**Figure 28:** Angular rate response to impulse input PSD function

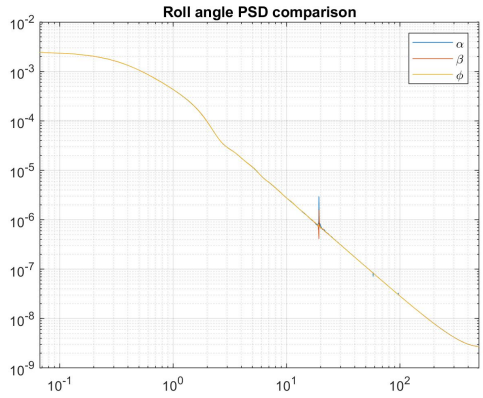


**Figure 29:** Angular position response to impulse input PSD function

## Two bodies model based INDI controller - step response

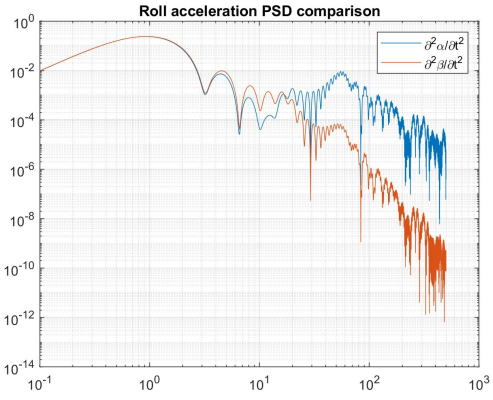


**Figure 30:** Angular acceleration response to step input PSD function

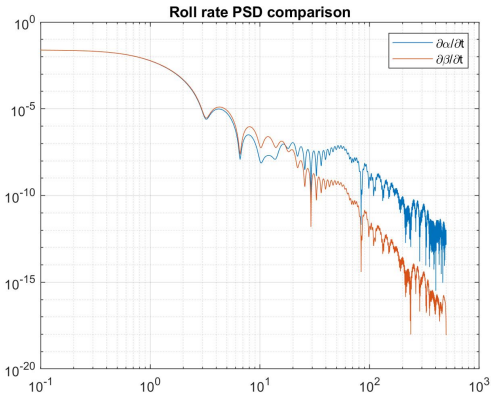


**Figure 31:** Angular rate response to step input PSD function

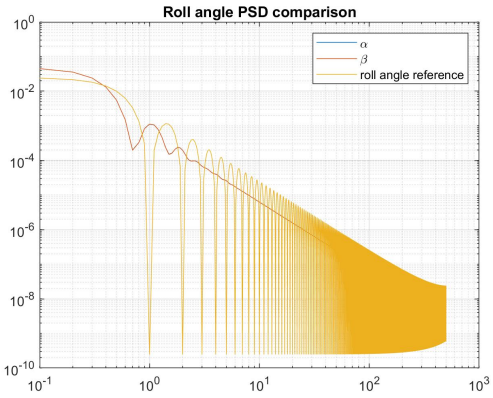


**Figure 32:** Angular position response to step input PSD function

## Two bodies model based INDI controller - impulse response

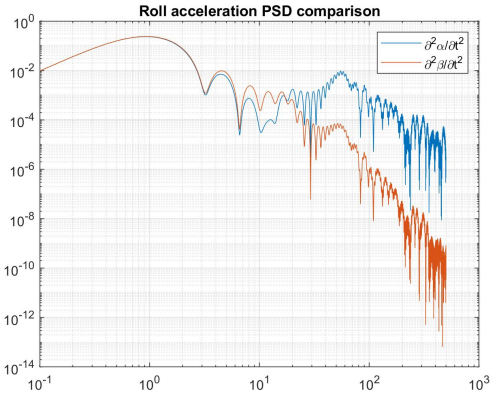


**Figure 33:** Angular acceleration response to impulse input PSD function

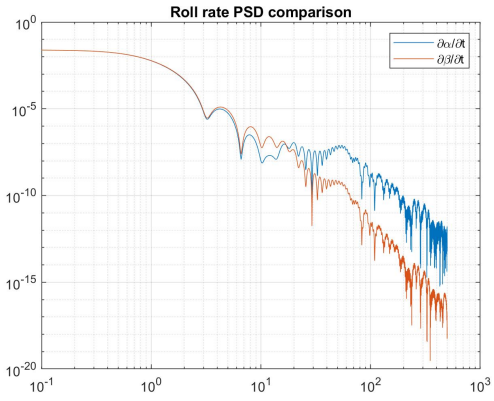


**Figure 34:** Angular rate response to impulse input PSD function

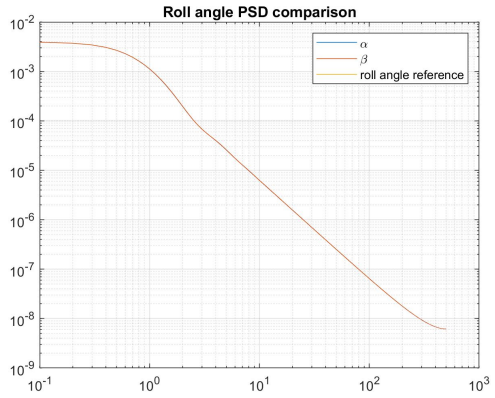


**Figure 35:** Angular position response to impulse input PSD function

# 3

# Scientific paper

# Investigation of the interaction between incremental nonlinear dynamic inversion flight controller and the structural properties of a drone

Alessandro Collicelli
*dept.of Control & Simulation*
*Delft University of Technology*
Delft, The Netherlands
a.collicelli@student.tudelft.nl

***Abstract*—Incremental Nonlinear Dynamics Inversion (INDI) flight controllers are sensor-based control systems, that are robust towards model uncertainty and with good disturbance rejection characteristics. These controllers show coupling effects in structural modes when implemented in specific flying vehicles with low-frequency structural motions. This paper investigates different INDI implementations, standard INDI, hybrid INDI, and notch filter placement in the INDI loop via simulation and flight tests on the Nederdrone. System identification of the structural characteristics of the vehicle and the system's yaw dynamics are executed via ground vibration and hover flight tests. Closed-loop behaviour of the INDI inner-loop, disturbance rejection performance, and outer loop step-tracking performance was assessed with dedicated flight tests. The investigated INDI solutions show similar disturbance rejection and outer-loop step-tracking performance, while the hybrid INDI solution performs a better nonlinear dynamic inversion.**

***Index Terms*—INDI, complementary filter, unmanned vehicle, flight control system structural motion coupling**

## I. Introduction

In recent years, aerospace structures have become increasingly thin and slender, due to the introduction of new structural materials and the need to decrease the amount of weight dedicated to the structural elements [1]. Consequently, the structural properties of these aircraft change, moving the natural frequency of structural modes closer to the rigid body ones, into the bandwidth of flight controllers. Therefore, the structural element contribution to the signal fed to the flight control laws is more dominant than for more rigid aircraft [2]. This generates an undesired interaction between the flight control system and the structural motions that can lead to instability of both the controlled system [3].

Common solutions are to apply a low-pass filter to the feedback signal or to apply a notch filter to the controller command, to suppress the contribution of the structural modes which makes the whole system unstable [4, 5]. However, when the structural dynamics' bandwidth overlaps the rigid body motion's one, the filtering solution will affect the controller performance by damping the magnitude and increasing the lag of the feedback signal also over the rigid body motion frequency range. Some approaches deal with this issue by taking into account the effects of the structural modes in the system dynamics and the sensors' measurements and designing a multi-objective controller which can both properly control the rigid body dynamic while damping the structural modes [6]. The availability of multiple accelerometers and gyroscope units to obtain an estimation of the structural modes states (observably of the states), and sufficient actuator bandwidth to operate on the structural modes' states are the underlying hypothesis of this solution.

Incremental non-linear dynamics inversion (INDI) is a sensor-based control system design technique, which linearizes a system's non-linear dynamics to enable the use of linear control design methods. The calculation of the variation of the system input is based on the inversion of the first-order approximation of the dynamics equations and knowledge of the effectiveness of the actuator is required. INDI controllers have proven to have good disturbance rejection characteristics [7, 8] and to be robust to model mismatches [6, 9].

Nevertheless, INDI based flight controller has been found to be unstable when implemented in basic form for the Nederdrone [10], an unmanned and electrical tail-sitter drone with vertical take-off and landing capabilities Figure 1. During hover flight, the aircraft shows self-sustained oscillations in the yaw axis when heavy filtering is not applied. Therefore, it is chosen as a test platform to investigate the interaction between the INDI control system and structural dynamics. In this paper, the interaction between different INDI-based flight controllers and the structural modes of the Nederdrone are investigated, such as conventional INDI [10], hybrid INDI [11], notch filter application on the system input [5] and Kalman filter for angular acceleration estimation. The goal is to find a

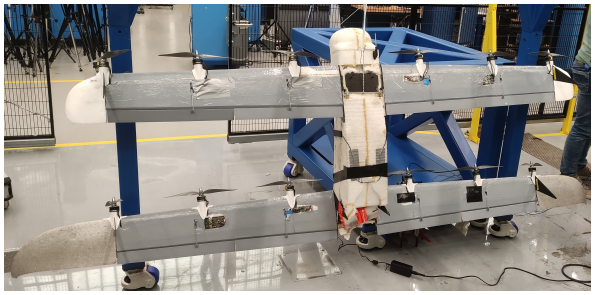

Fig. 1. The chosen test platform, the Nederdrone

solution that minimizes the filtering of the sensor signal, while still achieving good performance.

The structure of the paper is as follows. First, the characteristics of the test platform are outlined in section II, together with the INDI controller developed in [10]. Section III describes the system identification processes required to set up a simulation environment for the dynamics of interest and to develop the investigated solutions. After, the design choices of the different INDI solutions are laid out in section IV, followed by the description of the results of the performance investigation via simulation and flight test in section V. After the conclusion, appendix A provides a theoretical background to the INDI-based control system and in appendix B extra information regarding the ground vibration test setup and results are reported.

## II. Nederdrone description, limitation and INDI design

### A. Vehicle description

The Nederdrone is a tail sitter and unmanned flying vehicle with two wings, as shown in Figure 1, capable of vertical take-off and landing. It has twelve propellers, three for each semi-wing, eight control surfaces, one aileron, and one flap for each semi-wing. The propellers can be modeled as first-order systems with a cut-off frequency of 18 $rad/s$. The servos moving the control surfaces are assumed to behave as a first-order model with a cut-off frequency of 50 $rad/s$ and a rate limitation of 63.7 $rad/s$ [1][12]. The wings are connected to the fuselage, which is an empty foam cylinder that houses the batteries, the autopilot, and other hardware. The autopilot has three built-in accelerometers and three built-in gyroscopes, one for each control axes. This sensor setup is designed to measure the behavior of the rigid body motion of the aircraft, and it is not suitable for structural modes state observation, due to the lack of sensors measuring along the same axis. Limited actuator bandwidth and limited system observability make the application of an active vibration suppression strategy impossible without modification to the system.

[1]*Servo actuator specifications*, https://www.servocity.com/hs-5086wp-servo

Two carbon fiber rods connect two half-wings, while the front wing is connected to the back wing with four extra carbon fiber rods. The placement of these structural elements can be represented as an empty cylinder or a cylindrical thin shell.

Therefore, the torsional rigidity of the fuselage results is low, and it is an indicator of the presence of low-frequency torsional mode on the fuselage.

### B. Inner INDI loop flight controller design

The Nederdrone control architecture for both autonomous and piloted flight is thoroughly described by De Wagter *et al.*[10], and it is based on two nested INDI-based control loops. For the current purpose, only the attitude control loop coupled with the linear acceleration control along the vertical axis of the body reference frame of the vehicle $z_B$, is considered. The dynamics equations used for the design are the Euler equations for the rotational dynamics of a rigid body and the Newton equation applied along the vertical axis of the body reference frame of the vehicle $z_B$ (1).

$$\dot{\vec{x}} = \begin{bmatrix} \dot{\vec{\omega}} \\ \ddot{z}_B \end{bmatrix} = \begin{bmatrix} I^{-1} \cdot \left( -\vec{\omega} \times I\vec{\omega} + \vec{M}_{ext} \right) \\ -\frac{g}{\cos\phi\cos\theta} + F_{z_B}/m \end{bmatrix} = \tag{1}$$

$$\vec{f}(\vec{x}) + \mathbf{G} \begin{bmatrix} u_p \\ u_q \\ u_r \\ u_T \end{bmatrix} = \vec{f}(\vec{x}) + \mathbf{G}\vec{u}$$

Where $\vec{\omega} = [p, q, r]^T$ is the vector of the rotational rates along the $x_B$, $y_B$ and $y_B$ body axes, $\vec{f}(\vec{x})$ is nonlinear functions describing the contribution of the states to their own dynamic and $\mathbf{G}$ is the control effectiveness of the control inputs $\vec{u} = [u_p, u_q, u_r, u_T]^T$. $\vec{M}_{ext}$ and $F_{z_B}$ are the torques and the force generated with the propellers and the control surfaces. By applying the INDI design process for this system, (1) is linearized in (2) and the INDI control law is obtained in (3).

$$\dot{\vec{x}} = \dot{\vec{x}}_0 + \frac{\partial \vec{f}(\vec{x}_0)}{\vec{x}} \Delta\vec{x} + \frac{\partial \mathbf{G}(\vec{x}_0, t_0)\vec{u}}{\vec{u}} \Delta\vec{u} \tag{2}$$

$$= \dot{\vec{x}}_0 + A(\vec{x}_0)\Delta\vec{x} + \mathbf{G}\Delta\vec{u}$$

$$\nu = \dot{r} = \dot{r}_0 + g_1 \Delta u_r + g_2 \Delta \dot{u}_r = \tag{3}$$

$$\dot{r}_0 + (g_1 + g_2)\Delta u_r - g_2 z^{-1} \Delta u_r$$

The term $\dot{\vec{x}}_0$ is assumed to be measurable, $\dot{\vec{x}}$ is substituted by $\vec{\nu}$, which is the reference value for each element of $\dot{\vec{x}}$ and it is provided by external loops.

The term $A(\vec{x}_0)\Delta\vec{x}$ which describes the effect that a change in the state value has on the state itself, is commonly considered to have a slower and a smaller effect on the body dynamic than the actuator contribution. For very small time intervals the change in input is much

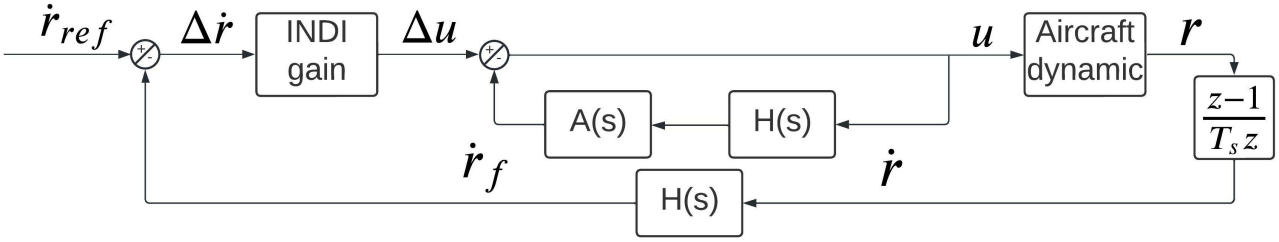


Fig. 2. Angular acceleration INDI control loop

faster than the change in state [13] and in the INDI design practice this is commonly known as the time scale separation principle [9]. Therefore, the $A(\vec{x}_0)\Delta\vec{x}$ term is neglected.

The control effectiveness matrix $\mathbf{G}$ is constant and diagonal, so that each element of the input vector acts on one axis, making the four control axes independent from one another. Since the phenomenon of interest manifests itself in the yaw rotation dynamics only this axis is considered from now on. The control effectiveness matrix element related to the yaw control input accounts also for the inertial effect due to the change in rotational speed of the propeller. This contribution is proportional to the derivative of the angular rate of the propellers which is proportional to the propeller command $u_r$ for the yaw axis. The angular acceleration of the propeller is calculated using a discrete approximation of the derivative in the $z$ domain since the propeller command is by nature a discrete signal. When including that contribution to (2) and considering only the yaw axis we obtain (3). When solving (3) for the control input, (4) is obtained, where

$$\Delta u_r = (g_1 + g_2)^{-1}(\nu - \dot{r}_0 + g_2 z^{-1}) \tag{4}$$

The yaw angular acceleration $\dot{r}_0$ is calculated from discrete differentiation of the gyroscope signal and it is later filtered with a second-order Butterworth low pass filter, with a cut-off frequency of 0.5 $Hz$. This low cut-off frequency aims to avoid the structural modes polluting the rigid body yaw angular acceleration measurement.

The variation to be applied to the previous control input is calculated in (4), and it is added to the previous control input before being fed as a command to the actuators. The control input's variation is limited to half of the maximum absolute value of the actuator's command. It is important to guarantee the synchronization between the control command and the actuator position and to avoid actuator saturation [13]. The control command calculated in the previous time step is filtered with the actuator dynamics transfer function before being added to the control input increment calculated in the current time step. The actuators' dynamic is modeled as the same first-order system that represents the propeller dynamic described in II-A. The same Butterworth filter applied to the angular acceleration measurement signal is applied to the control command calculated in the previous step, to ensure synchronization between the angular acceleration measurement and the control input signal. The angular acceleration INDI controller is shown in Figure 2, including the actuator synchronization loop (ASL). The ASL loop described above is shown in Figure 2 but circumscribed to the inner loop, where $A(z)$ is the actuator dynamic transfer function, and $H(z)$ is the Butterworth filter transfer function.

The reference for the angular acceleration signal $\nu$ is provided by the outer proportional attitude rate control loop. The angular rate is obtained from the gyroscope measurement and it is filtered with a second-order Butterworth low-pass filter with a cut-off frequency of 4 $Hz$ ($H(s)$ in Figure 3).

It is worth mentioning that the cut-off frequencies of the Butterworth filters for the angular accelerations and rates on the roll and pitch axes are respectively 5 $Hz$ and 20 $Hz$. The reduction in filter cut-off frequency was implemented to avoid the interaction between the controller and the low-frequency structural modes.

The yaw rate reference is provided by the heading angle control loop, which is again a proportional control loop. The yaw angle is obtained from GPS information during open-air flights and using a system that tracks the movement of markers applied to the drone during indoor flights. The structure of the yaw attitude controller is shown in Figure 3

### C. Control signal allocation

The control inputs in $\vec{u}$ are fed to every single actuator with a specific control allocation strategy. Since the control system is implemented in Paparazzi Autopilot [14] framework, some quantities are expressed in $pprz$ units, which are integer numbers used for actuator control. During a hovering maneuver the control surfaces act only on the pitch and yaw motion, thus the actuator command is defined as in $\Sigma^i = 2 * (C^i_{\Sigma q} u_q + C^i_{\Sigma r} u_r)$, bounded between -6000 and 6000 $pprz$. $C^i_{\Sigma q}$ and $C^i_{\Sigma r}$ are control allocation constants defined for each actuator which ensures coher-

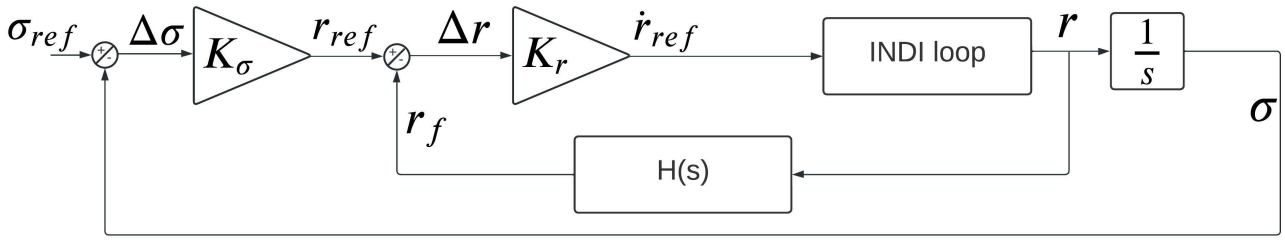


Fig. 3. Yaw axis controller structure

ence between the actuator's contribution to the system dynamics and the control command.

The propeller command is calculated as follows: first, the roll command $u_p$, pitch command $u_q$, and thrust command $u_T$ are used to obtain an initial propeller command $P_j^-$ (5). Then the yaw command is added to the initial propeller command and the overflow of the total command for each propeller is calculated (6). The maximum overflow value $O$ is used to obtain the yaw authority $u_{r\chi}$ (7), which is used to bound the value of the yaw command, obtaining a bounded yaw command $u_r^b$. '$boundAbs(x,y)$' is a function that returns $x$ if $x \in [-y, y]$, returns $-y$ if $x < -y$ and $y$ if $x > y$. Finally, the bounded yaw command is added to the initial propeller command calculated using only pitch, roll, and throttle command contribution and sent to each propeller to be executed. $C^j_{\Pi_p}$, $C^j_{\Pi_q}$, $C^j_{\Pi_r}$ and $C^j_{\Pi_T}$ are control allocation constants ensuring coherence between the torque or force generated by the actuator and the control inputs.

$$P_j^- = C^j_{\Pi_p} u_p + C^j_{\Pi_q} u_q + C^j_{\Pi_T} u_T \tag{5}$$

$$O = max_j(P_j^- + C^j_{\Pi_r} u_r - \Lambda) \tag{6}$$

$$u_{r\chi} = |u_r| - O \tag{7}$$

$$u_r^b = boundAbs(u_r, u_{r\chi})$$

$$P_j = P_j^- + C^j_{\Pi_r} u_r^b \tag{8}$$

where $\Lambda$ maximum allowed command value.

## III. System identification of the Nederdrone yaw dynamics

To gain knowledge of the structural properties of the Nederdrone and to obtain dynamic models that replicate the vehicle's yaw dynamic, ground vibration test and flight test were executed.

### A. Ground vibration test

The Nederdrone is hung on a structure by a rope, to simulate the hover condition and not affect the rigid body modes, at least around the yaw axis. The excitation to the structure is provided via a modal exciter or shaker (*2025E, ICP, PCB Piezotronics, Inc.*), which is connected to the aircraft structure with a rod. The force provided to the structure is measured using a load cell or force sensor (*288D01, ICP, PCB Piezotronics*) mounted at the end of a rod connected to the shaker and glued to the drone structure. The contact point is on a wing, to excite both symmetrical and asymmetrical bending and torsional modes. The displacement of the structure is measured using a laser scanning vibrometer camera (PSV-500 Scanning Vibrometer, Polytec). The test setup scheme is provided in Figure 4

The laser vibrometer camera can sense the displacement out of the geometrical plane defined by the drone's wings. Both the excitation instrument and the measurement instrument are connected to and controlled by the data acquisition computer, which is used to calibrate the camera, define the points in which measure the vehicle displacement from the equilibrium position and generate the input signal to provide to the Nederdrone's structure via the shaker. A chirp input complemented with white noise is applied to the structure. Using the data acquisition software, a local reference frame is defined based on co-planar points laying on the $X$-$Y$ body plane of the drone, the measurement points grid is built and the coordinates of all the points are automatically calculated.

The software executes multiple measurement runs and averaged the data across 10 measurement runs to obtain the best estimation of the frequency domain behavior of each measurement point. Each measurement run lasts 16 $s$ and the structure displacement is measured with a sampling rate of 500 $Hz$. At the end of the measuring process, each measurement point has an associated experimental transfer function. The data acquired during the ground vibration test are processed using Siemens Testlab Structure Modal Analysis software. The frequency domain data for each measurement point is blended together to perform a modal analysis of the vehicle's structure. The frequency interval upper bound for the estimation process is imposed at 35 $Hz$, while the lower bound is the one imposed by the sampling time of each data acquisition which is 16 $s$.

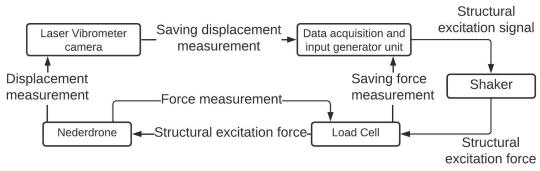


Fig. 4. Scheme of ground vibration test set up

A maximum limit of potential structural modes is provided as input to the software to avoid the identification of irrelevant modes. Then Siemens TestLab software provides the first guess for structural modes, then the operator has to choose the relevant ones so the software can iterate over those to provide the estimation of the structural mode. Then, a correlation analysis between the estimated modes is carried out, to ensure that the same mode is not identified as two very similar modes. If that is the case, the identification routine is executed once more being careful to not include modes that are too similar from the first guessed modes list.

Once a set of uncorrelated modes is obtained, the yaw dynamics-related modes are chosen with the aid of a graphic tool showing the deformation that each mode would generate in the structure. Therefore, knowing the position of the gyroscope measuring unit, two motions were found to be affecting the yaw angular acceleration measurement: the first torsional mode of the fuselage at a frequency of 3.75 Hz and the second torsional mode of the fuselage coupled with the bending mode of the wings at a frequency of 9.1 Hz. The shapes of these two modes are shown in Figure 29 and 30 from the appendix.

### *B. Flight test*

The Nederdrone is conducted to a hover flight condition, then the computer-generated input is substituted for the controller output for the yaw axis, simulating an open-loop system behavior for the yaw axis. The computer-generated yaw axis control signal and the gyroscope measurement of the yaw rate are recorded and saved for subsequent data processing. The time-domain inputs provided during different tests are chirp input and doublet input. A list of the relevant flight test input is provided in Table I.

### *C. Actuator modelling*

The propeller input to the dynamic system in the simulation must replicate two features: the dynamic behavior of the propeller and the yaw authority restriction on the yaw axis provided by the control signal allocation II-C. The propeller dynamic behavior is known and it is modeled by filtering the control signal with a first-order low-pass filter with a cut-off frequency of 18 $rad/s^{-1}$. When simulating only the yaw dynamics, the control signal quantities necessary to perform a correct control signal allocation are not available, since only the yaw axis controller is

TABLE I
LIST OF INPUT PROVIDED DURING FLIGHT TEST

| Test # | Input type | Ts [s] | Frequency interval [Hz] |
|---|---|---|---|
| 1 | Chirp | 17 | 1 - 4 |
| 2 | Chirp | 17 | 1 - 20 |
| 3 | Chirp | 17 | 1 - 20 |
| 4 | Chirp | 15 | 8 - 15 |
| 5 | Doublet | 4 | - |
| 6 | Doublet | 2 | - |
| 7 | Doublet | 2 | - |
| 8 | Chirp | 17 | 1 - 16 |
| 9 | Chirp | 12 | 1 - 16 |

simulated while the control allocation algorithm uses as input the roll, pitch, yaw, and thrust command. Thus, the control allocation effect is modeled as a limitation on the maximum and minimum values that $u_r$ can assume. The two boundary values are set to -1100 and 1100 and are obtained from the post-flight calculation of the $u_r^b$ value over time during a hover-flight.

To model the control surfaces contribution, three characteristics must be replicated: the control signal allocation, the dynamic behavior of the servo, and its rate limit. The control allocation is defined in simulation as $u_\Sigma = boundAbs(2 * u_r, 6000)$, which is the same definition provided in II-C when assuming $u_q = 0$. This assumption is an approximation but it holds during hover flight and it is proven to be valid also by flight test data. To include both the dynamic behavior and the servo rate limit, the frequency domain equation of the servo's dynamic $\dot{\delta_\Sigma} = -\tau_{act}\delta_\Sigma + \tau_{act}u_\Sigma$ is implemented as a set of Simulink®blocks. The quantity $\dot{\delta_\Sigma}$ is limited to the interval [-400, 400] $deg \cdot s^{-1}$ with a saturation block, to account for the servo rate limit. The implementation model is shown in Figure 5.

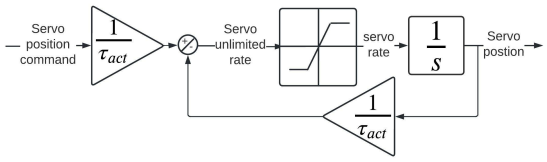


Fig. 5. Structure of control surface dynamic and rate limit implementation

The signal *servo command* is calculated by converting $u_r$ from $pprz$ unit to degrees, which is obtained through multiplication with the scaling constant 37.2/6000.

### *D. Full model for simulation purpose*

This model aims to provide a high-fidelity representation of the yaw dynamics of the Nederdrone, including both the rigid body and the structural dynamics within a specific frequency band. This frequency interval should contain the poles/eigenvalues related to the rigid body

motions and to the structural dynamics which cause the instability.

The chosen model structure is a two inputs one output Multi Input Single Output (MISO) transfer function model. The inputs are chosen to be the total propeller contribution and the total control surfaces contribution to the yaw dynamics. These two contributions are calculated by processing the logged yaw control signal with the actuator modeling processes described in III-C. The system output is the yaw angular acceleration and it is obtained starting from the angular rate measurement provided by the autopilot onboard gyroscopes. The gyroscope signal is first filtered using a second-order Butterworth filter with a cutoff frequency of 15 Hz. Then, the Butterworth filter output is differentiated using one step backward finite differences, to obtain the yaw angular acceleration.

Then, the flight test data outlined in III-B are used as data set to perform a frequency domain transfer function identification. A built-in algorithm from MATLAB®System Identification Toolbox called *'esttf.m'* is used for the transfer function identification process. The inputs to the algorithm are the Fourier transform of the input and output signals, the frequency interval of interest, and the number of poles the algorithm has to assume for the current transfer function estimation. This algorithm first operates a bilinear mapping transforming the frequency domain to the unity disk and then it operates consecutive iterations aiming to solve a nonlinear optimization problem [15]. The nonlinear least-squares loss function is reported in (9), where $\omega_k$ is the $k^{th}$ frequency coordinate, $D(\omega_k)$ is the denominator of the MIMO transfer function and $N_i(\omega_k)$ is the numerator of the transfer function from the $i^{th}$ input and the output. $u_i(\omega_k)$ is the Fourier transform of the $i^{th}$ input signal, $y(\omega_k)$ is the Fourier transform of the output signal and $W(\omega_k)$ is a frequency dependent weight which is defined as a pass-band filter over the [0.01, 20] $Hz$ frequency interval. $n_f$ is the number of frequency points and $n_u$ is the number of inputs of the system.

$$\underset{D,N_i}{\text{minimize}} \sum_{k=1}^{n_f} \left| \frac{W(\omega_k)}{D(\omega_k)} \left( D(\omega_k)\, y(\omega_k) - \sum_{i=1}^{n_u} N_i(\omega_k)\, u_i(\omega_k) \right) \right|^2 \tag{9}$$

Then numerator and denominator parameters are adjusted via linear refinement and the bilinear transformation executed at the beginning of the identification procedure is reverted to obtain the identified transfer functions.

Two accuracy estimation metrics are defined to assess the quality of the estimation. The first one is provided by the estimation routine report, and according to the function documentation is defined as in (10), and from now on it will be mentioned as *self metric*.

$$Fit\% = 100 \left( 1 - \frac{|\dot{r}_{measured} - \dot{r}_{model}|_2}{|\dot{r}_{measured} - \overline{\dot{r}_{measured}}|_2} \right) \tag{10}$$

TABLE II
LIST OF FULL MODEL ESTIMATION RUN

| Poles # | Self metric | Tischler metric $*10^3$ |
|---|---|---|
| 6 | -38.24 | 1.061 |
| 7 | -13.62 | 0.731 |
| 8 | -31.12 | 0.968 |
| 9 | 62.68 | 0.726 |
| 10 | -72.44 | 1.616 |

Where $\dot{r}_{measured}$ is the Fourier transform of the measured system output data and $\dot{r}_{model}$ is the calculated Fourier transform of the estimated model output given measured input. The *self metric* is a value between $-\infty$ and 100, being 100 when the output of the estimated model is exactly equal to the one measured during the experiment and it is zero when the output of the estimated model is the average of the measured output data.

The second metric used is taken from Tischler and Rample [16] and it is based on the comparison of the magnitude and phase of the estimated transfer function weighted on the coherence of the experimental frequency domain data. This metric will be called from now onwards the *Tischler metric*. The *Tischler metric* ($J_T$) (11) is reported for completeness.

$$J_T = \frac{20}{n} \sum_{i=1}^{n} W_\gamma(\omega_i)[W_g(|H_e(j\omega_i)| - |H_m(j\omega_i)|)^2 + W_p(\angle H_e(j\omega_i) - \angle H_e(j\omega_i))^2] \tag{11}$$

Where $n$ is the number of frequency points, $H_e(j\omega_i)$ is the value of the estimated transfer function at the frequency point $\omega = \omega_i$ and $H_m(j\omega_i)$ is the value of the system transfer function obtained from experimental data at the same frequency $\omega_i$. The values of the module and phase weights are $W_g = 1$ and $W_p = 1.745 \cdot 10^{-2}$. The value of the frequency point $W_\gamma(\omega_i)$ is reported in (12), where $\gamma_{xy}(\omega_i)$ is the value of the coherence function calculated from experimental data. All the weight values are taken from Tischler and Remple [16].

$$W_\gamma(\omega_i) = \left[ 1.58 \left( 1 - e^{-\gamma_{xy}^2} \right) \right]^2 \tag{12}$$

The *Tischler metric* is a cost function that scores zero when the bode plot of the estimated transfer function and the experimentally calculated one are the same, and which increases in its value with the increase in differences between the two aforementioned transfer functions.

Different estimations are run with a different pole number as an input and for each one of those the two accuracy metrics' value is calculated. In Table II all the estimation runs are reported together with the respective number of poles provided as an input and the accuracy metrics scores.

It is interesting to notice how identifications constrained to an even number of poles converge to a system with lower scores in the similarity metric than odd poles estimations. The system identification is executed only for the

yaw axis, which in the hovering condition is a combination of one aerodynamic mode (first order system) and multiple structural modes (second order systems). Therefore, the order of the resulting system is odd, which requires an odd number of poles to be described. The bode plot and the poles zeros map of the estimated transfer functions with the best accuracy metrics scores are reported in Figure 6 and Figure 7.

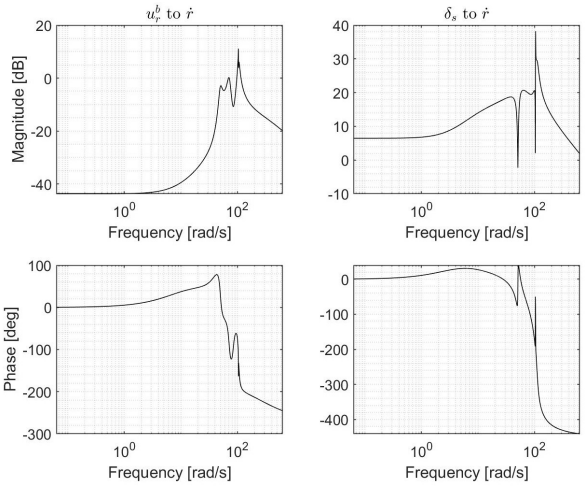


Fig. 6. Bode plot of the estimated MISO system

The obtained model is validated for two different conditions: time-domain open-loop response and frequency domain analysis of the system response in the closed loop. As shown in Figure 8 and Figure 9, the angular acceleration measured during a flight where the bounded yaw axis instability is happening is compared with the angular acceleration calculated using the estimated yaw dynamics model and the actuator command measured during the same flight.

Then, the estimated MISO system is integrated into

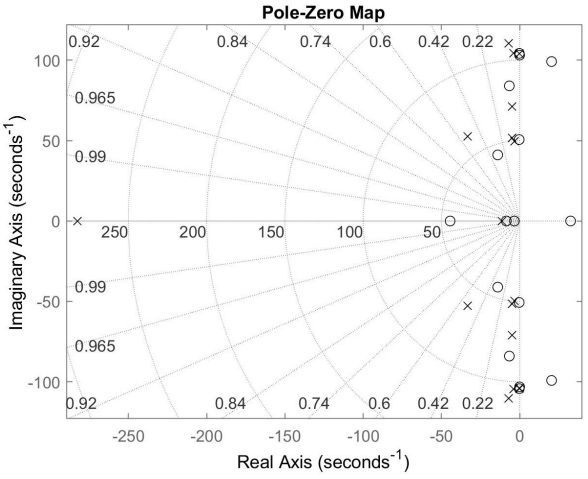


Fig. 7. Poles zeros map of the estimated MISO system

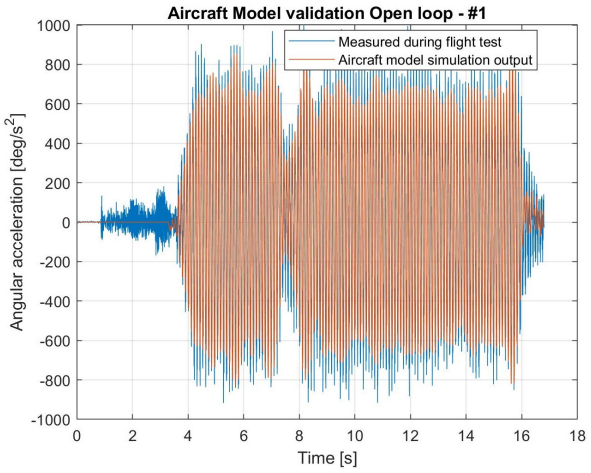


Fig. 8. Measured vs estimated angular acceleration for unstable flight condition

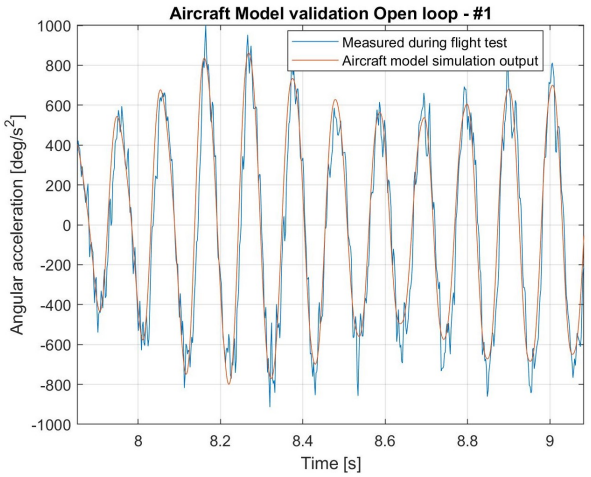


Fig. 9. Measured vs estimated angular acceleration for unstable flight condition - detail

a Simulink model which replicates the controller architecture for the Nederdrone yaw dynamics. The Simulink model includes the INDI inner loop and the proportional outer loops for rate and attitude tracking and the actuator dynamics with respective non-linear and saturation behavior. Then a linear analysis of the Simulink model is performed using MATLAB linearization routine for both stable and unstable controller configuration. The difference between the two conditions lies in the values of the low pass filter applied to the feedback signals for both attitude rate and acceleration and the values are reported in Table III.

For the stable configuration, the linearized model has no poles on the right-hand side of the complex plane. Instead, for the unstable configuration, the linearized model has a couple of unstable complex conjugate poles with a natural frequency of $52.8\,\mathrm{rad\,s^{-1}} = 8.4\,\mathrm{Hz}$. The pole-zero maps for both conditions are shown in Figures 10 and 11. When

TABLE III
CUT-OFF FREQUENCIES FOR FILTERS APPLIED TO FEEDBACK SIGNALS IN DIFFERENT CONDITIONS

| Condition | Rate $\omega_c f$ [Hz] | Acceleration $\omega_c f$ [Hz] |
|---|---|---|
| Stable | 4 | 0.5 |
| Unstable | 5 | 20 |

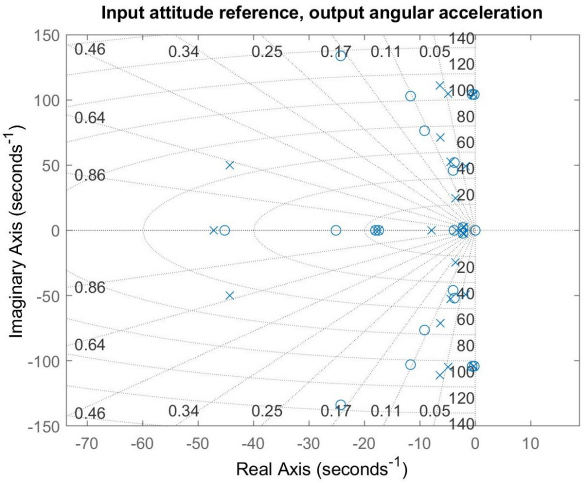


Fig. 10. Pole-zeros map for the stable controller configuration

analyzing the power spectral density function of the in-flight measured angular acceleration in Figure 12, it is clear by the peak at 9.68 Hz Hertz that the measured instability and the Simulink model's unstable pole match relatively close in frequency.

### *E. Rigid body model for angular acceleration estimation*

This model represents the rigid body rotational yaw dynamics of the Nederdrone and it aims to provide a real-time prediction of the yaw angular acceleration of the vehicle while running on the onboard computer. The model has been derived from the Euler rotation equation

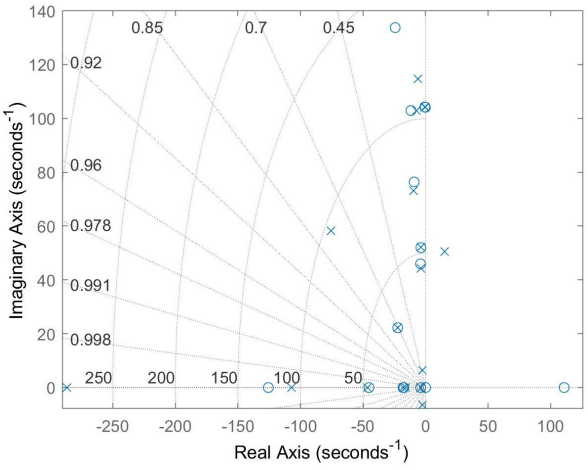


Fig. 11. Pole-zeros map for the unstable controller configuration

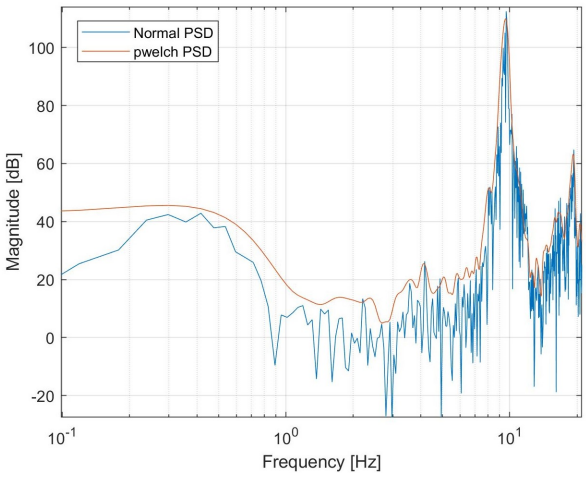


Fig. 12. Power Spectral Density function of the measured angular acceleration during unstable behaviour

of motions for the yaw axis (13). The term related to the roll and pitch rates is assumed to be negligible, leaving the yaw angular acceleration depending only on external torques contribution, which is reported in (14).

$$I_{rr}\dot{r} = -(I_{qq} - I_{pp})pq + M_r^{ext} \rightarrow I_{rr}\dot{r} = M_r^{ext} \tag{13}$$

$D(r)$ is a torque generated by the aerodynamic drag due to the yaw rate, $\tau_{D_p}(\omega_p)$ is generated by the aerodynamic drag acting on the propeller, $\tau_{I_p}(\dot{\omega}_p)$ is the torque due to the change in the propeller angular rate and $\tau_s(\delta_s)$ is generated by the control surface deflection. The aforementioned quantities are modeled as in (15) and the final formulation of the external torques $M_r^{ext}$ is provide in (16).

$$M_r^{ext} = D(r) + \tau_{D_p}(\omega_p) + \tau_{I_p}(\dot{\omega}_p) + \tau_s(\delta_s) \tag{14}$$

$$\begin{aligned} D(r) &\approx C_{D_w} r|r| \qquad \tau_{D_p}(\omega_p) \approx \hat{C}_{\tau_{D_p}} \omega_p \approx C_{\tau_{D_p}} u_r^b \\ \tau_s(\delta_s) &\approx C_{\tau_s} \delta_s \qquad \tau_{I_p}(\dot{\omega}_p) \approx \hat{C}_{\tau_{I_p}} \dot{\omega}_p \approx C_{\tau_{I_p}} \dot{u}_r^b \end{aligned} \tag{15}$$

$$M_r^{ext} = C_{D_w} r|r| + C_{\tau_{D_p}} \omega_p + C_{\tau_{I_p}} \dot{\omega}_p + C_{\tau_s} \delta_s \tag{16}$$

Therefore, by inserting (16) in (13) and solving for $\dot{r}$, the rigid body model for the yaw dynamics is obtained. The model linearly combines the input vector $[r|r|, \omega_p, \dot{\omega}_p, \delta_s]$, weighting each contribution with a scalar coefficient. The rigid body model can be reformulated as in (17), where the inertia term $I_{rr}$ has been included in the coefficients.

$$\dot{r} = [C_{D_w}, C_{\tau_{D_p}}, C_{\tau_{I_p}}, C_{\tau_s}] \cdot \begin{bmatrix} r|r|, \\ u_r^b, \\ \dot{u}_r^b, \\ \delta_s \end{bmatrix} \triangleq \vec{C} \begin{bmatrix} r|r|, \\ u_r^b, \\ \dot{u}_r^b, \\ \delta_s \end{bmatrix} \tag{17}$$

The coefficient vector $\vec{C}$ is estimated using a least-square approach. Given the linear system structure in (18), where $Y$ and $A$ are as described in (19) and (20).

$$Y = A\vec{C} \tag{18}$$

$$Y = \begin{bmatrix} \dot{r}_{exp\,1} \\ \dot{r}_{exp\,2} \\ \vdots \\ \dot{r}_{exp\,n} \end{bmatrix} \tag{19}$$

$$A = \begin{bmatrix} [r|r|, u_r^b, \dot{u}_r^b, \delta_s]_{exp\,1} \\ [r|r|, u_r^b, \dot{u}_r^b, \delta_s]_{exp\,2} \\ \vdots \\ [r|r|, u_r^b, \dot{u}_r^b, \delta_s]_{exp\,n} \end{bmatrix} \tag{20}$$

The data set utilized is a reduced version of the one used for the full model identification, using only the test numbers 1, 5, 6, and 7, to use flight test data which should not be much affected by the structural modes. The estimated coefficients are reported in Table IV. The same estimation is carried out without considering the contribution of the propeller command and the obtained coefficient is reported in Table IV. The RMSE value for the estimated coefficients is 79.06.

TABLE IV
LEAST-SQUARE MODEL COEFFICIENT VALUES

| | |
|---|---|
| $\vec{C}$ | $[-3.28\cdot10^{-2}, -6.23\cdot10^{-3}, 3.61\cdot10^{-3}, 4.934]$ |
| $\vec{C}$ with $u_r^b = 0$ | $[-3.21\cdot10^{-2}, 0, 3.68\cdot10^{-3}, 4.65]$ |

The comparison between the two estimated models for two different inputs (chirp and doublet) with respective components is shown in Figure 13 and Figure 14.

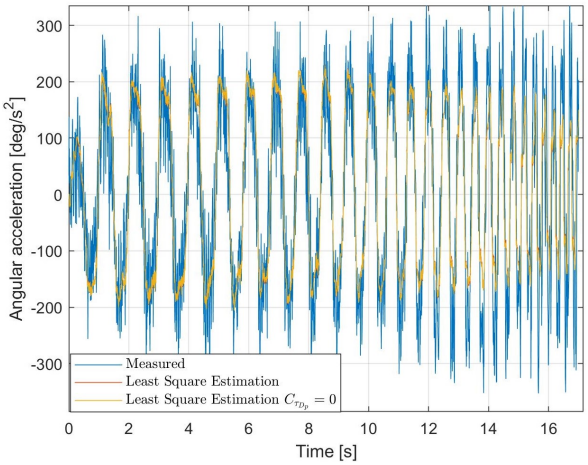


Fig. 13. Acceleration estimation via least squared estimated model for chirp input

## IV. CONTROL LAW DESIGN

The controller design must take into account the constraints due to the vehicle design. The actuator bandwidth is limited to 50 $rad/s$, the available sensors do not allow for structural state estimation and the current control allocation architecture does not allow independent control of single actuators. Therefore, the design of an active vibration suppression controller is not feasible with the current hardware. The only solution left is angular acceleration feedback-signal processing, filtering, or signal manipulation.

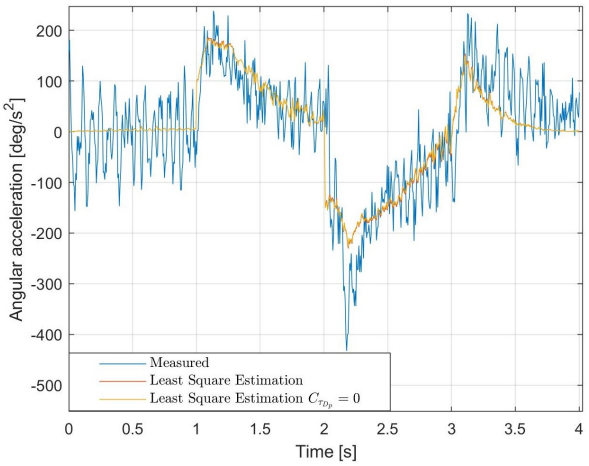


Fig. 14. Acceleration estimation via least squared estimated model for doublet input

### A. Hybrid INDI

A Hybrid INDI controller aims to mitigate the measurement delays in the angular acceleration feedback signal, by fusing the sensor's signal with a system model [11]. The angular acceleration signals fusion is operated via complementary filtering, a sensor fusion technique that weights the contribution of different sensors to state estimation. This sensor fusion technique is largely used for attitude estimation where MARG (Magnetic Angular Rate and Gravity) unit attitude estimation is combined with attitude position estimated by quaternions using the angular rate measured by the gyro unit to update the quaternion attitude estimation [17, 18]. However, it has also been used for angular acceleration estimation for flight control as proposed by Jiali et. al. in [19].

As described by Mahoney [20], frequency domain complementary filters provide a means to fuse noisy measurement or estimation of the same signal which has complementary spectral characteristics. To obtain the complementary filter, two filters $LP(s)$ and $HP(s)$ are defined as follows. $LP(s)$ is a low pass filter with a unity gain and a cut-off frequency that defines the border between the high frequency and low-frequency interval. In this case, $LP(s)$ is a second-order Butterworth filter with a cut-off frequency of 3.5 $Hz$ which was determined during the flight test. $HP(s)$ must satisfy the equation $HP(s) = 1 - LP(s)$ which makes $H(s)$ an high pass filter of the same order of the low pass filter. The complementary filter output is obtained as in (21), where $m_1$ and $m_2$ are the two signal to be fused.

$$\hat{m}(s) = m_1(s)LP(s) + m_2(s)HP(s) \tag{21}$$

In our case, the two signals are the angular acceleration measurement obtained from gyroscope measurement differentiation and angular acceleration estimation from an onboard system model. The angular acceleration measurement is fed to the low-pass filter while the angular acceleration estimation obtained by the model described in III-E is fed to the high-pass filter. Then, the fused angular acceleration signal is fed back to the INDI controller. Therefore, for the low-frequency interval, the controller still relies on sensor information, while for high-frequency information it relies on angular acceleration estimated using a rigid body model and which therefore is not affected by structural modes contributions.

For this specific design, a modification in the INDI synchronization loop is required. In the complementary filter, the delay in the feedback signal generated by the low-pass filter is compensated by the high-pass filter contribution. Therefore, the low-pass filter in the feedback of the actuator synchronization loop must be removed to avoid the actuator command having a lag with respect to the angular acceleration signal.

### B. Notch filter

The use of notch filters to not excite structural motions has been used extensively in the aerospace industry [2, 4]. In this case, the notch filter $NF(s)$ is placed in the actuator synchronization loop after the current yaw command calculation, as shown in Figure 15.

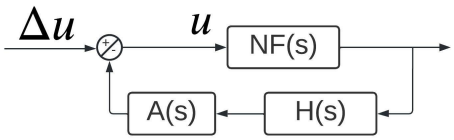


Fig. 15. Synchronization loop for the notch filter solution

The central frequency and the bandwidth of the notch filter are set respectively to 9.1 $Hz$, which is the natural frequency of the dominant fuselage torsional mode, and to 5 $Hz$. The Butterworth low-pass filter is kept both in the actuator synchronization loop and in the angular acceleration feedback loop, while the cut-off frequencies are set to 5 $Hz$. The removal of the low pass filter from the acceleration feedback loop is not possible due to the increase of the angular acceleration signal noise power with the increase in frequency. This is due to the differentiation of the gyroscope measurement, which acts as a discrete-time derivative operation.

## V. Simulation and flight test result

The two solutions proposed in sec. IV and the solution already implemented on the vehicle and described in II-B are modeled in a Simulink®environment and implemented in the *Paparazzi Autopilot* framework for their performance to be investigated.

For the flight tests, the angular acceleration is calculated via discrete differentiation of the yaw rate measurement followed by a signal filtering with a second-order Butterworth low-pass filter with a 15 $Hz$ cut-off frequency. This is done to prevent the growth of the noise's power with the increase of frequency in the angular acceleration measurement due to the discrete differentiation operation.

For all the tests investigating frequency domain behavior, at least three time-domain measurements are executed for each test type and each solution. Then, after obtaining the frequency domain data, the ones belonging to the same test type and the same investigated solution are used to obtain an averaged frequency-domain behavior.

### A. Investigated quantities

The different INDI loops are investigated under the following aspects:

1) Stability
2) INDI closed-loop behavior and transfer function
3) Reference tracking performance for outer control loops
4) Disturbance rejection capabilities

The stability of the inner-loop controller is assessed in a simulation environment via open-loop and closed-loop analyses of the different INDI solutions via model linearization and during flight tests via manual flight. Since the aircraft model used in the simulation is the one obtained in III-E, due to the frequency interval over which the flight tests excited the aircraft's dynamic, the model is considered to be valid between 1 $Hz$ and 15 $Hz$.

The INDI closed-loop behavior is investigated by adding a chirp signal to the angular acceleration reference signal during a hovering maneuver. The chirp frequency sweep starts at 0.5 $Hz$ and stops at 15 $Hz$. The closed-loop transfer function is calculated using the Fast Fourier Transform of the INDI loop input and output signals. The goal of the INDI-based controller is to linearize the input-output relation, meaning with a perfect nonlinear dynamic inversion the closed-loop can be represented by a unity gain transfer function. Therefore, the adherence of the different closed loops to the ideal behavior is discussed. The inversion residual, which is the difference between the system angular acceleration and the angular acceleration reference, is calculated and its frequency content is analyzed. The inversion residual is defined as $res_{INDI}(\omega) = \nu(j\omega) - \dot{r}_m(j\omega)$, with $\dot{r}_m(j\omega) = CL(j\omega) \cdot \dot{r}_{ref}(\omega)$ where $CL(j\omega)$ is the inner INDI closed-loop transfer function. This results in the $res_{INDI}(\omega) = (1 - CL(\omega))\nu(\omega)$. Therefore, the closer the closed-loop transfer function is to the unity gain, the lower the value of the auto power spectral density function (PSD) of the inversion residual in the frequency interval of interest.

The second test is a reference tracking task, where the drone has to follow a specific computer-generated heading

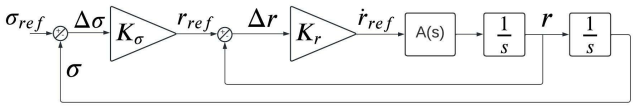


Fig. 16. Ideal model diagram

reference. Two different reference signals are defined: a chirp signal with power between 0.5 Hz and 15 Hz with an amplitude of 5° and doublet signal lasting 10 s with an amplitude of 30°. The goal is to assess the impact that each solution has on the total yaw axis control structure, both from a time and frequency domain perspective. The frequency domain behaviour is investigated by calculating the transfer function which relates the heading reference signal to the measured heading angle. The calculation procedure of the transfer function is the same as the closed-loop analysis, with the difference that no filtering is applied to the signals. Moreover, the results are compared to the ideal response, with the ideal model being the representation of the heading signal tracking dynamics if all the components of the system, including the controller and the aircraft dynamics, would have perfect behavior. The ideal model transfer function is reported in (22). The model is derived from the scheme in Figure 16, where the proportional gains $K_\sigma$=6 $K_r$=20 and the actuator transfer function $A(s)$ are the ones defined in II. The nonlinear dynamic inversion is assumed to be perfect, leaving only the actuator dynamics as a system component [9] and no signal filtering is required.

$$F_{IM}(s) = \frac{2160}{s^3 + 180s^2 + 360s + 2160} \tag{22}$$

The third and final test is a disturbance rejection test. To execute a repeatable test, the disturbance is generated by applying an offset to the $u_r$ signal sent to the control surfaces. The system's disturbance response is analyzed in terms of saturation of the propeller yaw command, time to reject the disturbance, and acceleration overshoot.

### *B. Simulation results*

The stability analysis in the simulation shows that only the standard INDI and the hybrid INDI are stable, while the notch filter solution is not. The integration of the notch filter in the INDI loop is not beneficial and induced instabilities at a different frequency with respect to the one mentioned in II-B and III-E. Different combinations of notch frequency and notch bandwidth are investigated, both in simulation and during flight tests, but none of the ones tested provided a stable solution. The poles of the INDI inner-loop of the notch filter solution Simulink model are shown in Figure 17 and the frequency content of the angular acceleration measured during the flight test executed using the notch filter solution is shown in Figure 18.

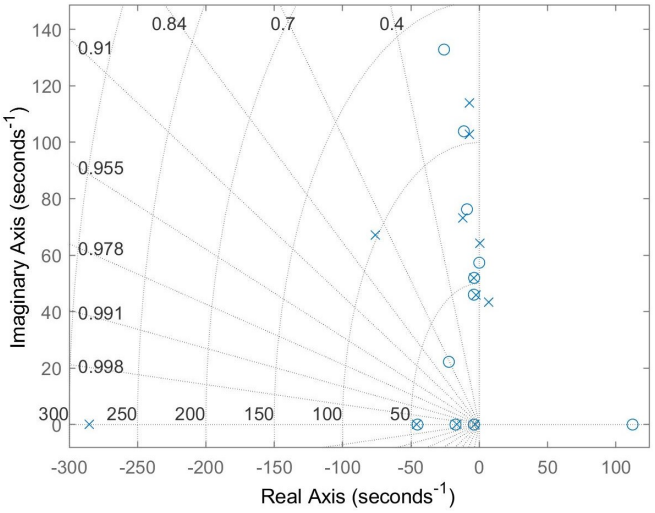


Fig. 17. Pole-zero map of INDI closed loop augmented with notch filter Simulink model

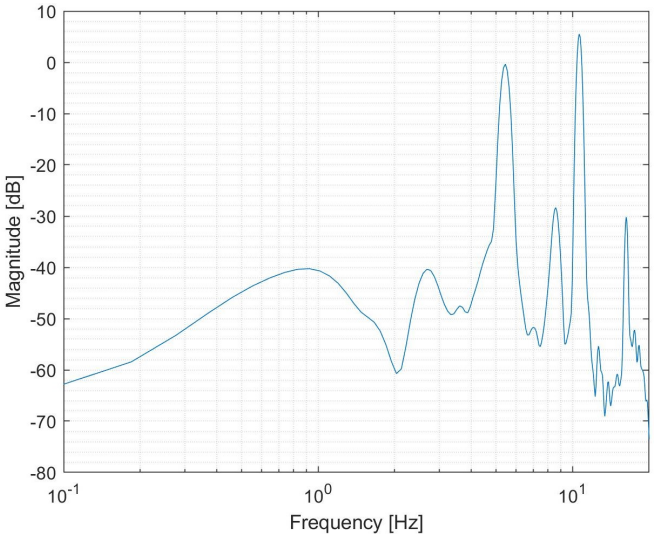


Fig. 18. Frequency content of angular acceleration signal during notch filter solution flight test

There are multiple causes for the instability of the notch filter solution. One can be found in the extra lag the notch filter introduces on the actuator command signal for the yaw dynamics $u_r$ before the notch frequency. Moreover, the open loop transfer function has a magnitude above 0 dB after the notch frequency where the phase margin is negative. The open-loop transfer function phase margin of the same solution without the notch filter is not enough to compensate for the additional delay, obtaining an open-loop transfer function with a negative phase margin, which leads to an unstable closed-loop system, as shown in Figure 19.

Therefore, the notch filter solution does not achieve the goal of enhancing the INDI-based flight control system for

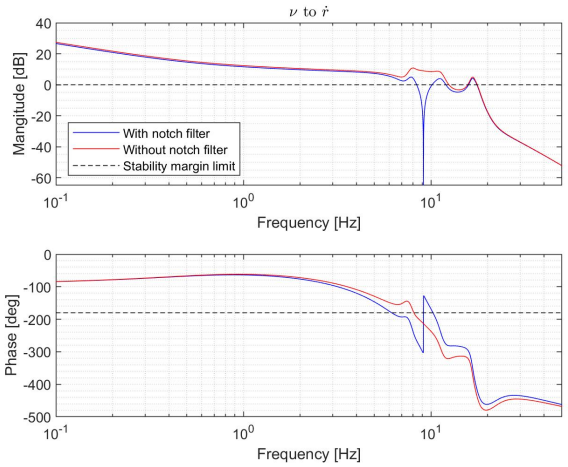


Fig. 19. Open loop transfer function for INDI loop with and without notch filter

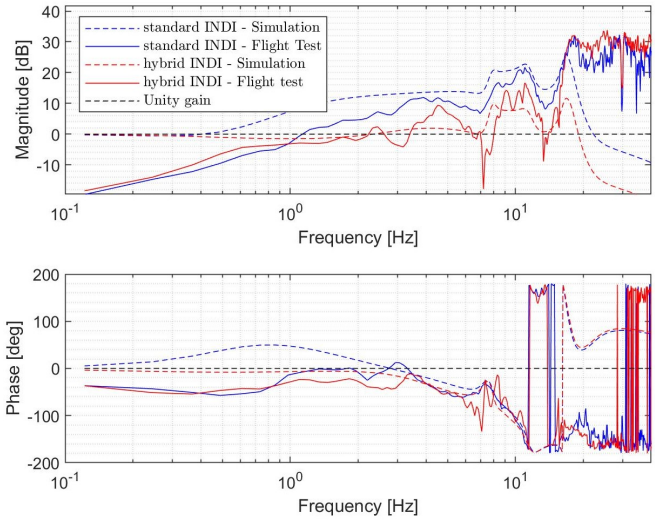


Fig. 20. INDI-inner loop transfer function from simulation and flight test data

this drone, despite being one of the benchmark solutions in the aerospace industry. The performance of this solution was not further investigated since stability is not achieved.

### C. Flight test results

The closed-loop transfer functions estimated in the flight test (solid line) and obtained by simulation model linearization (dashed line) are shown in Figure 20.

In the magnitude plot (top), it is clear that the hybrid INDI solution has a lower magnitude over the frequency interval dominated by the structural modes [3 - 15] $Hz$. This is valid for the data from both simulation and flight tests. Moreover, the magnitude of the hybrid INDI solution is closer to the 0 dB line than the other solution, making it the closest solution to the ideal unity gain behavior. In the phase plot, the behavior of the two solutions is almost identical, aside from a small portion of the validity bandwidth (1 - 2.5 Hz), where the standard INDI solution provides less phase lag.

The considerations outlined above are summarized in Figure 21, where the power spectral density function of the inversion residual is displayed. It is clear that for most of the interval of interest the hybrid INDI solution has a lower power, which indicates a better inversion performance and lower power over the controller bandwidth for the angular acceleration control loop. A better inversion performance from the frequency domain point of view means that the signal at specific frequencies is followed with more precision, or with a smaller error, using the complementary filter-based solution instead of the standard INDI solution. This metric provides a more compact outline of how close to the unity gain is the closed-loop transfer function since it incorporates the magnitude and phase mismatches between the pseudo control signal and the measured acceleration. Therefore, the closer the closed-loop transfer function is to the unity gain, the lower the value of the auto PSD of the inversion residual.

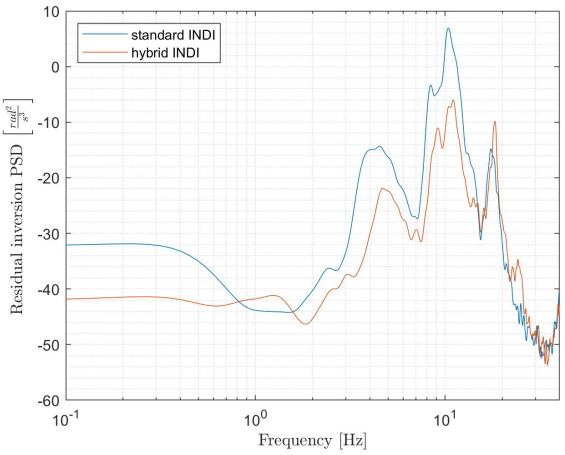


Fig. 21. Flight test inversion residual comparison

Figures 22 and Figure 23 show the behaviour of both solution during the heading tracking task. The first figure shows the frequency domain behaviour, where it is clear that both the implemented INDI solutions are not matching the ideal system's behaviour. Specifically, they show a significant lag compared to the ideal system, as it is clear from Figure 23, representing the time domain behaviour.

This is mainly due to the low-pass filtering of the yaw angular rate and the restriction in the yaw command authority operated during the real-time control allocation. The control allocation strategy reduces the magnitude of yaw command $u_r$ executed by the propellers, reducing its effectiveness and decreasing the gain of the closed-loop transfer function.

The small difference in the time and frequency domain behavior between the two investigated solutions suggests

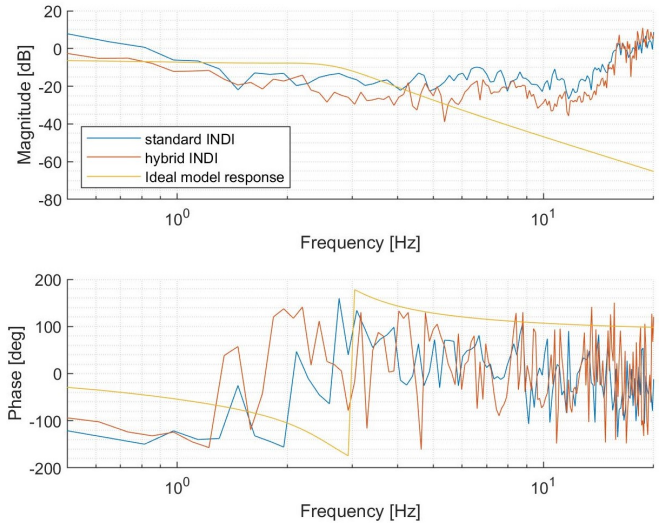


Fig. 22. Frequency domain comparison of yaw/heading angle controller and ideal model

that the way they affect the behavior of the outer control loop is not much different. Moreover, the outcome of this flight test does not allow us to identify the better solution among the investigated ones.

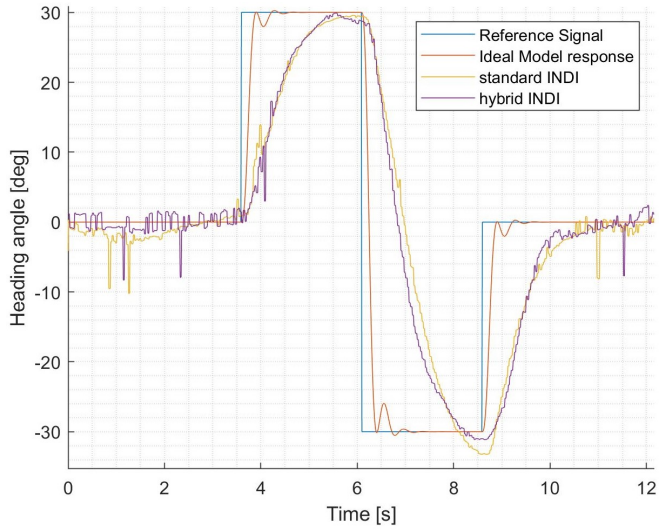


Fig. 23. Time domain comparison of yaw/heading angle controller and ideal model

Finally, the disturbance rejection test results for the standard INDI solution and the hybrid INDI solution are respectively shown in Figure 24 and Figure 25. In each figure, two different sets of quantities are shown: the first set is constituted by the pseudo-control signal, the feedback signal, and the measured angular acceleration signal. The second set includes the disturbance command, the yaw angular acceleration command calculated by the INDI controller, and the command received from the propeller and the control surfaces. The areas of the graphs with a green background mark the time intervals when the disturbance is active.

In this test, there are some points of interest worth mentioning: the feedback signal behavior during and after the disturbance, which is the main difference between the two solutions. The control distribution of the disturbance rejection effort between the propellers and the control surfaces, and quickness in recovering the disturbance effect.

The disturbance is provided with the control surfaces and it is expected that, after the controller action, the control surfaces' position is closer to zero, while the propeller contribution increases to compensate for the disturbance in the opposite direction. Both the investigated solutions present the expected time-domain behavior for what concerns the actuator command quantities. In the upper graph of each figure, an increase in angular acceleration is expected after the activation of the disturbance, followed by a rapid drop of the same quantity due to the controller action. Moreover, once the controller compensates for the disturbance, the angular acceleration feedback signal should settle again around the zero value.

The standard solution is the fastest to compensate for the effects of the change in presence of the disturbance. Since the angular acceleration feedback signal is very slow in following the change in acceleration, the difference between the pseudo control and the feedback signal grows rapidly and the disturbance is quickly compensated. The hybrid INDI solution is slower than the standard solution since the feedback signal remains more adherent to the pseudo control signal, keeping the angular acceleration error to a lower magnitude and therefore the magnitude of the yaw axis actuator command $u_r$ lower.

The hybrid INDI solution shows to have slightly better performance than the current solution implemented on the Nederdrone concerning the closed-loop performance and the accuracy of the nonlinear inversion. For what concerns attitude angle tracking and disturbance rejection, the performance of the two aforementioned solutions are comparable and no clear improvement from the standard INDI solution can be pointed out. The notch filter solution did not manage to stabilize the system.

## VI. Conclusions

This paper investigated the interaction of an INDI-based flight control system with the structural dynamics of a slender and light unmanned flying vehicle, which affected the yaw dynamics during the hover maneuver. The different investigated versions of the INDI control loop take into account the limitations of the drone in terms of real-time state estimation capabilities, actuator bandwidth, and the current solution implemented in the drone. The first solution is based on a complementary filter and it is designed to provide the benefit of sensor-based and model-based control systems. A notch filter-based

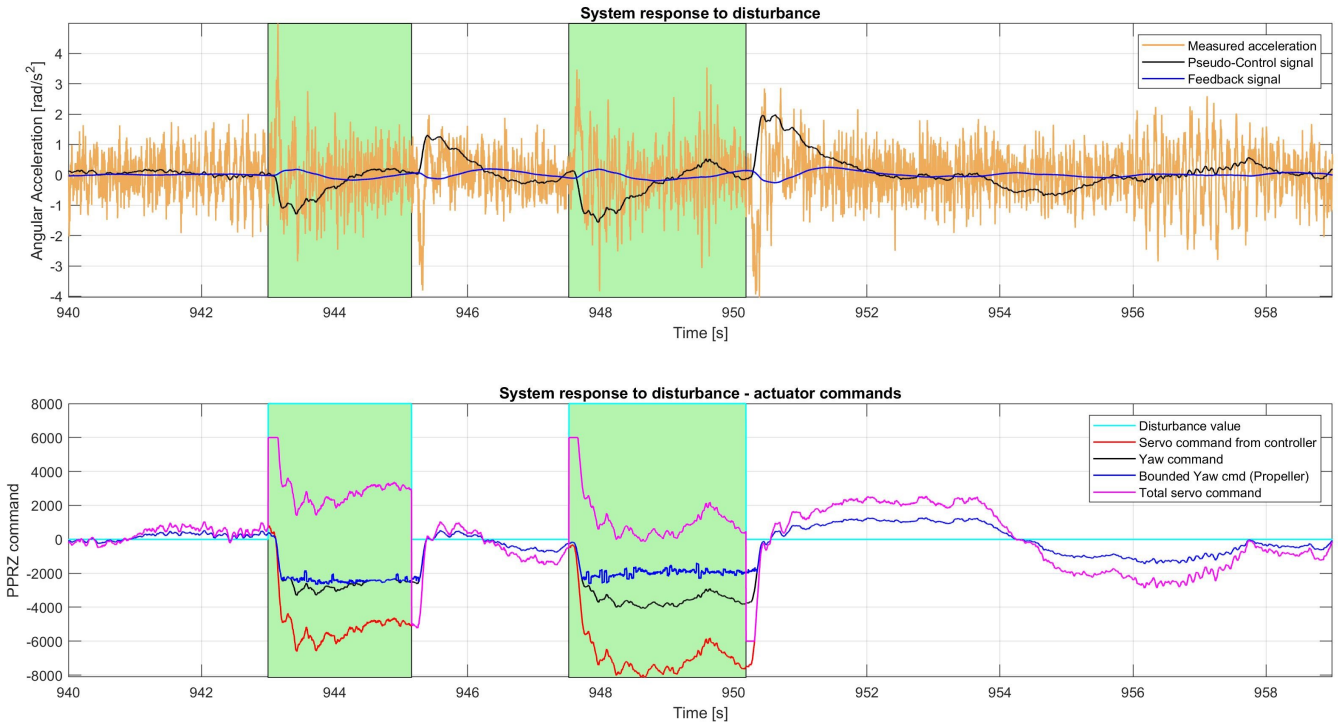


Fig. 24. Time domain behaviour for standard INDI solution disturbance test

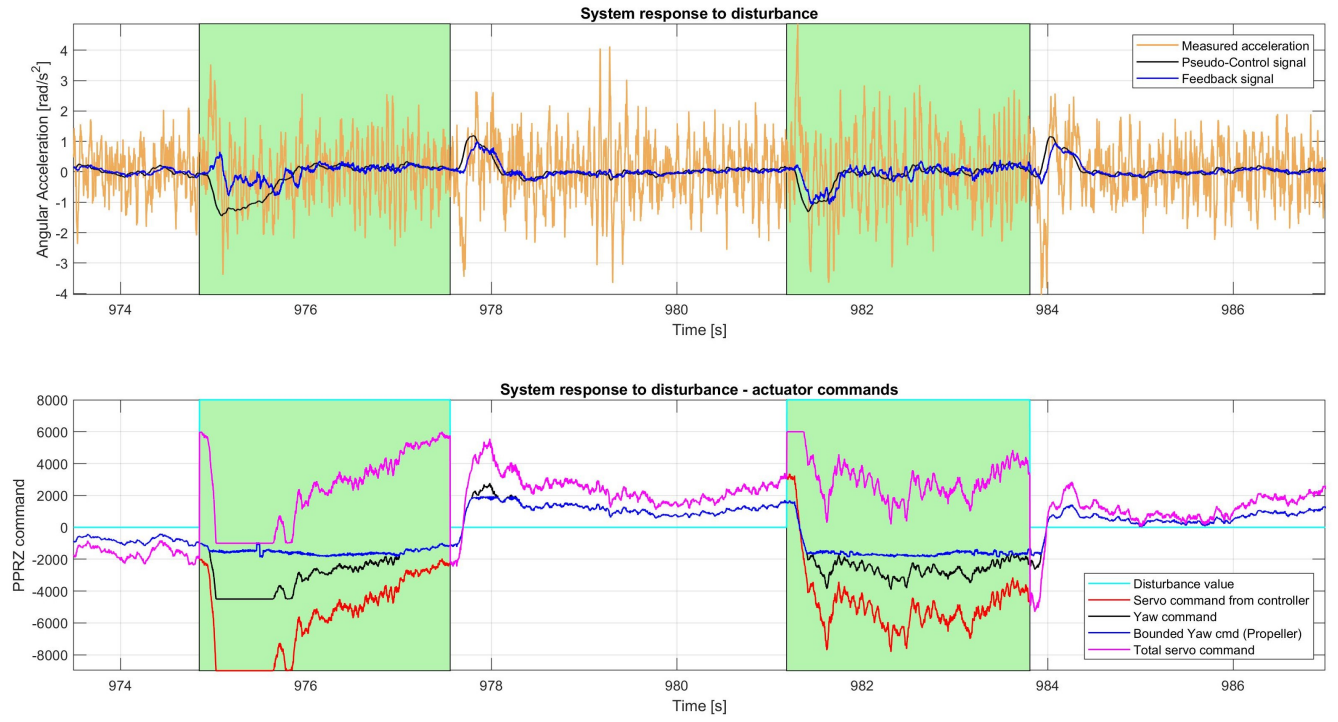


Fig. 25. Time domain behaviour for hybrid INDI solution disturbance test

solution was developed to be compared to the current and the first INDI solutions.

A simulation model and controller parameters were derived from different tests, namely flight tests and ground vibration tests. Afterwards, the three investigated solutions were implemented for both the simulation environment and the real drone to determine each solution's stability property and performance. The INDI closed-loop performance, the nonlinear dynamic inversion accuracy, the effect on the total yaw controller structure, and the disturbance rejection performance of each solution were assessed.

The hybrid INDI solution brings some improvement to the currently standard INDI solution such as lower excitation of the structural modes and an increase to the cut-off frequency of the angular acceleration low-pass filter by almost half a decade, due to the lead in phase provided by the high-frequency component of the complementary filter. Rejection of unmodeled disturbances is successfully obtained by both stable solutions. The "high-frequency" contribution of the structural modes that made the sole sensor-based solution unstable for high low-pass filter cut-off frequency is compensated by the assumed rigid body model "high-frequency".

Therefore, from the results obtained in the flight test, we can say that the hybrid-INDI solution is a valid alternative to the benchmark solution. Moreover, even though the hybrid version of the INDI controller requires the identification of a dynamic model, the chosen model is very simple and does not require high accuracy, since the controller is only partially dependent on it. Furthermore, the high-frequency component of the measured angular acceleration, which contains structural mode contribution, is substituted by the assumed behaviour of the rigid body mode only. Thus, the controller based on the hybrid-INDI not only is not reacting to the low power contribution of the structural modes at high frequency but is instead contributing to the pseudo-control signal tracking by the rigid body mode. Overall, the proposed solution brings some improvement to the standard INDI solution but it does not distance itself from it in terms of performance.

Interesting continuations for this research could be the identification of a more accurate system model to calculate the rigid body's angular acceleration to be fed to the high-pass filter of the complementary filter, for what concerns the system identification field. Different angular acceleration estimation techniques could be implemented to generate a more accurate signal to feedback to the controller. Finally, active structural vibration suppression using an INDI-based controller could be considered a research topic after solving the actuator authority issues.

## References


[1] S. Malisani, E. Capello, and G. Guglieri. "Development of a Flight Mechanics Simulation Computer based on a Flexible Aircraft Model for a Regional Aircraft". In: *IOP Conference Series: Materials Science and Engineering* 1024 (2021), p. 012066. DOI: 10.1088/1757-899x/1024/1/012066.

[2] J. Becker, B. Caldwell, and V. Vaccaro. "*The interaction of flight control system and aircraft structure / Structural Aspects of Flexible Aircraft Control*". In: (2014).

[3] H. Yamashiro, R. Stirling, and P. Engineer. "*Reduction of Flight Control System/Structural Mode Interaction*". In: August (2007), pp. 1–19. DOI: 10.2514/6.2007-6381.

[4] Flávio J. Silvestre et al. "*Aircraft control based on flexible aircraft dynamics*". In: *Journal of Aircraft* 54.1 (2017), pp. 262–271. DOI: 10.2514/1.C033834.

[5] Wei Xu et al. "*Full Attitude Control of an Efficient Quadrotor Tail-sitter VTOL UAV with Flexible Modes*". In: *International Conference on Unmanned Aircraft Systems (ICUAS)* (2019).

[6] X. Wang et al. "*Flexible aircraft gust load alleviation with incremental nonlinear dynamic inversion*". In: *Journal of Guidance, Control, and Dynamics* 42.7 (2019), pp. 1519–1536. DOI: 10.2514/1.G003980.

[7] E.J.J. Smeur, G.C.H.E. De Croon, and Q. Chu. "*Gust disturbance alleviation with incremental nonlinear dynamic inversion*". In: *IEEE International Conference on Intelligent Robots and Systems* 2016-Novem (2016), pp. 5626–5631. DOI: 10.1109/IROS.2016.7759827.

[8] E. Mooij. "*Robust control of a conventional aeroelastic launch vehicle*". In: *AIAA Scitech 2020 Forum* 1 - Part F, Orlando - FL, United States.January (2020), pp. 1–25. DOI: 10.2514/6.2020-1103.

[9] E.J.J. Smeur, Q. Chu, and G.C.H.E. de Croon. "*Adaptive Incremental Nonlinear Dynamic Inversion for Attitude Control of Micro Air Vehicles*". In: *Journal of Guidance, Control, and Dynamics* 39.3 (2016). DOI: 10.2514/1.G001490.

[10] C. De Wagter et al. "*The NederDrone: A hybrid lift, hybrid energy hydrogen UAV*". In: *International Journal of Hydrogen Energy* 46.29 (2021), pp. 16003–16018. DOI: 10.1016/j.ijhydene.2021.02.053.

[11] Yagiz Kumtepe, Tijmen Pollack, and Erik-Jan Van Kampen. "Flight Control Law Design using Hybrid Incremental Nonlinear Dynamic Inversion". In: (). DOI: 10.2514/6.2022-1597. eprint: https://arc.aiaa.org/doi/pdf/10.2514/6.2022-1597. URL: https://arc.aiaa.org/doi/abs/10.2514/6.2022-1597.

[12] *Servo actuator specifications*. https://www.servocity.com/hs-5086wp-servo/. Accessed: 2022-02-22.

[13] F. Grondman et al. "*Design and flight testing of incremental nonlinear dynamic inversion based control laws for a passenger aircraft*". In: *AIAA Guidance, Navigation, and Control Conference, 2018* 0.210039 (2018). DOI: 10.2514/6.2018-0385.

[14] *Paparazzi Autopilot*. https://wiki.paparazziuav.org/wiki/Main_Page.

[15] Z. Drmač, S. Gugercin, and C. Beattie. "Quadrature-Based Vector Fitting for Discretized $H_2$ Approximation". In: *SIAM Journal on Scientific Computing* 37.2 (2015), A625–A652. DOI: 10.1137/140961511.

[16] Mark B. Tischler and Robert K. Remple. *Aircraft and Rotorcraft System Identification - Engineering methods with Flight Test Examples*. 1801 Alexander Bell Drive, Reston, VA 20191-4344: American institute of Aeronautics and Astronautics, 2012. ISBN: 978-1-60086-820-7.

[17] Md. Saiful Islam et al. "A low cost MEMS and complementary filter based attitude heading reference system (AHRS) for low speed aircraft". In: *2016 3rd International Conference on Electrical Engineering and Information Communication Technology (ICEEICT)*. 2016, pp. 1–5. DOI: 10.1109/CEEICT.2016.7873047.

[18] Zhang Zhe et al. "Adaptive Complementary Filtering Algorithm for IMU Based on MEMS". In: *2020 Chinese Control And Decision Conference (CCDC)*. 2020, pp. 5409–5416. DOI: 10.1109/CCDC49329.2020.9164809.

[19] Yang Jiali and Zhu Jihong. "An angular acceleration estimation method based on the complementary filter theory". In: *Conference Record - IEEE Instrumentation and Measurement Technology Conference* 2016-July (2016). ISSN: 10915281. DOI: 10.1109/I2MTC.2016.7520548.

[20] Robert Mahony et al. "Nonlinear complementary filters on the special linear group". In: *International Journal of Control* 85.10 (2012), pp. 1557–1573. ISSN: 00207179. DOI: 10.1080/00207179.2012.693951.

[21] X. Wang et al. "*Stability analysis for incremental nonlinear dynamic inversion control*". In: *Journal of Guidance, Control, and Dynamics* 42.5 (2019), pp. 1116–1129. DOI: 10.2514/1.G003791.

## APPENDIX A
## INCREMENTAL NONLINEAR DYNAMICS INVERSION DERIVATION

Nonlinear dynamics inversion flight control system design strategies aim to linearize nonlinear dynamics to later design a linear controller to obtain the desired system behaviour. This goal is reached by calculating the required input to give to the system to obtain the desired output by inverting the system's dynamics equations. Incremental nonlinear dynamics inversion belongs to this family of controllers but is regarded as a sensor-based control strategy since it gathers the system's state knowledge with sensor measurements. Given a nonlinear SISO system, where $\vec{f}(\vec{x})$, $\vec{g}(\vec{x})$ and $h(\vec{x})$ are arbitrary nonlinear functions.

$$\begin{aligned} \dot{\vec{x}} &= \vec{f}(\vec{x}) + \vec{g}(\vec{x})\,u \\ y &= h(\vec{x}) \end{aligned} \tag{23}$$

The relative degree $r$ of the system in (23) is defined as the minimum number of time differentiation required to be operated on the output $y$ to obtain an explicit relation between input $u$ and output. For partial and fully controllable system of degree $n$, the relation $r \leq n$ holds. If $r < n$ then there are $n - r$ hidden or internal dynamics. Then, the following change of coordinates is defined

$$\begin{aligned} \phi_1(\vec{x}) &= h(\vec{x}) \\ \phi_2(\vec{x}) &= L_f\, h(\vec{x}) \\ &\vdots \\ \phi_r(\vec{x}) &= L_f^{r-1}\, h(\vec{x}) \end{aligned} \tag{24}$$

Where $L_f^m\, h(\vec{x})$ is the $m^{th}$ Lie derivative of $h(\vec{x})$, which is defined as in (25)

$$\begin{aligned} L_f^0\, h(\vec{x}) &= h(\vec{x}) \\ L_f^k\, h(\vec{x}) &= L_f \left[L_f^{k-1} h(\vec{x})\right] = \nabla^T \left[L_f^{k-1} h(\vec{x})\right] \vec{f}(\vec{x}) \\ L_g L_f\, h(\vec{x}) &= \nabla^T \left[L_f h(\vec{x})\right] \vec{g}(\vec{x}) \end{aligned} \tag{25}$$

It is always possible to add $n - r$ functions $\phi_i(\vec{x})$ such as $L_g\, \phi_i(\vec{x}) = 0\ \forall\ r+1 \leqslant i \leqslant n$ to complete the coordinate transformation in (24) and have a system of the same degree of the initial one.

$$\vec{z} = \vec{\Phi}(\vec{x}) = \begin{bmatrix} \phi_1(\vec{x}) \\ \vdots \\ \phi_r(\vec{x}) \\ \phi_{r+1}(\vec{x}) \\ \vdots \\ \phi_n(\vec{x}) \end{bmatrix} \tag{26}$$

When operating the time derivative to $\vec{z}$, the time derivative of the first $r-1$ coordinates are:

$$\dot{z}_i = \dot{\phi}_i(\vec{x}) = \frac{\partial \phi_i(\vec{x})}{\partial \vec{x}}\dot{\vec{x}} = \frac{\partial \phi_i(\vec{x})}{\partial \vec{x}}\left[\vec{f}(\vec{x}) + \vec{g}(\vec{x})u\right] = \frac{\partial L_f^{i-1}h(\vec{x})}{\partial \vec{x}}\vec{f}(\vec{x}) = L_f^i h(\vec{x}) = \phi(\vec{x}) = z_{i+1} \tag{27}$$

The $r^{th}$ coordinate time derivative is:

$$\dot{z}_r = \dot{\phi}_r(\vec{x}) = \frac{\partial \phi_r(\vec{x})}{\partial \vec{x}}\dot{\vec{x}} = \frac{\partial \phi_r(\vec{x})}{\partial \vec{x}}\left[\vec{f}(\vec{x}) + \vec{g}(\vec{x})u\right] = \frac{\partial L_f^{r-1}h(\vec{x})}{\partial \vec{x}}\vec{f}(\vec{x}) + \frac{\partial L_f^{r-1}h(\vec{x})}{\partial \vec{x}}\vec{g}(\vec{x})u = L_f^r h(\vec{x}) + L_g L_f^{r-1}h(\vec{x})u \tag{28}$$

Finally, the last $n-r$ elements describing the internal dynamics are reported in (29), with $i \in [r+1, n]$.

$$\dot{z}_i = L_f \phi_i(\vec{x}) + L_g \phi_i(\vec{x})u = q_{i-r}(\vec{x}) \tag{29}$$

As said before, in the above equation the Lie derivative of $q_{i-r}(\vec{x}) = 0$ along $\vec{g}(\vec{x})$ is equal to zero. In order to conclude the coordinate transformation, the dependency of (26) and (27) on $\vec{x}$ has to be substituted with $\vec{x} = \vec{\Phi}^{-1}(\vec{z})$, thus (28) becomes

$$\dot{z}_r = L_f^r h\left[\vec{\Phi}^{-1}(\vec{z})\right] + L_g L_f^{r-1} h\left[\vec{\Phi}^{-1}(\vec{z})\right] u = a(\vec{z}) + b(\vec{z})u$$
$$a(\vec{z}) = L_f^r h\left[\vec{\Phi}^{-1}(\vec{z})\right] \qquad b(\vec{z}) = L_g L_f^{r-1} h\left[\vec{\Phi}^{-1}(\vec{z})\right] \tag{30}$$

For the internal dynamics coordinates the substitution is trivial and not useful for control system design and will not be discussed further. The system dynamics described in (30), is linearized around the current system state and input values $z = z_0$ and $u = u_0$ using a first-order Taylor approximation. Then the zero-order term $\dot{z}_r^{(0)}$ is assumed to be known from sensor measurements and the first order term related to the system's state change is neglected according to the time-scale separation principle [9].

$$\dot{z}_r \approx \dot{z}_r^{(0)} + \left.\frac{\partial[\vec{a}(\vec{z}) + b(\vec{z})]}{\partial \vec{z}}\right|_{\substack{\vec{z}=\vec{z}_0 \\ u=u_0}} \Delta\vec{z} + \left.\frac{\partial[\vec{a}(\vec{z}) + B(\vec{z})]}{\partial u}\right|_{\substack{\vec{z}=\vec{z}_0 \\ u=u_0}} \Delta u + \mathcal{O}(\Delta\vec{z}^2, \Delta u^2) \tag{31}$$
$$\dot{z}_r \approx \dot{z}_r^{(0)} + \left.\frac{\partial[\vec{a}(\vec{z}) + B(\vec{z})]}{\partial u}\right|_{\substack{\vec{z}=\vec{z}_0 \\ u=u_0}} \Delta u + \delta(\Delta\vec{z}^2, \Delta u^2, \Delta t)$$

The INDI controller is designed by solving (31) for $\Delta u$ and substituting the state derivative $\dot{z}_r = \nu$ with the desired state derivative value $\nu$. The obtained control law is reported in (32).

$$\Delta u = B^{-1}\left[\nu - \dot{z}_r^{(0)}\right] \qquad B = \left.\frac{\partial[\vec{a}(\vec{z}) + B(\vec{z})]}{\partial u}\right|_{\substack{\vec{z}=\vec{z}_0 \\ u=u_0}} \Delta u \tag{32}$$

Equation (32) calculates the value of the increment to apply to each current actuator state value. Therefore, a measurement or an estimation of the current actuator position is necessary to provide the correct input to the actuators and to avoid their saturation [13]. To fulfill this requirement, an actuator synchronization loop is usually implemented and placed between the INDI controller and the actuator. Moreover, since the state derivative measurement is used, it is also necessary to make sure the commanded actuator position and the measured state derivative belong to the same time instant. Therefore, possible low pass filters applied to the measurement signal must be applied to the actuator signal too, to ensure time synchronization.

This control strategy can be easily extended to MIMO systems. Starting from the equivalent of (23) and augmenting the number of inputs and outputs

$$\begin{aligned} \dot{\vec{x}} &= \vec{f}(\vec{x}) + G(\vec{x})\vec{u} \\ \vec{y} &= \vec{h}(\vec{x}) \end{aligned} \tag{33}$$

Where $G(\vec{x})$, $\vec{u}$ and $\vec{h}(\vec{x})$ are expressed as in (34) with $\ell$ being the number of inputs and $m$ the number of outputs.

$$\begin{aligned} \vec{h}(\vec{x}) &= [h_1(\vec{x}), h_2(\vec{x}), ..., h_i(\vec{x}), ..., h_m(\vec{x})]^T \\ \vec{u} &= [u_1(\vec{x}), u_2(\vec{x}), ..., u_j(\vec{x}), ..., u_\ell(\vec{x})]^T \\ G(\vec{x}) &= [\vec{g}_1(\vec{x}), \vec{g}_2(\vec{x}), ..., \vec{g}_j(\vec{x}), ..., \vec{g}_\ell(\vec{x})] \end{aligned} \tag{34}$$

For each output variable, the respective relative degree can be defined as previously done for the SISO case. Thus, a relative degree vector is defined as $\vec{r} = [r_1, r_2, ..., r_i, ..., r_m]^T$ and a set of coordinates can be defined to express each inputs in the canonical form. Similar to the SISO case, we can define the $r_i^{th}$ Lie derivative for the $i^{th}$ output as components of the new coordinate system

$$\begin{aligned} \phi_{r_i}^i(\vec{x}) &= L_f^{r_i} h_i(\vec{x}) \\ \dot{\phi}_{r_i}^i(\vec{x}) &= L_f^{r_i} h_i(\vec{x}) + \sum_{j=1}^{m} L_{g_j} L_f^{r_i - 1} h_i(\vec{x}) u_j \end{aligned} \tag{35}$$

Collecting all $\nu^i = \dot{\phi}_{r_i}^i$ into the vector $\vec{\Psi}(\vec{x})$, the vector of the desired change in behaviour for each output is obtained as in (36)

$$\vec{\nu}(\vec{x}) = \vec{\Psi}(\vec{x}) = \begin{bmatrix} \dot{\phi}_{r_i}^1(\vec{x}) \\ \dot{\phi}_{r_2}^2(\vec{x}) \\ \vdots \\ \dot{\phi}_{r_m}^m(\vec{x}) \end{bmatrix} = \begin{bmatrix} L_f^{r_i} h_1(\vec{x}) \\ L_f^2 h_2(\vec{x}) \\ \vdots \\ L_f^{r_m} h_m(\vec{x}) \end{bmatrix} + \tag{36}$$

$$\begin{bmatrix} L_{g_1}L_f^{r_1-1}h_1(\vec{x}) & L_{g_2}L_f^{r_1-1}h_1(\vec{x}) & \cdots & L_{g_\ell}L_f^{r-1}h_1(\vec{x}) \\ L_{g_1}L_f^{r_2-1}h_2(\vec{x}) & L_{g_2}L_f^{r_2-1}h_2(\vec{x}) & \cdots & L_{g_\ell}L_f^{r_2-1}h_2(\vec{x}) \\ \vdots & \vdots & \vdots & \vdots \\ L_{g_1}L_f^{r_m-1}h_m(v) & L_{g_2}L_f^{r_m-1}h_m(\vec{x}) & \cdots & L_{g_\ell}L_f^{r_m-1}h_m(\vec{x}) \end{bmatrix} \vec{u}$$

$$\vec{\Psi}(\vec{x}) = \vec{a}(\vec{x}) + B(\vec{x})\,\vec{u} \tag{37}$$

Thus, to simplify the input-output linearization method and to reduce the dependency of the method on the model used to design it, the first-order Taylor approximation of the equation as reported in (38).

$$\vec{\Psi} \approx \vec{\Psi}_0 + \left.\frac{\partial[\vec{a}(\vec{x}) + B(\vec{x})]}{\partial\vec{x}}\right|_{\substack{\vec{x}=\vec{x}_0 \\ \vec{u}=\vec{u}_0}} \Delta\vec{x} + \left.\frac{\partial[\vec{a}(\vec{x}) + B(\vec{x})]}{\partial\vec{u}}\right|_{\substack{\vec{x}=\vec{x}_0 \\ \vec{u}=\vec{u}_0}} \Delta\vec{u} + \\ + \mathcal{O}(\Delta\vec{x}^2, \Delta\vec{u}^2) \tag{38}$$

After due simplifications and terms grouping, (38) can be expressed as in (39). There, the terms related to the state vector derivative and increment are neglected and included in the calculation error (Wang *et al.*2019, [21]).

$$\vec{\Psi} \approx \vec{\Psi}_0 + B(\vec{x}_0)\Delta\vec{u} + \vec{\delta}(\Delta\vec{x}^2, \Delta\vec{u}^2, \Delta t)$$
$$\vec{\delta}(\Delta\vec{x}^2, \Delta\vec{u}^2, \Delta t) = \left.\frac{\partial[\vec{a}(\vec{x}) + B(\vec{x})]}{\partial\vec{x}}\right|_{\substack{\vec{x}=\vec{x}_0 \\ \vec{u}=\vec{u}_0}} \Delta\vec{x} + \mathcal{O}(\Delta\vec{x}^2, \Delta\vec{u}^2) \tag{39}$$

Where $\vec{\Psi}_0$ is assumed to be measurable, $\Delta u$ is the increment to be added to the actuator command, $\vec{x}_0$ and $\vec{u}_0$ are the state values and actuator position values at the instant $t = t_0$, which are assumed to be measurable. $B(\vec{x}_0)$ is the control effectiveness matrix evaluated at the instant $t = t_0$ and $\vec{\delta}(\Delta\vec{x}^2, \Delta\vec{u}^2, \delta t)$ is the error committed by using the first order Taylor approximation. By making explicit the actuator command increment in (39) and defining $\vec{\Psi} = \vec{\nu}$

$$\Delta\vec{u} = B^{-1}(\vec{x}_0)[\vec{\nu} - \vec{\Psi}_0] \tag{40}$$

Which if substituted in (39) provides the input-output linearization for the linearized model. In the actuator command increment calculation (40), $\vec{\delta}$ is neglected. It must be kept in mind that even if the nonlinear plant model is linearized in (38), the coefficients of the linearization, only $B(\vec{x}_0)$ in our case, can still show a nonlinear behavior. Moreover, the total control input is obtained through the sum of the previous actuator state and the currently calculated increment

$$\vec{u} = \vec{u}_0 + \Delta\vec{u} = \vec{u}_0 + B^{-1}(\vec{x}_0)[\vec{\nu} - \vec{\Phi}_0] \tag{41}$$

From (40) it is also clear that the elements of the vector $\vec{\nu}$ can be assigned with independent values, allowing the decoupling of the control axis. This property is obtained by the inversion of the control effectiveness matrix.

## APPENDIX B
## GROUND VIBRATION TEST SET UP

The ground vibration test setup was the one shown in Figure 27 and schematically described in the paper. The drone was hanged with a rope to a solid structure and connected to the shaker and the impedance head using hot glue, as reporter in Figure 26.

Before executing each vibration test, the grid of measurement point is defined from the data acquisition software, and and example is provided in Figure 28

After the data acquisition and data analysis procedures, different structural modes were identified. However, the relevant ones were only two, which shapes are reported in Figures 29 and 30. In both Figures there is an area highlighted in green which indicates the position of the autopilot device which contains the gyroscope unit.

Finally, the correlation between all the structural modes was calculated and the values are reported in table V. The columns The column and row marked as *Mode 3* correspond to the mode shape in Figure 30 and the column and row marked as *Mode 3* correspond to the mode shape in Figure 30

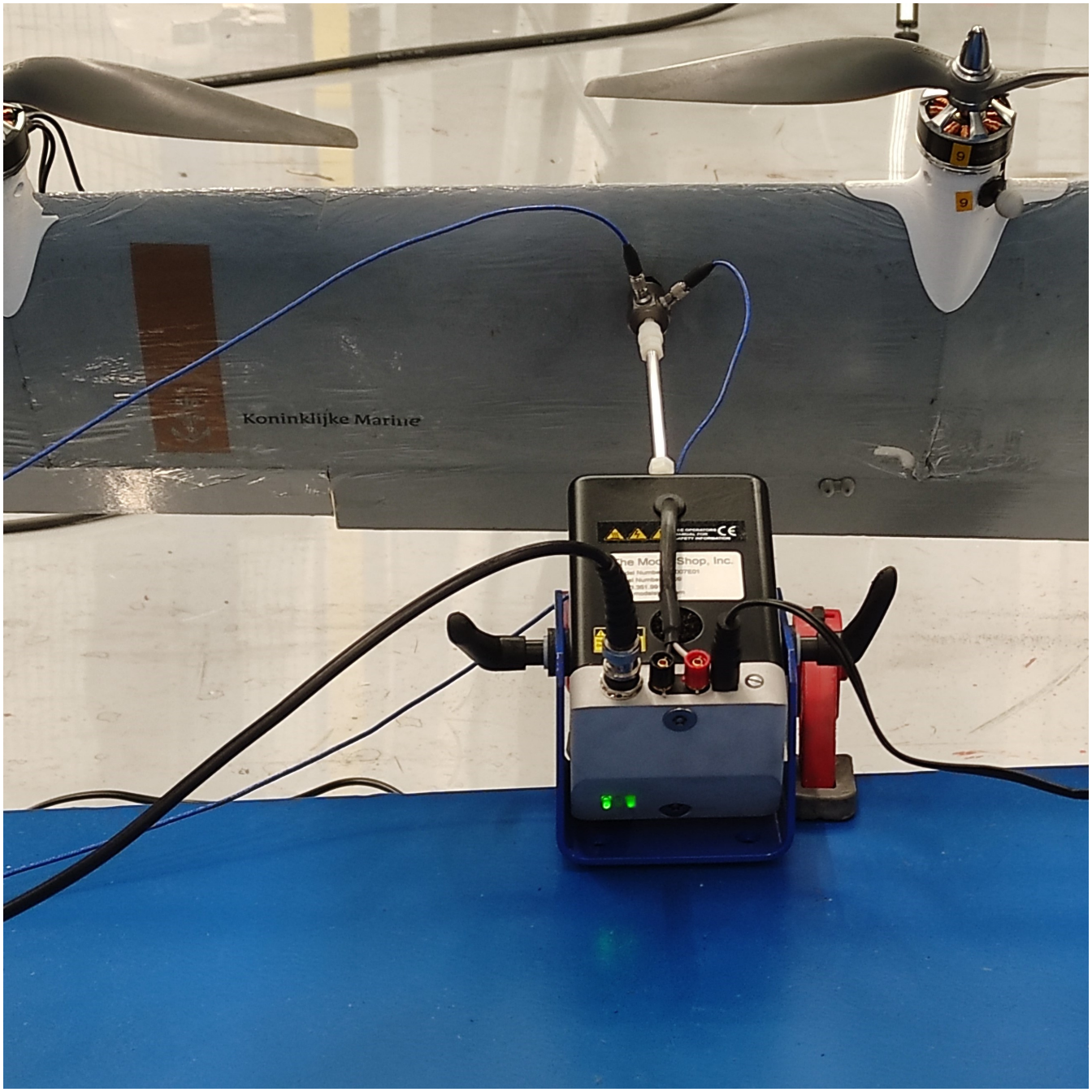


Fig. 26. Shaker and impedance head connection to the Nederdrone

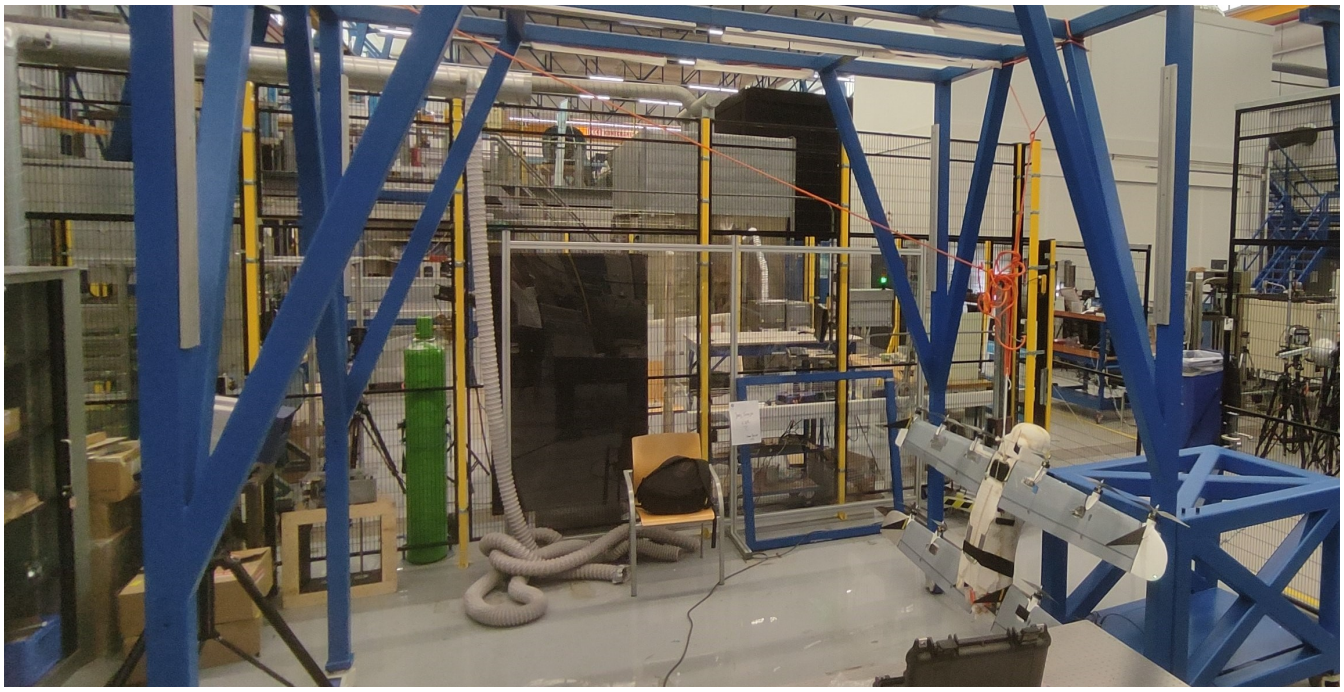

Fig. 27. Ground vibration test setup

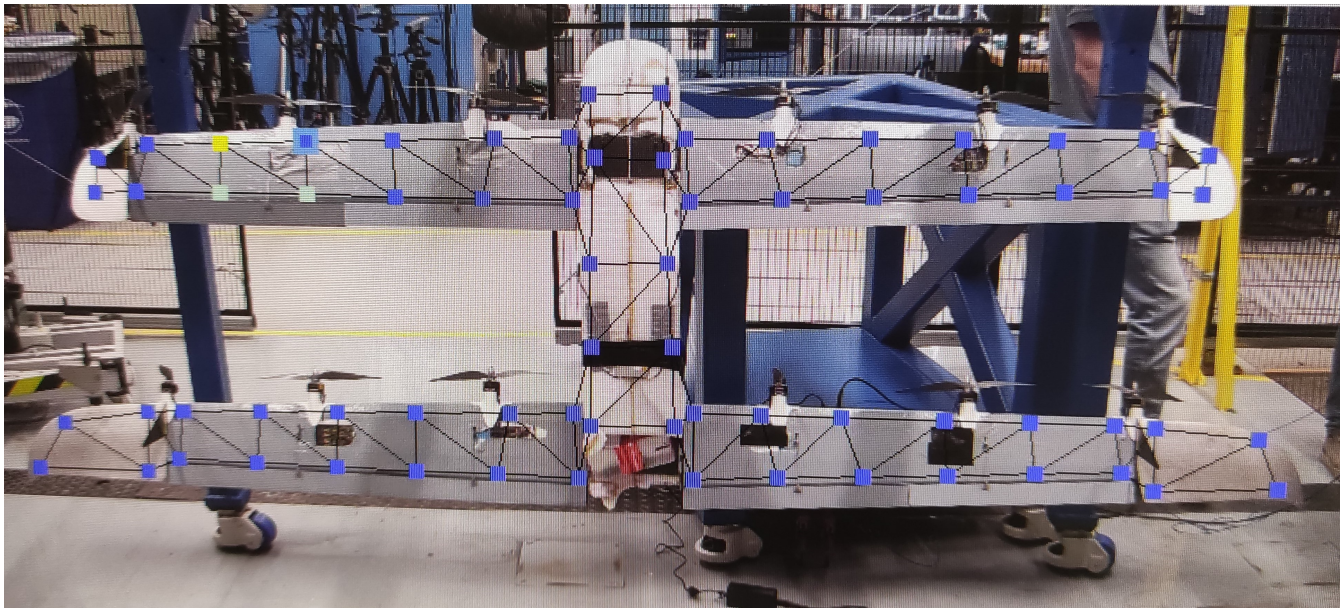

Fig. 28. Grid of measurement points

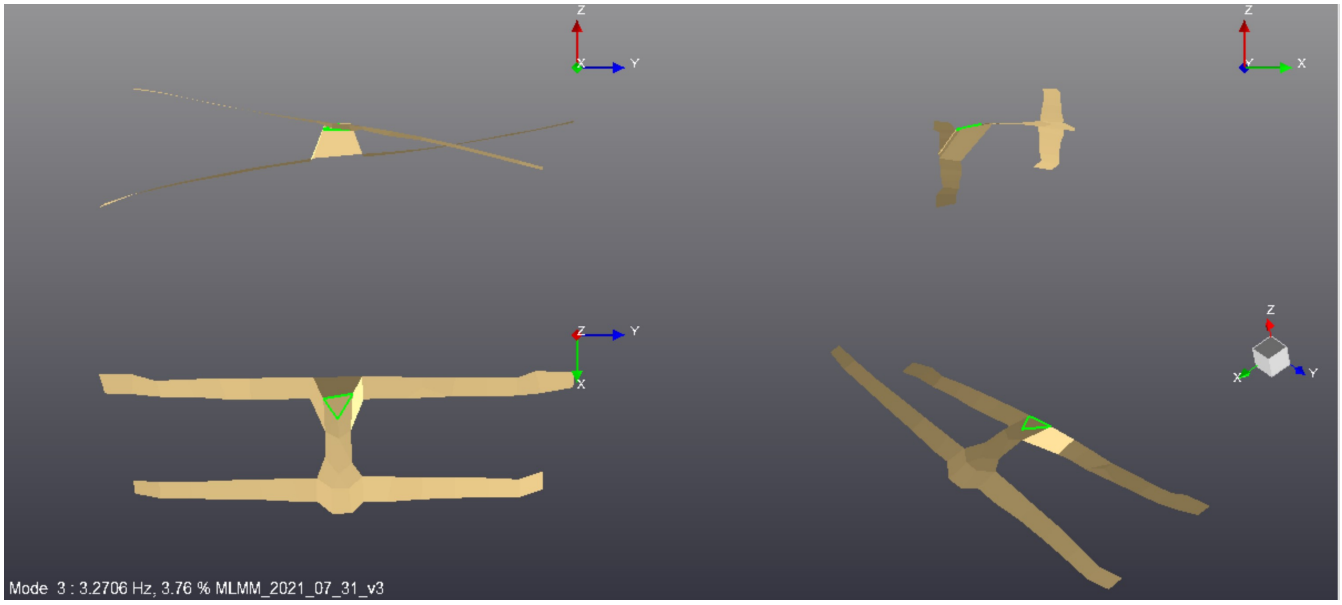


Fig. 29. First torsional mode of the fuselage

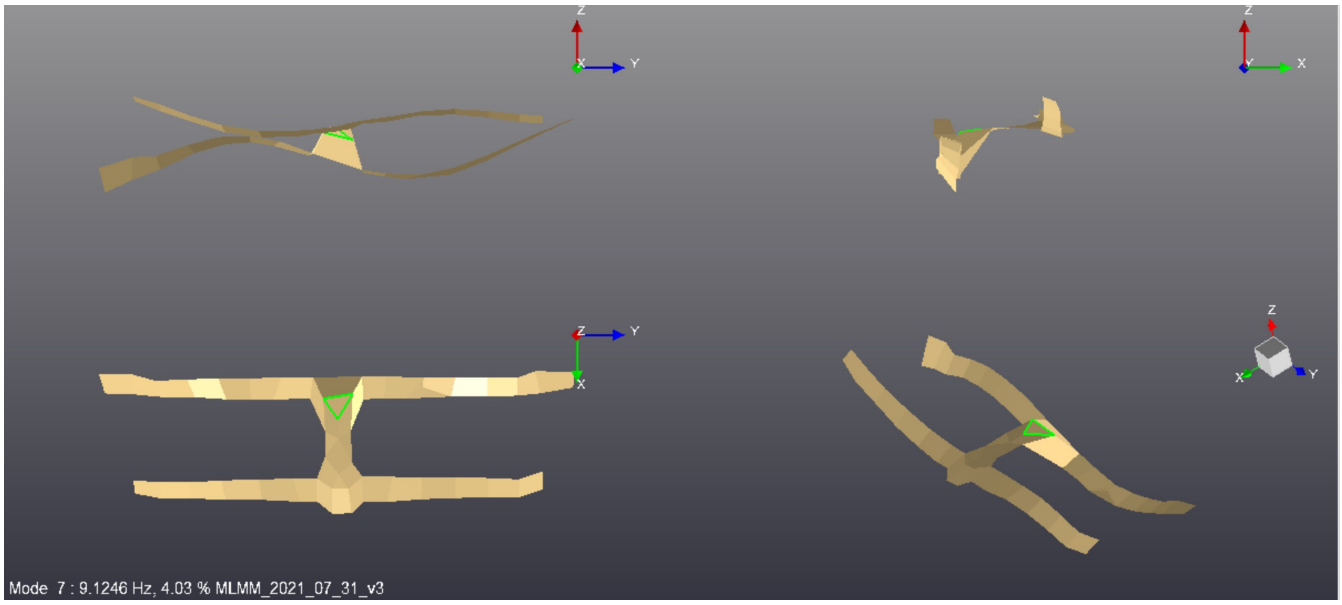


Fig. 30. Second torsional mode of the fuselage coupled with wing bending and torsion

TABLE V
STRUCTURAL MODES CORRELATION TABLE

| | Frequency [Hz] | Mode 1 | Mode 2 | Mode 3 | Mode 4 | Mode 5 | Mode 6 | Mode 7 | Mode 8 | Mode 9 | Mode 10 | Mode 11 | Mode 12 | Mode 13 | Mode 14 | Mode 15 |
|---|---|---|---|---|---|---|---|---|---|---|---|---|---|---|---|---|
| Mode 1 | 1.161 | 100,000 | 2,089 | 0,239 | 24,305 | 0,116 | 3,731 | 4,862 | 2,406 | 17,337 | 3,649 | 3,839 | 0,557 | 1,406 | 1,049 | 0,084 |
| Mode 2 | 2.541 | 2,089 | 100,000 | 1,326 | 0,277 | 11,239 | 6,680 | 6,459 | 0,880 | 0,704 | 17,627 | 11,831 | 0,147 | 0,762 | 3,088 | 0,781 |
| Mode 3 | 3.271 | 0,239 | 1,326 | 100,000 | 0,092 | 0,016 | 1,394 | 11,238 | 14,171 | 20,774 | 8,284 | 7,727 | 19,791 | 0,136 | 4,232 | 1,107 |
| Mode 4 | 5.185 | 24,305 | 0,277 | 0,092 | 100,000 | 3,127 | 41,283 | 5,040 | 11,192 | 23,720 | 0,777 | 22,101 | 0,288 | 3,181 | 31,709 | 14,178 |
| Mode 5 | 6.107 | 0,116 | 11,239 | 0,016 | 3,127 | 100,000 | 31,099 | 10,253 | 4,988 | 0,436 | 19,884 | 22,747 | 1,283 | 5,094 | 3,004 | 3,380 |
| Mode 6 | 8.272 | 3,731 | 6,680 | 1,394 | 41,283 | 31,099 | 100,000 | 12,217 | 6,036 | 3,711 | 10,941 | 20,105 | 2,466 | 7,061 | 14,596 | 7,599 |
| Mode 7 | 9.125 | 4,862 | 6,459 | 11,238 | 5,040 | 10,253 | 12,217 | 100,000 | 1,778 | 13,157 | 17,710 | 44,438 | 56,102 | 36,595 | 8,984 | 2,828 |
| Mode 8 | 11.589 | 2,406 | 0,880 | 14,171 | 11,192 | 4,988 | 6,036 | 1,778 | 100,000 | 5,686 | 11,979 | 0,110 | 13,418 | 11,495 | 5,914 | 1,966 |
| Mode 9 | 11.897 | 17,337 | 0,704 | 20,774 | 23,720 | 0,436 | 3,711 | 13,157 | 5,686 | 100,000 | 0,028 | 13,124 | 12,393 | 4,932 | 15,263 | 1,831 |
| Mode 10 | 13.038 | 3,649 | 17,627 | 8,284 | 0,777 | 19,884 | 10,941 | 17,710 | 11,979 | 0,028 | 100,000 | 24,667 | 3,884 | 4,773 | 0,266 | 0,002 |
| Mode 11 | 13.801 | 3,839 | 11,831 | 7,727 | 22,101 | 22,747 | 20,105 | 44,438 | 0,110 | 13,124 | 24,667 | 100,000 | 25,957 | 6,841 | 16,797 | 11,061 |
| Mode 12 | 16.974 | 0,557 | 0,147 | 19,791 | 0,288 | 1,283 | 2,466 | 56,102 | 13,418 | 12,393 | 3,884 | 25,957 | 100,000 | 65,125 | 1,463 | 5,786 |
| Mode 13 | 18.545 | 1,406 | 0,762 | 0,136 | 3,181 | 5,094 | 7,061 | 36,595 | 11,495 | 4,932 | 4,773 | 6,841 | 65,125 | 100,000 | 2,628 | 12,691 |
| Mode 14 | 21.658 | 1,049 | 3,088 | 4,232 | 31,709 | 3,004 | 14,596 | 8,984 | 5,914 | 15,263 | 0,266 | 16,797 | 1,463 | 2,628 | 100,000 | 57,824 |
| Mode 15 | 23.238 | 0,084 | 0,781 | 1,107 | 14,178 | 3,380 | 7,599 | 2,828 | 1,966 | 1,831 | 0,002 | 11,061 | 5,786 | 12,691 | 57,824 | 100,000 |

# 4

# Conclusion

As mentioned in the introduction, a slander and light airframe leads to the presence of low-frequency structural eigenmotions, which might be coupled with the flight controller dynamic, leading to limited self-sustained, or worse unstable, oscillations. This Thesis project focused on the case where the flight controller and the testing platform were an INDI-based flight controller and the Nederdrone, a vertical take-off and landing drone. The goal of the research was to investigate the behaviour and performances of different INDI implementations when integrated into an aircraft with low-frequency structural modes by answering the two research questions stated in the introduction 1.

Flight controllers' unstable interaction with aircraft structural modes is a well-known and studied phenomenon, which was thoroughly explored in the literary survey. The major findings were that overlooking the presence of low-frequency structural modes during the flight controller design process can lead to a servo-elastic coupling for different classes of controllers among which also INDI-based controllers are present. The coupling usually leads to structural damages or failures or limit-cycle oscillations. Different approaches are taken to neutralize this phenomenon: sensor measurements' signal filtering or the adoption of flight controllers that can both regulate the rigid body dynamics while damping the structural ones being the most common. INDI-based flight controllers have been successfully designed and utilized in both approaches, obtaining satisfactory results. In the preliminary analysis of the investigated problem, it was recorded how both heavy signal filtering and reduction of the INDI gain reduce and almost cancel the coupling phenomena. After the literature study and the preliminary analysis, the first research question was thoroughly investigated.

During the research it was found that the fuselage's torsional modes contribution to the angular acceleration measurement led to negative gain and phase margins, determining the instability of the system. The different INDI implementations investigated as possible solutions for this issue were all focused on feedback signal processing, due to the non-feasibility of an active vibration suppressing solutions. Specifically, three different signal filters were applied to the angular acceleration signal: a second-order Butterworth low-pass filter, a complementary filter providing a model-based high-frequency component, and a notch filter. All the filters were implemented both in a simulation environment and the real aircraft, but only the low-pass filter and the complementary filter were found to be stable and it was possible to assess their performance. While the complementary filter solution showed to perform better nonlinear dynamic inversion and to be faster in rejecting disturbances, there was almost no difference in how the two signal processing solutions affected the behaviour of the outer control loop. Therefore it was proved that for the Nederdrone, both standard and hybrid INDI are viable and equally effective options. These findings answer fully to the second research question concluding the research activity initially designed for this master thesis project.

# References


[1] S. Malisani, E. Capello, and G. Guglieri. "Development of a Flight Mechanics Simulation Computer based on a Flexible Aircraft Model for a Regional Aircraft". In: *IOP Conference Series: Materials Science and Engineering* 1024 (Jan. 2021), p. 012066. DOI: 10.1088/1757-899x/1024/1/012066.

[2] J. Becker, B. Caldwell, and V. Vaccaro. "*The interaction of flight control system and aircraft structure / Structural Aspects of Flexible Aircraft Control*". In: (2014).

[3] C. De Wagter et al. "*The NederDrone: A hybrid lift, hybrid energy hydrogen UAV*". In: *International Journal of Hydrogen Energy* 46.29 (2021), pp. 16003–16018. DOI: 10.1016/j.ijhydene.2021.02.053.